Inelastic Light Scattering Studies of Biological Macromolecular Solutions and Virus Crystals

by

© Stephen J. Spencer

A thesis submitted to the School of Graduate Studies in partial fulfillment of the requirements for the degree of Doctor of Philosophy.

Department of Physics and Physical Oceanography
Memorial University

April 2024

St. John's, Newfoundland and Labrador, Canada

Abstract

In this study, Brillouin light scattering is used as a tool to explore the elastic and viscoelastic properties of different macromolecular systems. Specifically, we explore two common macromolecular systems: aqueous solutions and crystals. By performing experiments on these different systems, we are able to explore the evolution of the properties of interest in three distinct regimes. By performing experiments on aqueous solutions, we are able to explore the dilute regime, wherein solute molecules may be treated as non-interacting particles, and the semi-dilute regime, where intermolecular interactions cannot be neglected. Finally, performing experiments on macromolecular crystals allows us to observe the elastic properties of macromolecules in the solid state.

The effects of macromolecular crowding have been extensively studied by various experimental techniques. Such works have demonstrated a significant amount of binding of solvent to the hydration shells of such crowders, drastically reducing the available free volume. In this work, Brillouin light scattering experiments were performed on aqueous solutions of Ficoll 70 and Ficoll 400 with concentrations ranging from 1 wt% to 35 wt% and Bovine Serum Albumin with concentrations of 1 wt% to 27 wt%. By examining the evolution of longitudinal Brillouin peak parameters with solute concentration, we calculated viscoelastic properties, including hypersound velocity, adiabatic bulk modulus and compressibility, apparent viscosity, and hypersound attenuation. Existing theory could only capture trends in this evolution up to a threshold concentration due to the neglect of intermolecular interactions. As such, the addition of a quadratic term was incorporated to account for intermolecular interactions between solute molecules. In Ficoll solutions, evidence of a central mode, which is due to relaxation of solvent in the polymer hydration shell, was observed.

In recent years, there has been a growing amount of interest in exploration of the elastic properties of crystalline macromolecular structures. Such properties of virus crystals, however, are still hardly known. In the present work, crystals of satellite tobacco mosaic virus were grown using hang drop vapour diffusion techniques. Crystal clusters grown were subsequently used in Brillouin light scattering experiments. Peaks in Brillouin spectra were determined to be due to longitudinal bulk modes, and the parameters of these peaks were used to approximate hypersound velocity and attenuation within the crystals.

For my parents,
who always supported me.

Acknowledgements

First and foremost, I would like to express my gratitude and appreciation to my supervisor, Dr. Todd Andrews. Thank you for your guidance, your patience, your understanding, and your tutelage over these years. I cannot properly express how honoured and privileged I have felt working alongside you. Thank you for having me as your graduate student and giving me the opportunity to work on this project.

I would also like to extend my thanks to Dr. Ayala Rao of University of California Riverside for providing me with the initial STMV samples used in this work, and Tim Walsh of Memorial University's Botanical Garden for his assistance in growing tobacco plants. Furthermore I would like to thank Dr. Anand Yethiraj and Dr. Venketesh Ranganthan for their invaluable insight into the mechanics of macromolecular solutions.

I would like to thank my parents for their unwavering support throughout the entirety of my academic career. Even after all these years, they still take interest in my work, and talk me through the stressful parts. I can never repay them for everything they have done for me.

Finally I would like to thank some of my fellow graduate students. Thank you to Dillon and Brad for always being around to bounce ideas off of eachother, and thank you for your patience when it was my turn to use the Brillouin scattering apparatus. And thank you to Kyle for being a fantastic office-mate and friend. Thanks for all the coffee runs, the beer trips, and for putting up with my ramblings.

Statement of contribution

In the presented work, Chapters 1-3 and 6 are independently authored by Stephen Spencer. Due to the manuscript nature of this thesis, the experimental results chapters (Chapters 4 and 5) have been written in collaboration, with Stephen Spencer as the primary author.

All experimental works presented in Chapter 4 were performed by Stephen Spencer. Chapter 4 was co-authored by Stephen Spencer and Dr. Todd Andrews.

Ficoll-400 samples used in Chapter 5 were fabricated by Dr. Venketesh Ranganthan, and samples of Ficoll-70 and BSA were fabricated by Stephen Spencer. All Brillouin scattering experiments in this chapter were performed by Stephen Spencer, and the chapter was co-authored by Stephen Spencer, Dr. Todd Andrews, Dr. Anand Yethiraj, and Dr. Venketesh Ranganthan.

Table of contents

List of tables

List of figures

List of symbols

U	Potential Energy
$u(R)$	Position
$P(R)$	Momentum
M	Mass
K, G	Spring Constant
$\vec{q}$, $\vec{k}$, $\vec{K}$	Wave Vector
ω, Ω	angular frequency
λ	Wavelength
S_{ijkl}	Elastic Compliance
σ_{ij}	Tensile Stress
C_{ijkl}	Elastic Stiffness Constant
f	Frequency
n	Refractive Index
v	Speed
B	Bulk Modulus
ρ	Density
χ	Compressibility
V	Volume
P	Pressure
α	Hypersound Attenuation / Fitting Parameter Relating Solute and Solvent Velocities
τ	Characteristic Lifetime
κ	Thermal Conductivity
η_b	Bulk Viscosity
η_s	Shear Viscosity
$S_{\rho\rho}(\vec{q},\omega)$	Spectral Density Function
$N(t)$	Number of particles
$\vec{J}(\vec{r},t)$	Particle Flux
$\vec{u}_B(\vec{r},t)$	Brownian Particle Velocity
$\vec{G}(t)$	Momentum Vector
$\vec{g}(\vec{r},t)$	Momentum Density Vector

List of symbols

$\vec{\tau}_{ij}(\vec{r},t)$	Momentum Flux
$\vec{S}$	Surface Area Vector
$\vec{F}$	External Force
$E(t)$	Energy
$e(\vec{r},t)$	Energy Density
$\vec{J}_e(\vec{r},t)$	Energy Flux
$Q(\vec{r},t)$	Heat
$T(\vec{r},t)$	Temperature
c_v	Volumetric Specific Heat
c_p	Barometric Specific Heat
$S(\vec{q})$	Structure Factor
η	Apparent Viscosity
μ_S	Solute Mass Fraction
Λ	Normalized Sound Attenuation Parameter

List of abbreviations

BSA	Bovine Serum Albumin
STMV	Satellite Tobacco Mosaic Virus
TMV	Tobacco Mosaic Virus
PEG	Poly(Ethelene) Glycol
NMR	Nuclear Magnetic Resonance
RNA	Ribonucleic Acid
DNA	Deoxyribonucleic Acid
WIV	Wiseana Iridovirus
PMMA	Polymethyl Methacrylate
RPM	Rotations Per Minute

Chapter 1

Introduction

The study presented within this work contains two primary components which utilize Brillouin light scattering spectroscopy as a tool to explore the properties of macromolecular systems. Brillouin light scattering is a non-invasive and non-destructive laser spectroscopy technique used to study the propagation of acoustic phonons within a material. In the present work, acoustic waves propagating in both solid and liquid systems are referred to as phonons.

Firstly, this study reports on Brillouin light scattering studies of aqueous solutions of polymers Ficoll 70, Ficoll 400, and Bovine Serum Albumin (BSA). Solution elastic and viscoelastic properties were determined over the dilute and semi-dilute ranges from the dependence of Brillouin peak frequency and width. The concentration dependencies of these properties were not consistent with existing theory but instead were found to be well-described by expressions derived from a new model relating hypersound frequency and solute concentration. Furthermore, Brillouin spectra of high concentration Ficoll solutions demonstrated properties associated with solute hydration. Such properties were subsequently used to calculate a relaxation time associated with hydration.

Secondly, Brillouin scattering experiments were performed on crystals formed from satellite tobacco mosaic virus (STMV) particles. STMV crystals were grown using hang-drop vapour diffusion techniques. Various techniques were used to optimise crystal growth, until such a technique was able to consistently grow crystals which were suitable in size. Such crystals were subsequently used in Brillouin light scattering experiments. Such experiments were performed in an attempt to observe longitudinal acoustic modes as well as individual phonon modes propagating within the sample. Longitudinal bulk mode frequency was subsequently used to approximate phonon velocity and attenuation within the crystals.

1.1 Macromolecules

Organic molecules are sets of atoms bound together by covalent bonds. For most macromolecules, this definition is satisfactory. However in some macromolecules atoms are held together by several other secondary forces. Therefore, it is practical to define a macromolecule as a group of atoms which move together and do not dissociate. Such macromolecules typically exhibit a regular structure and behave like a conventional covalently bonded molecule in most physiochemical aspects [1]. Some common forms of macromolecules are polymers, nucleic acid, and colloids.

1.2 Macromolecules in Solution

In the past there have been many studies on macromolecular solutions through several different means of experiment. Properties of macromolecular solutions have been rigorously studied by means of diffusion experiments, rheology, and NMR. However there have been very few studies of macromolecular solutions by means of Brillouin scattering. As such, the following section will summarize some work which has been performed on various macromolecular solutions.

In a study by Pochylski *et al.*, Brillouin light scattering experiments were performed on poly(ethylene glycol) 600 (PEG600) solutions at various concentrations and temperatures ranging from 288 K to 363 K [2]. A single set of Brillouin peaks was observed in these spectra, and change in Brillouin peak shift and width was recorded as a function of temperature. This allowed for further calculations of elastic properties, such as phonon velocity, sound attenuation, and adiabatic compressibility, shown for changing temperature. At high concentrations, a relaxation mode was observed in spectra, which was attributed to hydration of PEG due to surrounding solvent.

Furthermore, Pochylski *et al* performed Brillouin light scattering experiments on PEG 400 at temperatures below crystallization temperature [3]. In this temperature range, a second set of Brillouin peaks was observed, which corresponded to PEG400 crystallites forming in the solution. The frequency shift and width of both sets of peaks were used to show the evolution of different zones of local compressibility with changing temperature and concentration.

Svandize *et al.* performed Brillouin light scattering experiments on solutions of lysozyme at temperatures ranging from 293 K to 355 K [4]. The evolution of phonon velocities and dampening were observed over a range of temperatures. A critical temperature of 343 K was observed in Brillouin spectra. At this temperature, phonon dampening was at a maximum, whereas both phonon speed and Brillouin peak intensity were minimized. This anomalous point was determined to be due to the beginning of a sol-gel transition in high concentration lysozyme solutions.

In a follow-up study, Asenbaum *et al*. performed Brillouin light scattering experiments on water-lysozyme solutions at the same temperature range [5]. A minimum in Brillouin peak intensity was also observed at 343 K. An extreme minimum was also observed in the intensity of the central Rayleigh peak. For temperatures less than the critical temperature, the temperature dependence of the peak intensity is much stronger than calculations predicted, whereas at temperatures above the critical temperature, the temperature dependence was much smaller. This indicated that the solution of folded lysozyme molecules in solution had irreversibly become a gel of thermally unfolded lysozyme.

Brillouin light scattering was performed on a number of different macromolecular solutions, including glycine, triglycine, glycerol, sucrose, lysozyme, BSA, and gelatin, at various concentrations by Adichtev *et al*. [6]. They found that for nearly all materials studied, Brillouin peak shift and width increased with increasing concentration following a universal relationship. This relationship was derived from a Reuss average of the bulk moduli of the constituents of a two component system, treating them as non-interacting particles. It was also shown that the relationship between Brillouin peak properties and solution viscosity do not follow a universal relationship,as peak shift and peak linewidth did, and show more variance with macroscopic viscosity.

Roldán-Ruiz *et al* performed Brillouin light scattering, and complimentary NMR spectroscopy, on binary mixtures of malcine, a macromolecule formed through the reaction of malic acid and choline chloride, and water [7]. This study measured acoustic velocity with changing concentration over a full range of % weight concentrations, ranging from pure water to pure malcine. Two linear regimes, increasing with increasing concentration, were observed in the relationship between acoustic velocity and malcine concentration, with a transition at 70% malcine concentration by weight. This transition was described to be the transition from malcine in water to water in malcine. This transitionary region was further demonstrated by a divergence in self-diffusion coefficients for concentrations below 70%, as measured by NMR spectroscopy.

Aside from observing the evolution of phonons in macromolecular solutions, Brillouin light scattering has also been used as a technique to observe hydration of macromolecules within solution. In such studies, a weak and wide mode was observed within the central elastic peak of a spectrum. This phenomenon was first observed by Pinnow *et al.*, and was attributed to relaxation due to hydration of solute molecules by the surrounding solvent [8]. More specifically, the width of the central peak is directly proportional to the relaxation time of hydration. This relaxation corresponds to solvent molecules entering and exiting the hydration shell of solute molecules, and the relaxation time corresponds to the duration of the occupancy within the hydration shell. This phenomenon has been explored in many different macromolecular solutions, such as LiCl [9], DNA [10], hyaluronic acid [11], PEG 600 [2], and more.

The use of Brillouin scattering has also been used to observe hydration of glycoproteins in gastropod mucus in work by Hanlon *et al* [12, 13]. This work observed the change in Brillouin peak parameters as a function of temperature, and observed the appearance of a Brillouin peak due to ice crystals at temperatures below -2.5°C. This depression in freezing temperature from 0°C was determined to be due to hydration of glycoproteins. More specifically, the water bound to the hydration shells of the glycoproteins was unable to reorient itself into a configuration which would allow freezing. This depression in freezing point temperature was also observed to move further from 0° with increasing glycoprotein concentration [13].

While the studies listed above have done considerable work exploring the viscoelastic properties of different aqueous macromolecular solutions, these works have all worked in relatively low concentration ranges. As such, they treat these macromolecules as non-interacting particles. The aim of this work is, therefore, to explore the viscoelastic properties of such solutions at higher concentrations, where there is a significant degree of macromolecular crowding and the inter-molecular interactions can no longer be ignored. It is expected that this increase in macromolecular crowding will cause a further increase in phonon frequency and Brillouin peak linewidth, and subsequently other viscoelastic properties calculated from these measured properties.

1.3 Ficoll

Ficoll is a neutral, highly branched copolymer comprised of sucrose and epichlorohydrin. Despite its branching nature, diffusion experiments have shown that Ficoll is spherical, and not linear like other branching polymers, as shown in the schematic in Figure 1.1 [14]. Due to its well known diffusion properties, it has commonly been used as a test solute in filtration experiments [14, 15]. Within the last fifteen years however, diffusion experiments involving ficoll have shown larger diffusion rates than were predicted by theory and simulation for hard spheres [16]. This led to the understanding that ficoll is not a rigid sphere, but is instead globular, with more freedom to have its shape altered by its environment [16].

There are two variations of Ficoll which were used in this work. The first is ficoll-70, which has a mass of 70 kDa and Stokes radius (the effective hydrated raduis) of 5.10 nm [17]. The second type is Ficoll-400, which has a mass of 400 kDa and a Stokes radius of 10.0 nm [18].

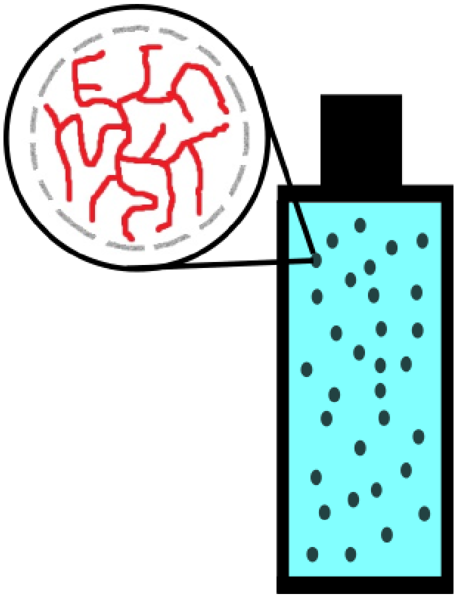

Figure 1.1: Schematic of Ficoll molecules in solution.

To date, the acoustic dynamics of aqueous Ficoll solutions have not been explored through means of inelastic light scattering. As such, this study used Brillouin light scattering to explore phonon and viscoelastic properties (specifically as hypersound velocity, bulk modulus, apparent viscosity, and hypersound attenuation) of Ficoll solutions as concentration is changed.

1.4 Bovine Serum Albumin

Bovine serum albumin (BSA) is a globular protein primarily found within the blood of cattle. BSA has a well known size and shape, similar to the schematic of Ficoll in Figure 1.1, and has therefore been used extensively as a macromolecular crowding agent [19–21], and has also been commonly used in diffusion experiments [22–26]. BSA molecules are ellipsoidal with a Stokes radius of 3.8 nm and molecular mass of 66.5 kDa [27]. While few, there have been some studies of phonon velocity in BSA based systems by use of Brillouin scattering.

Bohidar *et al.* performed Brillouin light scattering experiments on BSA, as well as insulin, as a function of environmental pressure [28]. A quadratic relationship between environmental pressure and phonon velocity was observed for BSA solutions at room temperature. Furthermore, an exponential decrease in compressibility, and consequentially, an exponential increase in rigidity modulus, was observed for increasing pressure.

Molecular dynamics simulations were performed by Hanlon *et al.* to investigate the viscoelastic properties of different aqueous macromolecular solutions [29]. These simulations studied an anti-freeze glycoprotein, a toxin protein, and BSA at temperatures ranging from 280 K - 340 K. This study showed that with increasing temperature, there was an increase in hypersound velocity and bulk modulus, and a decrease in viscosity. Interestingly, temperature dependent studies showed a weak maximum in velocity and hypersound modulus before approaching convergence between the different solutions. Furthermore, in the anti-freeze data, there was an increase in hypersound velocity and bulk modulus with increasing protein concentration, which closely resembled experimental data.

In a study by Yan *et al.*, Brillouin light scattering was used to probe dextran ($H(C_6H_{10}O_5)OH$), a complex and branched polysaccharide. Molecules within organic cells were subsequently compared to systems of other macromolecular systems, including BSA [30]. Brillouin results from this study showed a linear relationship between phonon velocity and concentration. However data for BSA experienced a deviation from linearity at 10% weight concentration. This change in linearity was attributed to increased interactions between BSA molecules. Such interactions lead to volume fluctuations within BSA molecules, which therefore reduce the compressibility of molecules. This fluctuation of cell volume and structure was also determined to be the cause of a change in the rate of change of phonon velocity with concentration.

While there have been some experimental works used to explore phonon velocity of BSA solutions, there has been no work to date further exploring the evolution of elastic behaviour of aqueous BSA solutions with changing concentration. Therefore, this study aims to use Brillouin light scattering techniques to probe acoustic bulk phonons in BSA solutions and perform an in depth look into elastic behaviour such systems.

1.5 Definition of a Virus

The concept of a virus was first put forward by Bijerinck in 1898 as a means to describe an infectious agent which is smaller than a bacterium [31]. The virus he was describing was tobacco mosaic virus, which was first described as the mosaic disease of tobacco by Adolph Mayer [32].

Whereas organic host cells contain two types of nucleic acid, DNA and RNA, virus particles contain only one type of nucleic acid. This can be either DNA or RNA. All genetic information for reproduction of a virus is encoded in its nucleic acid. However it lacks the components for independent self replication. As such, a virus can not reproduce on its own, and therefore must attach itself to a host cell in order to replicate.

In a study by Talati and Jha, low frequency vibrational modes were calculated using an elastic continuum approximation model for spherical virus particles immersed in a medium [33]. The vibrational modes of virus nanoparticles were calculated from a classical point of view, starting with Lamb's equation of motion for a three-dimensional elastic body. It was shown that the Lamé constants (material dependent parameters which describe the stress-strain relationship) relate to elastic constants, as $\lambda = C_{12}$ and $\mu = C_{44}$.

In a study by Hartschuch *et al.* Brillouin light scattering experiments were performed on Wiseana iridovirus embedded within Poly(methyl methacrylate) using the 514.5 nm line of an Ar^{+} laser, analyzed with a tandem Fabry-Perot interferometer [34]. WIV samples were placed on a silicon substrate for analysis. Spectra were collected with different incident wave-vectors. In these spectra, a weak peak was observed at $\nu_T = 8.8 \pm 0.2$ GHz, corresponding to a transverse acoustic mode. This leads to a transverse acoustic phonon velocity of $\mathrm{v}_T = 1450 \pm 50$ m/s. Using $\mathrm{v}_L = 2\mathrm{v}_T$ for a crystal with Poissons ratio $\sigma = 0.33$, the longitudinal acoustic phonon velocity was estimated to be $\mathrm{v}_L = 2900 \pm 200$ m/s. Finally, Hartschuch calculated Young's modulus to be $\mathrm{E} = 6.7$ GPa.

A study by Sirotkin *et al.* was performed which aimed to explore phonon dynamics of different viruses, treating them as nano-particles [35]. Low frequency Brillouin and Raman scattering was performed on several large viruses, with diameters of 140 - 190 nm, and compared to similar sized colloidal nano-spheres. Despite structural similarities between the viruses used in this study and colloidal nano-spheres, Brillouin and Raman scattering experiments did not show any evidence of nano-particle modes. It was determined that this was possibly due to the complexity of the inner structures of viruses. Sirotkin *et al.* also expressed that the heterogeneous elasticity and/or the diffuse structures of the viruses could prevent the development of motional coherence within the virus particles.

Brillouin spectra collected on macromolecule and virus crystals have exhibited acoustic phonon frequencies almost an order of magnitude lower than those of conventional crystals, attributed to their weaker bonding properties. This work aims

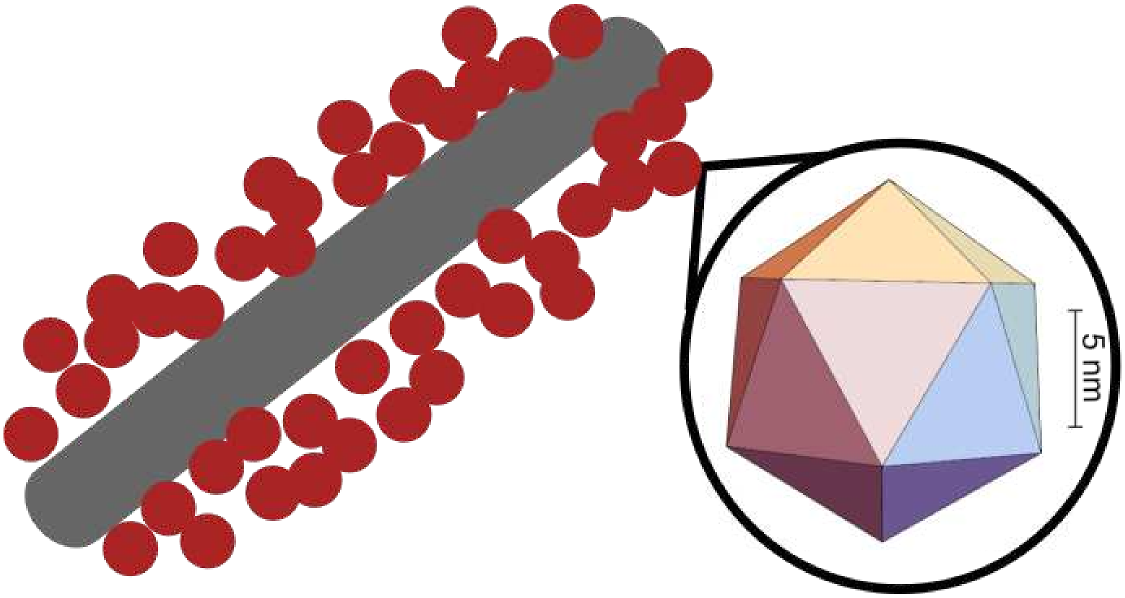

Figure 1.2: Schematic of icosahedral structure of STMV, comprised of twenty equal triangular faces, surrounding helper virus TMV molecule. Each triangular face contains three capsid subunits. Icosahedron generated by Mathematica.

to explore these phonon properties within virus crystals, and the elastic properties derived from them.

1.6 Satellite Tobacco Mosaic Virus

STMV is an icosahedral ssRNA virus diameter of 17 nm. STMV has a triangulation number of T = 1, meaning that it is comprised of 60 identical capsid subunits, evenly distributed between its 20 faces . As a satellite virus, STMV does not encode a capsid protein and therefore lacks the ability to self replicate. Though it can not self replicate, STMV may spread when in the presence of a helper virus. The helper virus most commonly associated with STMV is tobacco mosaic virus, TMV, which is a cylindrical-like virus with a length roughly 18 times the diameter of STMV [36].

1.7 Crystallization of Macromolecules

The first crystallization of macromolecules was performed by Hünefeld in 1840, who successfully crystallized hemoglobin from the blood of an earthworm [37]. Crystallization of hemoglobin was the focus of many studies at this time. However the first study to reproducibly grow hemoglobin crystals was performed by Fünke in 1951 [37].

While conventional and macromolecular crystals are superficially similar, there are important differences between them. Macromolecular crystals are often very fragile. Since macromolecules often lack inversion symmetry, the morphologies of macromolecular crystals are typically simple.

Macromolecular crystals typically grow in very narrow ranges. They can usually only grow in temperatures ranging from 0°C - 30°C, and fairly neutral pH ranges. Furthermore, macromolecular crystallization requires an incredibly high solvent content, no less than 30%. In most cases, the solvent content in solution is between 40% - 60% [38]. However some macromolecules have required solutions of 90% solvent [39, 40]. Macromolecules in solution typically crystallize in small islands which eventually branch together. As such, lattice constraints are tenuous and few. This contributes to high levels of disorder in crystals. Unlike conventional crystals, macromolecular crystals often have a large degree of hydration within them. As such, they cannot be exposed to air or too long without losing aspects of their diffraction patterns [41]. The resulting crystals also exhibit a large amount of polymorphism. For example, STMV crystals can be orthorhombic, monoclinic, or cubic. The cell sizes of macromolecular crystals are large, ranging from 30 Å to several hundred Å. Since scattering intensity is inversely proportional to cell size, macromolecular crystals typically exhibit weak light scattering properties [37].

Crystallization of proteins, RNA, and viruses employ many of the same mechanisms as conventional crystals. Some of these growth mechanisms include spiral dislocation, 2D nucleation, random nucleation, and 3D aggregation. Unlike conventional crystallization, but macromolecular crystallization may employ different mechanisms in the same face, or change from one mechanism to another [37].

Macromolecular crystals require extremely high levels of supersaturation, on the order of a few hundreds to thousand percent, and more complex solutions, often involving salts and buffer solutions. Due to the complex nature of solution required for crystallization, there is a higher chance of impurities within the final crystal. Crystals may be grown using seeding techniques, but it becomes less effective with larger molecules [37].

While crystallization of viruses and proteins dates back as far as the 1940's [42, 43], crystallization of STMV has only been explored over the last 30 years [44]. Virus crystals, a type of macromolecular crystal, are typically very small, rarely exceeding 1 mm, such is the case for STMV crystals. STMV crystals have been grown as large as 200 μm under reproducible conditions [45], however STMV crystals were grown to 1.5 mm in a zero-gravity environment [46].

The growth of six macromolecular crystals, including STMV, was observed by means of atomic force microscopy in real time by Malkin *et al.* [47]. Crystals were nucleated in small droplets (3 ml), which produced no more than 3 - 5 seed crystals. These crystals were then transferred to a cell containing 50 ml of the correspoonding macromolecular solution. Concentrations of solution varied between different types of macromolecules. Crystal growth was examined over periods of several hours. During this time, crystals grew from microcrystals of size 40 - 50 μm to mature crystals of size 0.5 mm. Finally, STMV crystallized differently from other macromolecules observed. No dislocations were observed in STMV crystals. The dominant growth mechanism of STMV was continuous sedimentation and absorption of three dimensional nuclei. Upon absorption, nuclei continued to grow by both two dimensional nucleation, growth in the normal direction, and by step flow over the surface of the larger crystal. These nuclei rapidly develop into multi-layer plateaus. The heights of the plateaus varied, ranging from 12 - 510 nm (8 - 34 layers) [47].

Land *et al.* were able to show the process of a canavalin macrocluster forming step bunches, generating a plateau on the top as it growed. It was shown that the crystal step train merged with the macrocluster, continuing to grow without defects. This is different from microcrystal incorporation, which would involve the growth of many defects. It is unknown whether or not the macroclusters are ordered in the beginning, but it is presumed that they reorient themselves to align with the crystal lattice. This process is similar to results reported for thaumatin [48] and STMV [49]. Topmost terraces formed by macroclusters in this study were significantly larger than those generated by dislocation hillocks. 2D nucleation was observed in terraces formed by macroclusters, however no 2D nucleation occurred on terraces formed from dislocation hillocks outside extremely high supersaturation.

1.8 Elastic Properties of Macromolecular Crystals

While crystallization of viruses and other macromolecules has been well researched over the last hundred years, the exploration of the elastic properties of such crystals is still a relatively new field of research. As such there have been few studies on the elastic properties of macromolecular crystals and, in particuar, virus crystals. For this reason, the following section will summarize some work done on both virus and protein crystals.

In a study by Tachibana *et al.* acoustic properties of crystalline lysozyme were explored using ultra-sonic pulse echo method [50]. Acoustic phonon velocity was measured along the [110] direction, and found to be v = 1817 m/s ± 5%. In this work, it was shown that $C_{11} + C_{66} = 3.99$ GPa. Young's modulus for crystalline lysozyme was calculated to be $E = 2.70$ GPa, using $\sigma = 0.33$ as Poisson's ratio. Furthermore, shear modulus and bulk modulus were calculated using $\mu = E/2(1+\sigma)$ = 102 GPa and K = $E/3(1-2\sigma)$ = 2.65 GPa, respectively.

Chernov *et. al* performed a rigorous study of the growth of protein crystals, covering many topics, including surface energy, elasticity, cracking, solubility, nucleation, growth modes, and crystal perfection [51]. Protein crystals and other macromolecular crystals are known to be very soft and fragile. The Young's modulus for several macromolecular crystals have been calculated from experimental results measuring vibrational frequencies. Measurements of crystal plasticity and strength were made by triple point bending of as-grown triclinic lysozyme rods. The deflection of lysozyme was linear with applied force. This occurred until the deflection began to cause cracking in the crystal. This suggests that these crystals are purely elastic up to their strength limit. In bending experiments, four lysozyme rods with different faces in contact with the bottom surface of a cuvette were measured. The Young's modulus found using an isotropic approximation were E = 0.1 - 0.5 GPa. These values are roughly 2-3 times lower than those for cross-linked lysozyme, and 10 - 100 times lower than those for conventional crystals. Compressibility of crystals was calculated and compared to compressibility of protein molecules (calculated measuring frequencies of ultrasound in protein solutions). Interestingly, the crystals were much softer than the molecules composing them. Assuming a Poisson's ratio of 0.25 for lysozyme molecules, Young's modulus was calculated. This yielded a value of $E \simeq 1.5 \cdot \mathrm{K}$, where K is the bulk modulus.

In a study by Stephanidis *et al.*, STMV crystals were grown through hang-drop vapour diffusion, and subsequent Brillouin light scattering experiments were performed [45]. Different STMV conditions were investigated, STMV solutions, fully hydrated crystals, and severely dehydrated crystals. STMV solution was purified from STMV that was twice recrystallized from NaCl. The final concentration of solution was 8.5 mg/ml. From this solution, STMV crystals were grown using hang-drop vapour diffusion at room temperature with a buffer solution of 0.025 M sodium sulphate at pH 6.8. After growth, crystals were transferred into sealed glass capillaries with minimum mother liquor to ensure full hydration and stability of crystals. Finally, dry crystals were prepared by slowly evaporating mother liquor in unsealed capillaries in air over several days. Dry crystals became slightly opaque. However STMV crystal shape and crystalline organization remained unchanged. In this study, Brillouin light scattering experiments were performed with a laser of wavelength $\lambda = 532$ nm and power of 10 mW. Different scattering geometries were used to explore the phonon dynamics of STMV. For STMV solutions, all spectra showed only Brillouin features characteristic of aqueous buffers were observed. This was likely due to the small concentration of STMV in the solution. The first peak observed in Brillouin spectra, at $\nu = 8.00 \pm 0.05$ GHz was an effect of the aqueous buffer within the wet crystal, and the broader peak at $\nu = 11.2 \pm 0.2$ GHz arose from STMV. Both of these peaks were due to longitudinal acoustic modes propagating in their respective media. This value led to a calculated longitudinal acoustic mode velocity in STMV of $v = 1920 \pm 70$ m/s. Once the crystal had dried, the longitudinal acoustic mode frequency shifted to $\nu = 200 \pm 0.5$ GHz, corresponding to a phonon velocity of v = 3430 ± 80 m/s.

Bibliography

[1] P Munk and T M Aminabhavi. *Introduction to Macromolecular Science*. Wiley, New York, NY, 2002.

[2] M Pochylski, F Aliotta, Z Blaszczak, and J Gapiński. Structuring effects and hydration phenomena in poly (ethylene glycol)/water mixtures investigated by brillouin scattering. *The Journal of Physical Chemistry B*, 110(41):20533–20539, 2006.

[3] M Pochylski and J Gapinski. Brillouin scattering study of polyethylene glycol/water system below crystallization temperature. *The Journal of Physical Chemistry B*, 114(8):2644–2649, 2010.

[4] AV Svanidze, VP Romanov, and SG Lushnikov. Anomalous behavior of brillouin light scattering at thermal denaturation of lysozyme. *JETP letters*, 93(7):409–414, 2011.

[5] A Asenbaum, C Pruner, HW Schröer, K Plätzer, L Bieler, H Brandstetter, W Schirmacher, A Schulte, and E Wilhelm. Rayleigh and brillouin scattering in a lysozyme–water mixture: An unusual behavior around 343 k. *Journal of Molecular Liquids*, 158(1):7–12, 2011.

[6] SV Adichtchev, Yu A Karpegina, KA Okotrub, MA Surovtseva, VA Zykova, and NV Surovtsev. Brillouin spectroscopy of biorelevant fluids in relation to viscosity and solute concentration. *Physical review E*, 99(6):062410, 2019.

[7] MJ Roldán-Ruiz, RJ Jiménez-Riobóo, MC Gutiérrez, ML Ferrer, and F del Monte. Brillouin and nmr spectroscopic studies of aqueous dilutions of malicine:

Determining the dilution range for transition from a “water-in-des” system to a “des-in-water” one. *Journal of Molecular Liquids*, 284:175–181, 2019.

[8] DA Pinnow, SJ Candau, and TA Litovitz. Rayleigh scattering: orientational relaxation in liquids. *The Journal of chemical physics*, 49(1):347–362, 1968.

[9] NJ Tao and SM Lindsay. Reorientational relaxation of water molecules in licl solution studied by depolarised rayleigh scattering. *Journal of Physics: Condensed Matter*, 1(44):8709, 1989.

[10] NJ Tao. Light scattering spectroscopy studies of water molecules in dna. *Water and Biological Macromolecules*, page 266, 1993.

[11] SA Lee, MR Flowers, WF Oliver, A Rupprecht, and SM Lindsay. Brillouin-scattering study of hyaluronic acid: dynamic coupling with the water of hydration and phase transitions. *Physical Review E*, 47(1):677, 1993.

[12] D F Hanlon, M J Clouter, and G T Andrews. Temperature dependence of the viscoelastic properties of a natural gastropod mucus by brillouin light scattering spectroscopy. *arXiv preprint arXiv:2306.06807*, 2023.

[13] D F Hanlon, M J Clouter, and G T Andrews. Influence of hydration and dehydration on the viscoelastic properties of snail mucus by brillouin spectroscopy. *arXiv preprint arXiv:2308.00524*, 2023.

[14] MP Bohrer, Gary D Patterson, and PJ Carroll. Hindered diffusion of dextran and ficoll in microporous membranes. *Macromolecules*, 17(6):1170–1173, 1984.

[15] M G Davidson and W M Deen. Hindered diffusion of water-soluble macromolecules in membranes. *Macromolecules*, 21(12):3474–3481, 1988.

[16] W H Fissell, S Manley, A Dubnisheva, J Glass, J Magistrelli, A N Eldridge, A J Fleischman, A L Zydney, and S Roy. Ficoll is not a rigid sphere. *American Journal of Physiology-Renal Physiology*, 293(4):F1209–F1213, 2007.

[17] Avanator. *Ficoll PM70, Cytiva*, 2022.

[18] Avanator. *Ficoll PM400, Cytiva*, 2022.

[19] K Totani, Y Ihara, I Matsuo, and Y Ito. Effects of macromolecular crowding on glycoprotein processing enzymes. *Journal of the American Chemical Society*, 130(6):2101–2107, 2008.

[20] C Ota and K Takano. Behavior of bovine serum albumin molecules in molecular crowding environments investigated by raman spectroscopy. *Langmuir*, 32(29):7372–7382, 2016.

[21] M Bercea and IA Plugariu. Macromolecular crowding in solutions of bovine serum albumin and neutral polymers. In *2021 International Conference on e-Health and Bioengineering (EHB)*, pages 1–4. IEEE, 2021.

[22] M L Wagner and H Scheraga. Gouy diffusion studies of bovine serum albumin. *The Journal of Physical Chemistry*, 60(8):1066–1076, 1956.

[23] T Raj and WH Flygare. Diffusion studies of bovine serum albumin by quasielastic light scattering. *Biochemistry*, 13(16):3336–3340, 1974.

[24] R D Tilton, C R Robertson, and A P Gast. Lateral diffusion of bovine serum albumin adsorbed at the solid-liquid interface. *Journal of colloid and interface science*, 137(1):192–203, 1990.

[25] A K Gaigalas, J B Hubbard, M McCurley, and S Woo. Diffusion of bovine serum

albumin in aqueous solutions. *The Journal of Physical Chemistry*, 96(5):2355–2359, 1992.

[26] K. Akintola. Evaluation of the physical properties of experimental macromolecular crowding systems. Master's thesis, Memorial University of Newfoundland, Canada, 2022.

[27] I Axelsson. Characterization of proteins and other macromolecules by agarose gel chromatography. *Journal of Chromatography A*, 152(1):21–32, 1978.

[28] HB Bohidar. Light scattering study of solution properties of bovine serum albumin, insulin, and polystyrene under moderate pressure. *Colloid and Polymer Science*, 267(4):292–300, 1989.

[29] D F Hanlon, I Saika-Voivod, M S G Razul, and G T Andrews. Probing the viscoelastic properties of aqueous protein solutions using molecular dynamics simulations. *arXiv preprint arXiv:2309.09119*, 2023.

[30] G Yan, S Monnier, M Mouelhi, and T Dehoux. Probing molecular crowding in compressed tissues with brillouin light scattering. *Proceedings of the National Academy of Sciences*, 119(4):e2113614119, 2022.

[31] MW Beijerinck. Concerning a contagium virum fluidum as cause of the spot disease of tobacco leaves. *Phytopathology Classics*, 7(1):33–52, 1898.

[32] A Mayer. Ueber die mosaikkrankheit des tabaks. *Die Landwirtschaftlichen Versuchs-Stationen*, 32:451–467, 1886.

[33] M Talati and P K Jha. *Physical Review E*, 73(1):011901, 2006.

[34] RD Hartschuh, SP Wargacki, H Xiong, J Neiswinger, A Kisliuk, S Sihn, V Ward, RA Vaia, and AP Sokolov. *Physical Review E*, 78(2):021907, 2008.

[35] S Sirotkin, A Mermet, M Bergoin, V Ward, and J L Van Etten. Viruses as nanoparticles: Structure versus collective dynamics. *Physical Review E*, 90(2):022718, 2014.

[36] V Sivanandam, D Mathews, and ALN Rao. *Virology*, 483:163–173, 2015.

[37] A McPherson. *Crystallization of Biological Macromolecules*, volume 586. Cold Spring Harbor Laboratory Press Cold Spring Harbor, NY, 1999.

[38] B W Matthews. Solvent content of protein crystals. *Journal of Molecular Biology*, 33(2):491–497, 1968.

[39] DLD Caspar, C Cohen, and W Longley. Tropomyosin: Crystal structure, polymorphism and molecular interactions. *Journal of Molecular Biology*, 41(1):87–107, 1969.

[40] C Cohen, DLD Caspar, DAD Parry, and RM Lucas. Tropomyosin crystal dynamics. In *Cold Spring Harbor Symposia on Quantitative Biology*, volume 36, pages 205–216. Cold Spring Harbor Laboratory Press, 1972.

[41] J D Bernal and D Crowfoot. X-ray photographs of crystalline pepsin. *Nature*, 133(3369):794, 1934.

[42] S Cohen. *Journal of Biological Chemistry*, 144(2):353–362, 1942.

[43] Z Kam, HB Shore, and G Feher. *Journal of Molecular Biology*, 123(4):539–555, 1978.

[44] R A Valverde and J A Dodds. *Journal of General Virology*, 68(4):965–972, 1987.

[45] B Stephanidis, S Adichtchev, P Gouet, A McPherson, and A Mermet. *Biophysical Journal*, 93(4):1354–1359, 2007.

[46] A McPherson and L J DeLucas. Microgravity protein crystallization. *Microgravity*, 1:15010, 2015.

[47] AJ Malkin, TA Land, Yu G Kuznetsov, A McPherson, and JJ DeYoreo. *Physical Review Letters*, 75(14):2778, 1995.

[48] AJ Malkin, Yu G Kuznetsov, W Glantz, and A McPherson. *The Journal of Physical Chemistry*, 100(28):11736–11743, 1996.

[49] TA Land, AJ Malkin, Yu G Kuznetsov, A McPherson, and JJ De Yoreo. *Physical Review Letters*, 75(14):2774, 1995.

[50] M Tachibana, K Kojima, R Ikuyama, Y Kobayashi, and M Ataka. *Chemical Physics Letters*, 332(3):259–264, 2000.

[51] A A Chernov. *Journal of Structural Biology*, 142(1):3–21, 2003.

Chapter 2

Theory

The work presented in this study uses inelastic light scattering spectroscopy as a means of probing acoustic phonons propagating in crystalline structures and aqueous solutions. The following section will describe the underlying theory and mechanics of inelastic light scattering of these systems.

2.1 Elastic Properties of Crystals

To describe elastic properties of a crystal, it is beneficial to treat the atoms as a series of masses on springs. For this example, we consider an atom whose position is defined by $r(R) = R + u(R)$, where R is the equilibrium position of the atom, and $u(R)$ is some displacement from equilibrium. Subsequently, the potential energy within the crystal is described by

$$U = \frac{1}{2}\sum_{RR'} \phi(r(R) - r(R')) = \frac{1}{2}\sum_{RR'} \phi(R - R' + u(R) - u(R')). \tag{2.1}$$

The Hamiltonian of such a system is given by

$$H = \sum_R \frac{P(R)^2}{2M} + U \tag{2.2}$$

where $P(R)$ is the momentum of an atom and M is the mass of an atom [1].

To find a solution for the harmonic approximation, we first expand the potential energy U using a Taylor series expansion [1]

$$\begin{gathered} U = \tfrac{N}{2} \textstyle\sum_R \phi(R) + \tfrac{1}{2} \textstyle\sum_{RR'} [u(R) - u(R')] \cdot \nabla\phi(R - R') + \\ \tfrac{1}{4} \textstyle\sum_{RR'} [\{u(R) - u(R')\} \cdot \nabla]^2 \phi(R'_R) + O(u^3). \end{gathered} \tag{2.3}$$

The linear term of Equation 2.3, $\sum_{RR'} \nabla\phi(R - R')$, is related to the force on an atom at position R at equilibrium. As such this term vanishes. The potential energy can be written as $U = U_{eq} + U_{harm}$, where U_{eq} is given by Equation 2.1 and U_{harm} is given by

$$U_{harm} = \frac{1}{4} \sum_{RR'} [u_\mu(R) - u_\mu(R')] \phi_{\mu\nu}(R - R') [u_\nu(R) - u_{nu}(R')] \tag{2.4}$$

where

$$\phi_{\mu\nu}(r) = \frac{\partial^2 \phi(r)}{\partial r_\mu \partial r_\nu}. \tag{2.5}$$

In matrix notation, U_{harm} is written as [1]

$$U_{harm} = \frac{1}{2} \sum_{RR'} u_\mu(R) D_{\mu\nu}(R - R') u_\nu(R'). \tag{2.6}$$

2.1.1 Normal Modes in a Lattice

To calculate the normal modes in a lattice, we begin with a monatomic one-dimensional chain of atoms whose Bravais lattice vectors are given by $R = na$. The harmonic potential energy is given by

$$U_{harm} = \frac{1}{2}K\sum_{n}[u(na) - u(\{n+1\}a)]^2 \tag{2.7}$$

where K is a spring constant, and the equation of motion is given by

$$M\ddot{u}(na) = -\frac{\partial U_{harm}}{\partial u(na)} = -K[2u(na) - u(\{n-1\}a) + u(\{n+1\}a)]. \tag{2.8}$$

If there is a finite number of atoms, we must obtain a method to describe motion at the ends of the chain. As such, we impose periodic boundary conditions $u([N+1]a) = u(a)$ and $u(0) = u(Na)$, where N is the length of the chain of atoms. This will yield a solution of the form $u(na,t) \propto e^{i(kna-\omega t)}$ where k is a wave vector. The periodic boundary condition requires $e^{ikNa} = 1$, thus

$$k = \frac{2\pi}{a}\frac{n}{N} \tag{2.9}$$

where $2\pi/a$ is the length of the first Brillouin zone. With these conditions, we may return to Equation 2.8, as

$$-M\omega^2 e^{i(kna-\omega t)} = -K(2 - e^{-ika} - e^{ika})e^{i(kna-\omega t)}. \tag{2.10}$$

From 2.10 we obtain the frequency of the normal mode for small values of k [1]

$$\omega = \left(a\sqrt{\frac{K}{M}}|k|\right). \tag{2.11}$$

Next, consider a Bravais lattice with two different ions per unit cell with positions na and $na + d$ and masses M_1 and M_2, respectively. We take $d \leq a/2$, such that $a - d \geq d$. As such, we obtain two equations of motion, one for each type of atom

$$M_1 \ddot{u}_1(na) = K[(]u_2(na) - 2u_1(na) + u_2(\{n-1\}a)] \tag{2.12}$$

$$M_2 \ddot{u}_2(na) = K[(]u_1(\{n+1\}a) - 2u_2(na) + u_1(na)] \tag{2.13}$$

As with the previous example, we seek solutions of the form $u_1(na,t) = \epsilon_1 e^{i(kna - \omega t)}$ and $u_2(na,t) = \epsilon_2 e^{i(kna - \omega t)}$. By substituting these expressions into Equations 2.12 and 2.13 we obtain an expression for normal mode vibrational frequency, as

$$\omega^2 = K\left(\frac{M_1 + M_2 \pm \sqrt{M_1^2 + 2M_1M_2\cos(ka) + M_2^2}}{M_1M_2}\right). \tag{2.14}$$

For small values of k, the solutions to Equation 2.14 become

$$\omega(k) = ka\sqrt{\frac{K}{2(M_1 + M_2)}} \tag{2.15}$$

and

$$\omega(k) = \sqrt{\frac{2K(M_1 + M_2)}{M_1M_2}}. \tag{2.16}$$

These two solutions correspond to two different phonon branches. Equation 2.15 corresponds to acoustic modes, while Equation 2.16 corrseponds to optical modes.

A simple phonon dispersion curve is shown in Figure 2.1. In this curve, the higher frequency branch corresponds to optical phonons, which are higher energy in nature, and the lower frequency branch corresponds to acoustic phonons. In three-dimensional crystals, it is important to consider the direction of propagation and the polarization direction. In a simple three-dimensional structure, polarization vectors are mutually

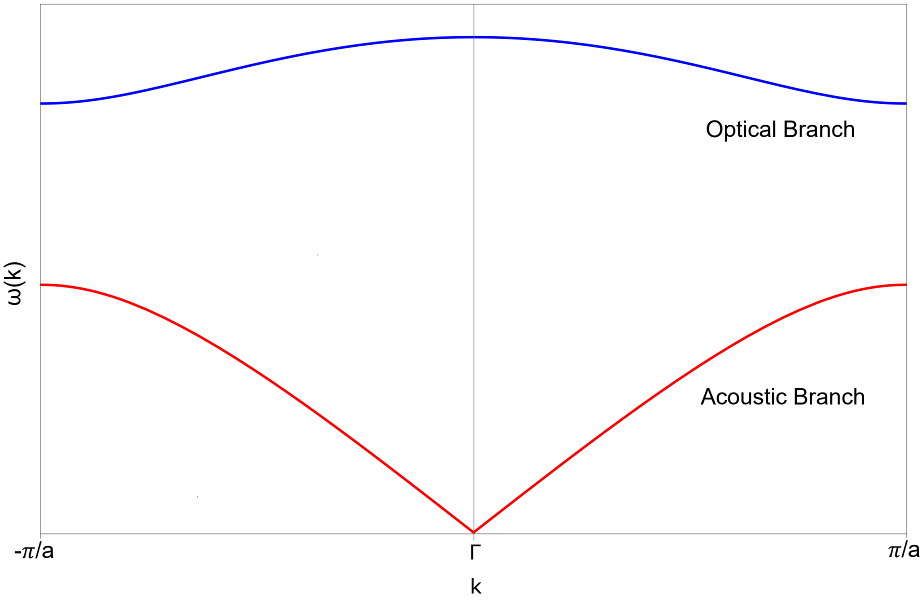

Figure 2.1: Simple diagram of a phonon dispersion curve for a one-dimensional chain with two different atoms in the unit cell.

perpendicular, aligning with the three principle directions. In anisotropic crystals, the polarization vector does not need to be so simply related to the direction of propagation, unless $\vec{k}$ is invariant under symmetry operations [1].

When expanding these concepts into three dimensions, we must adopt the matrix notation provided in Equation 2.6. To discuss normal modes of a three-dimensional atomic crystal, we may use the symmetries of the crystal to simplify the solutions to Equation 2.6.

Beginning with a monatomic three-dimensional crystal, there are 3N equations of motion, 3 equations for each N atom, of the form

$$M\ddot{u}_{\mu}(R) = -\frac{\partial U_{harm}}{\partial u_{\mu}(R)} = \sum_{R'\nu} D_{\mu\nu}(R - R')u_{\nu}(R'). \tag{2.17}$$

Analogous to the one-dimensional model, we seek a solution to the equation of motion of the form $\vec{u}(\vec{R},t) = \vec{\epsilon}e^{i(\vec{k}\cdot\vec{R}-\omega t)}$, where $\vec{\epsilon}$ is the polarization vector. As with the one dimensional case, we impose periodic boundary conditions $u(R + N_i a_i) = u(R)$. The allowed wave vectors of $\vec{k}$ are given by

$$\vec{k} = \frac{n_1}{N_1}\vec{b_1} + \frac{n_2}{N_2}\vec{b_2} + \frac{n_3}{N_3}\vec{b_3} \tag{2.18}$$

where $\vec{b_i}$ are reciprocal lattice vectors, with indices 1,2, and 3 representing three orthogonal directions. With $\vec{\epsilon}$ as an eigenvector, Equation 2.17 becomes

$$M\omega^2\vec{\epsilon} = D(\vec{k})\vec{\epsilon} \tag{2.19}$$

where $D(\vec{k})$ is a dynamical matrix given by $D(\vec{k}) = \sum_R D(R)e^{-i\vec{k}\cdot\vec{R}}$. $D(\vec{k})$ is an even function and real matrix, with eigenvectors ϵ_1, ϵ_2, and ϵ_3 which satisfy

$$D(\vec{k})\epsilon_s(\vec{k}) = \lambda_s\epsilon_s(\vec{k}) \tag{2.20}$$

and $\epsilon_s\epsilon_{s'} = \delta_{ss'}$. Thus we obtain three normal modes with wave vector $\vec{k}$, polarization vector $\vec{\epsilon_s}(\vec{k})$, and frequency

$$\omega_s = \sqrt{\frac{\lambda_s(\vec{k})}{M}}. \tag{2.21}$$

As with the one-dimensional case, when introducing a polyatomic basis to a three-dimensional crystal optical modes are also produced. 3N normal modes exist in polyatomic crystals, where N is the number of different types of atoms. These normal modes correspond to 3 acoustic modes and 3N-3 optical modes. As such, polarization vectors are no longer related by mutual orthogonality relations. Instead, if displacement of an ion is given by

$$\vec{u}_{s,i}(\vec{R},t) = Re[\vec{\epsilon_{s,i}}e^{i(\vec{k}\cdot\vec{R}-\omega t)}] \tag{2.22}$$

Table 2.1: Compression of tensor notation of elastic stiffness constants.

ij/kl	11	22	33	23,32	31,13	12,21
α/β	1	2	3	4	5	6

then polarization is chosen to satisfy the generalized 3p orthogonality relations

$$\sum_{i=1}^{p} \epsilon^{\dagger}_{s,i}(\vec{k}) \cdot \epsilon_{s',i}(\vec{k}) M_i = \delta s s'. \tag{2.23}$$

By introducing the strain tensor

$$\epsilon_{ij} = \frac{1}{2}\left(\frac{\partial}{\partial x_i} u_j + \frac{\partial}{\partial x_j} u_i\right) \tag{2.24}$$

it can be shown that U_{harm} [2] may be expressed as

$$U_{harm} = \frac{1}{2} \int dr \left[\sum \epsilon_{ij} c_{ijkl} \epsilon_{kl}\right] \tag{2.25}$$

where c_{ijlk} are elastic constants. To simplify this expression, we define the six possible combinations as shown in Table 2.1, thus generating a 6×6 matrix $C_{\alpha\beta} = c_{ijkl}$, with $\alpha = ij$ and $\beta = kl$.

2.1.2 Elasticity Tensor

If stress applied to a crystal is below the elastic limit, the strain is recoverable. In tensor notation, Hooke's law is given by

$$\varepsilon_{ij} = s_{ijkl} \sigma_{kl} \tag{2.26}$$

where ε_{ij} is longitudinal strain, s_{ijkl} is the elastic compliance constant, and σ_{kl} is the tensile stress. Alternatively, Hooke's law may be expressed as

$$\sigma_{ij} = c_{ijkl}\varepsilon_{kl} \tag{2.27}$$

where c_{ijkl} is the elastic stiffness constant, given by $c_{ijkl} = s_{ijkl}^{-1}$. Since s_{ijkl} and c_{ijkl} are fourth-rank tensors, they have 81 terms. However, introducing symmetry elements may reduce the number of independent terms [3].

As an example, shear stress σ_{12} cannot be applied without σ_{21}, which is equal. As such

$$\varepsilon_{11} = s_{1112}\sigma_{12} + s_{1121}\sigma_{21} = (s_{1112} + s_{1121})\varepsilon_{12}. \tag{2.28}$$

Thus s_{1112} and s_{1121} always occur together and cannot be separated. As such, we may say $s_{ijkl} = s_{ijlk}$. As a second example, consider uniaxial tension applied along the O_{x_3} direction. As such, $\varepsilon_{12} = s_{1233}\sigma_{33}$ and $\varepsilon_{21} = s_{2133}\sigma_{33}$. By the definition of the strain tensor, $\varepsilon_{12} = \varepsilon_{21}$, and therefore $s_{ijkl} = s_{jikl}$. From these two examples, it is apparent that $s_{ijkl} = s_{jikl} = s_{jilk} = s_{ijlk}$, and consequently $c_{ijkl} = c_{jikl} = c_{jilk} = c_{ijlk}$. This use of symmetry reduces the number of stiffness constants from 81 to 36, as ij and kl each have 6 unique combinations.

As in the classical treatment of elasticity, we can compress the tensor notation of Equations 2.26 and 2.27 according to Table 2.1. Therefore we may write the stress and strain tensors in matrix notation, as

$$\begin{bmatrix} \sigma_{11} & \sigma_{12} & \sigma_{13} \\ \sigma_{21} & \sigma_{22} & \sigma_{23} \\ \sigma_{31} & \sigma_{32} & \sigma_{33} \end{bmatrix} \rightarrow \begin{bmatrix} \sigma_1 & \sigma_6 & \sigma_5 \\ \sigma_6 & \sigma_2 & \sigma_4 \\ \sigma_5 & \sigma_4 & \sigma_3 \end{bmatrix} \tag{2.29}$$

and

$$\begin{bmatrix} \varepsilon_{11} & \varepsilon_{12} & \varepsilon_{13} \\ \varepsilon_{21} & \varepsilon_{22} & \varepsilon_{23} \\ \varepsilon_{31} & \varepsilon_{32} & \varepsilon_{33} \end{bmatrix} \rightarrow \begin{bmatrix} \varepsilon_1 & \frac{1}{2}\varepsilon_6 & \frac{1}{2}\varepsilon_5 \\ \frac{1}{2}\varepsilon_6 & \varepsilon_2 & \frac{1}{2}\varepsilon_4 \\ \frac{1}{2}\varepsilon_5 & \frac{1}{2}\varepsilon_4 & \varepsilon_3 \end{bmatrix}. \tag{2.30}$$

The factors of 1/2 are introduced as

- $s_{ijkl} = s_{mn}$ when m and n are 1, 2, or 3

- $2s_{ijkl} = s_{mn}$ when either m or n are 4, 5, or 6

- $4_{ijkl} = s_{mn}$ when both m and n are 4, 5, or 6.

As such we may now express Equations 2.26 and 2.27 as

$$\varepsilon_i = s_{ij}\sigma_j \tag{2.31}$$

and

$$\sigma_i = c_{ij}\varepsilon_j \tag{2.32}$$

where s_{ij} and c_{ij} are 6×6 matricies with 36 independent coefficients.

The number of independent coefficients of s_{ij} and c_{ij} may be reduced by the symmetry of a crystal. Some conditions may be deduced simply by the symmetry of a crystal, for example, c_{11}, c_{22} and c_{33} are related to propagation of transverse waves in a crystal. In a cubic crystal, the three principle directions are equivalent, and thus $c_{11} = c_{22} = c_{33}$. In other cases, one must take into account the interactions of stresses and strains along different directions in the crystal.

Further restrictions may be applied on elastic constants [4]. Strain on a crystal must be positive, or the crystal would be unstable. Furthermore $c_{ij}\varepsilon_i\varepsilon_j/2$ must be positive definite for all non-zero values of $\varepsilon_{i,j}$. These two conditions impose new restrictions on elastic constants based on symmetry. For example, in a cubic crystal, $c_{44} > 0$, $c_{11} > |c_{12}|$, and $c_{11} + 2c_{12} > 0$. For an icosahedral crystal, all nine elastic constants are independant.

2.2 Inelastic Light Scattering

Inelastic light scattering techniques are experimental techniques used to probe phonons propagating in materials. Such techniques use light in the visible spectrum. Since phonon wave vectors (10^5 cm^{-1}) are much smaller than the magnitude of the first Brillouin zone (10^8 cm^{-1}), probing occurs in the vicinity of $k = 0$ [1]. Examples of such scattering are Brillouin scattering, which probes acoustic phonons, and Raman scattering, which probes optical phonons.

Inelastic light scattering is governed by conservation of energy and momentum [5], as

$$\hbar\omega_s = \hbar\omega_i \pm \hbar\Omega \tag{2.33}$$

$$\hbar\vec{K}_s = \hbar\vec{K}_i \pm \hbar\vec{q} \tag{2.34}$$

where ω and $\vec{K}$ are the photon angular frequency and wave vector, respectively, Ω and $\vec{q}$ are the angular frequency and wave vector of the phonon, respectively, and the subscripts i and s denote the incident and scattered light.

2.2.1 Brillouin Scattering in Solids

Brillouin spectroscopy is an inelastic light scattering technique which is used to probe thermally excited acoustic phonons in a material. Brillouin scattering is governed by conservation of energy and momentum, given in Equations 2.34 and 2.33. Angular frequency, Ω of the phonon is given by

$$\Omega = 2\pi f = vq \tag{2.35}$$

where v is the speed of the phonon. Since v is significantly smaller than c, the speed of light, we can make the approximation that $\omega_s \simeq \omega_i$ and $k_s \simeq k_i$, where k is the magnitude of $\vec{K}$.

As an inelastic light scattering technique, Brillouin scattering probes acoustic phonons in a material. Bulk acoustic phonons, represented by $\vec{q_B}$ in Figure (2.2), are caused by fluctuations in the dielectric constant due to fluctuations in the strain field. Bulk modes are described with components parallel and perpendicular to the surface of the sample. The magnitudes of the components of the phonon wave vectors are given by

$$q_B^{\parallel} = n[k_i \sin\theta_i' + k_s \sin\theta_s'] \tag{2.36}$$

$$q_B^{\perp} = n[k_i \cos\theta_i' + k_s \cos\theta_s'] \tag{2.37}$$

where n is the refractive index of the material, and θ_i' and θ_s' are the incident and scattered internal angles of photons, provided by Snell's law. Combining Equations (2.36) and (2.37), the magnitude of the bulk phonons wave vector is

$$q_B = [(q_B^{\parallel})^2 + (q_b^{\perp})^2]^{\frac{1}{2}} = n[k_i^2 + k_s^2 + 2k_ik_s\{\sin\theta_i' \sin\theta_s' + \cos\theta_i' \cos\theta_s'\}]^{\frac{1}{2}}. \tag{2.38}$$

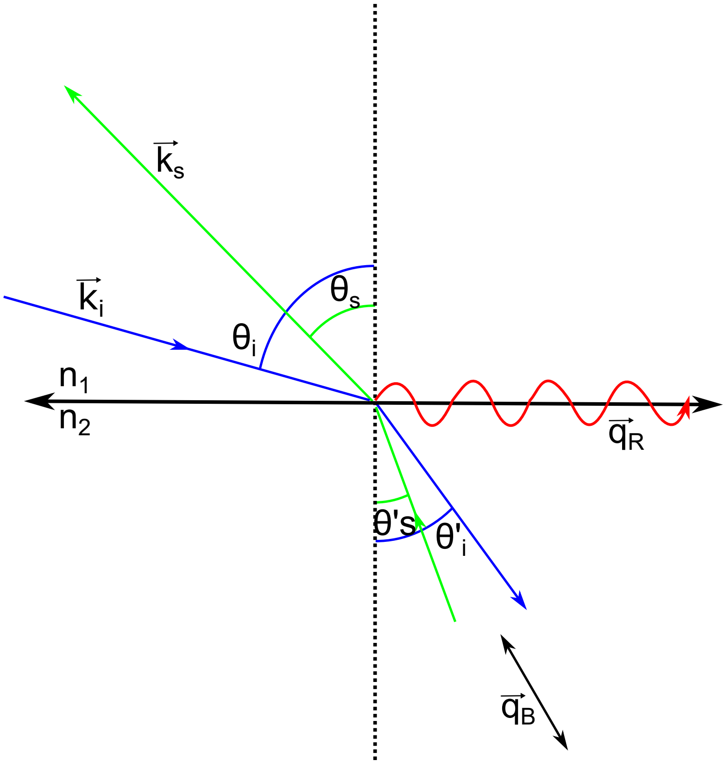

Figure 2.2: Diagram of vectors involved in Brillouin scattering process. $\vec{k_i}$ and $\vec{k_s}$ are the incident and scattered light wave vectors, θ_i, θ_s θ'_i, θ'_s are the external and internal incident and scattered light angles with respect to the normal of the sample, $\vec{q}_B$ is the bulk mode, and $\vec{q}_R$ is the Rayleigh surface mode.

Remembering that $k_s \simeq k_i$, Equation [2.38] may be expressed as

$$q_B = n[2k_i^2(1 + \sin\theta_i' \sin\theta_s' + \cos\theta_i' \cos\theta_s')]^{\frac{1}{2}}. \tag{2.39}$$

From here, it can be shown that

$$q_B = 2nk_i \cos\left(\frac{\theta_s' - \theta_i'}{2}\right). \tag{2.40}$$

In the case of 180° backscattering, as will be used in the proposed experiments, $\theta_s = \theta_i$, and consequently $\theta_s' = \theta_i'$, and therefore $q_B = 2nk_i$. By applying Equation (2.35), and the fact that $k = \frac{2\pi}{\lambda}$, the frequency of the bulk mode can be expressed as

$$f_B = \frac{2nv_B}{\lambda_i} \tag{2.41}$$

where λ_i is the wavelength of the incident photon. By rearranging Equation (2.41), one can solve for the velocity of the bulk mode as

$$v_B = \frac{f_B\lambda_i}{2n}. \tag{2.42}$$

There are two types of bulk modes which may occur in a material. These are transverse bulk modes, which are polarized in one of the directions perpendicular to the direction of propagation, and longitudinal bulk modes, which are polarized parallel to the direction of propagation.

There is another type of phonon produced in Brillouin scattering which propagates along the surface of the material. This is called the Rayleigh surface mode, and is primarily seen in spectra taken from opaque materials. The Rayleigh surface mode is caused by deformations on the sample surface, represented by $\vec{q}_R$ in Figure (2.2).

These surface modes decay very rapidly into the bulk of the material, so the only component that is considered is parallel to the surface of the material. The magnitude of the surface mode wave vector can therefore be expressed as just the parallel component, similar to Equation (2.36).

$$q_R = q_R^{\|} = k_i \sin\theta_i + k_s \sin\theta_s \tag{2.43}$$

Since $\theta_s = \theta_i$ in 180° backscattering, and $k_s \simeq k_i$, Equation (2.43) becomes

$$q_R = 2k_i \sin\theta_i. \tag{2.44}$$

The frequency of the Rayleigh surface mode is therefore given by

$$f_R = \frac{2v_R \sin\theta_i}{\lambda_i}. \tag{2.45}$$

Again, one may solve for the velocity of the surface mode as

$$v_R = \frac{f_R \lambda_i}{2\sin\theta_i}. \tag{2.46}$$

A typical Brillouin spectrum consists of peaks due to transverse bulk modes, longitudinal bulk modes, and sometimes Rayleigh surface modes. A simple schematic of a Brillouin spectrum is shown in Figure (2.3). The central peak occurs at the frequency of the incident laser, with an assigned frequency shift of 0 GHz, and Brillouin peaks occur at frequencies on the order of tens of GHz shifted from the reference beam. To the left of the reference peak are the peaks caused by Stokes scattering, wherein a phonon is generated, and to the right of the central peak are the peaks corresponding to anti-Stokes scattering events, wherein a phonon is annihilated. In accordance with

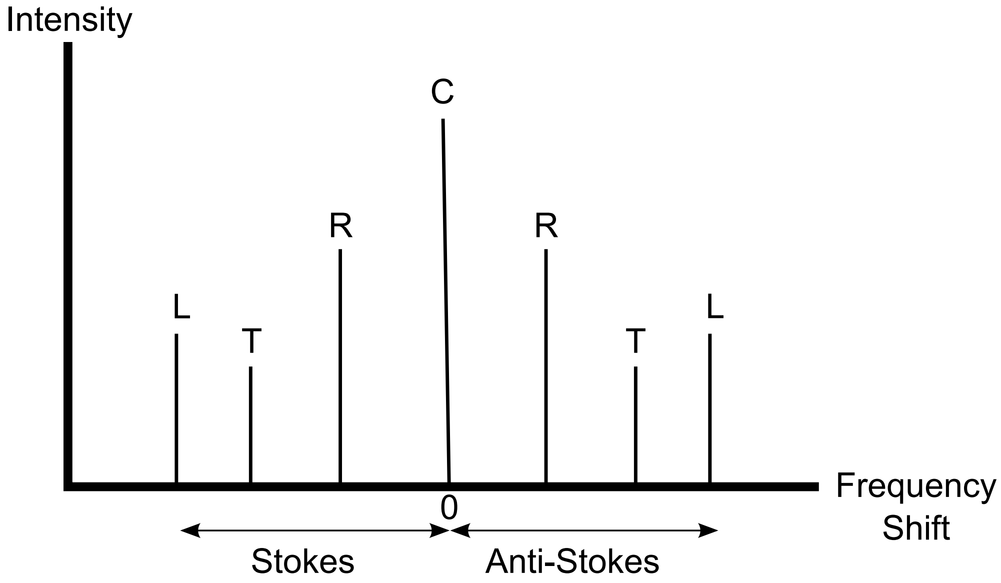

Figure 2.3: Schematic of a typical Brillouin spectrum. C is the central elastic peak, R is due to the Rayleigh surface mode, T is due to the transverse bulk mode, and L is due to the longitudinal bulk mode.

Equation (2.45), the frequency shift of the surface mode, labeled as R in Figure (2.3), depends on the angle of incidence. The frequency shift of the surface mode increases with increasing angle of incidence. The frequency shifts of peaks corresponding to the bulk modes, represented by T and L in Figure (2.3). The frequency shift of bulk modes depends on the direction being probed within the crystal. In opaque materials, a large change in the external angle of incidence corresponds to a small change in internal angle, by Snell's law. As such, probing direction experiences very little variation, and the frequency of bulk modes may be treated as independent of angle of incidence.

2.3 Brillouin Scattering in Liquids

2.3.1 Phonon Propagation in Liquids

Similar to phonon propagation in crystals, phonon velocity in liquids can be expressed as

$$v_s = \sqrt{\frac{B}{\rho}} = \sqrt{\frac{1}{\chi_s \rho}} \tag{2.47}$$

where B is the bulk modulus, χ_s is the adiabatic compressibility, and ρ is the density of the liquid. For liquids, the main contribution to phonon velocity is compressibility, given by

$$\chi_s = \frac{1}{\rho}\left(\frac{\partial \rho}{\partial P}\right)_s = -\frac{1}{V}\left(\frac{\partial V}{\partial P}\right)_s . \tag{2.48}$$

Adiabatic compressibility of a liquid, effectively, determines the ease by which the compressions of groups of molecules may occur, which subsequently determines the ease of propagation of phonons [6].

There is, however, a critical point at which the compressibility of the fluid diverges. At such a point, by equation 2.47, phonon velocity v_s tends to zero, and subsequently phonon frequency also tends to zero, as

$$\omega_s = v_s q. \tag{2.49}$$

As phonons propagate throughout a liquid, the intensity of the wave dissipates over distance. There are two major contributions to this dissipation; viscosity and thermal conduction. As such, we may discuss a characteristic lifetime τ as being directly related to thermal conductivity, κ, bulk viscosity, η_b, and shear viscosity, η_S due to dissipation processes in the fluid. From a Brillouin spectrum, characteristic lifetime may be found from

$$\Gamma = 2\alpha v_s = \frac{2}{\tau} \tag{2.50}$$

where Γ is the Brillouin peak linewidth and α is the hypersound absorption coefficient [6].

2.3.2 Inelastic Light Scattering in Liquids

In order to discuss light scattered inelastically from a liquid, we must first derive a spectral density function $S_{\rho\rho}(\vec{q}, \omega)$, a function which describes the Brillouin spectra as a function of frequency. There are two important contributions which must be discussed in order to derive such an equation; the thermodynamic contribution and the hydrodynamic contribution [6].

To begin discussion of the thermodynamic contribution to the spectral density function, we must first consider conservation laws for the system, these being conservation of mass, momentum, and energy [6]. To start with conservation of mass, we must first consider the total number of particles in a volume V as

$$N(t) = \int_V d^3r\, \rho_n(\vec{r}, t) \tag{2.51}$$

and thus the rate of change of $N(t)$ is

$$\frac{dN(t)}{dt} = \int_V d^3r\, \frac{\partial \rho_n(\vec{r}, t)}{\partial t} \tag{2.52}$$

where $\rho_n(\vec{r}, t)$ is the time dependent local number density of particles within the liquid. Following conservation of mass, the rate of change of $N(t)$ must be such that the number of particles entering V is the same as the number of particles leaving V.

As such, we may introduce the flux of particles $\vec{J}$, and say

$$\frac{\partial \rho_n(\vec{r},t)}{\partial t} + \nabla \cdot \vec{J}(\vec{r},t) = 0. \tag{2.53}$$

The only way in which the number of particles contained within volume V may change is by diffusion through the surface S which encompasses V. As such, we may define the outward volume flow as $\vec{u}_B(\vec{r},t) \cdot d\vec{S}$, where $\vec{u}_B(\vec{r},t)$ is the Brownian particle velocity, and $d\vec{S}$ is the volume surface element. To find the total change in the number of particles in this volume due to convection, we can integrate over $\vec{S}$. Furthermore, since there are no other contributions to the change in number of particles, this integral over $\vec{S}$ can be equated to the right side of Equation 2.52, and subsequently

$$\int_V d^3r \, \frac{\partial \rho_n(\vec{r},t)}{\partial t} = \int_S \rho_n(\vec{r},t)\vec{u}_B(\vec{r},t) \cdot d\vec{S}. \tag{2.54}$$

Next, we must discuss conservation of momentum within the volume V. Similar to conservation of mass, we may define the momentum vector $\vec{G}(t)$ and the momentum density vector $\vec{g}(\vec{r},t)$ such that

$$\vec{G}(t) = \int_V d^3r \, \vec{g}(\vec{r},t). \tag{2.55}$$

and conservation of momentum may be defined as

$$\frac{\partial \vec{g}_i(\vec{r},t)}{\partial t} + \nabla_j \cdot \vec{\tau}_{ij}(\vec{r},t) = 0. \tag{2.56}$$

where $\vec{\tau}_{ij}(\vec{r},t)$ is the momentum flux tensor. There are two major contributions to changes of momentum within the volume V [6]. The first is convection of particles through the surrounding surface S. This may be expressed as

$$-\int_s \vec{g}(\vec{r},t)\vec{u}_B(\vec{r},t)\cdot d\vec{S}. \tag{2.57}$$

The second factor which may affect momentum is an external force provided by fluid surrounding the volume V, such that

$$d\vec{F} = \vec{\sigma}\cdot d\vec{S} \tag{2.58}$$

where $\vec{\sigma}$ is the stress tensor. As such, we may express change in momentum as

$$\frac{d\vec{G}(t)}{dt} = \int_V d^3r\,\frac{\partial\vec{g}(\vec{r},t)}{\partial t} = \int_S \left[\vec{\sigma}(\vec{r},t) - \vec{g}(\vec{r},t)\vec{u}_B(\vec{r},t)\right]\cdot d\vec{S}. \tag{2.59}$$

Furthermore, $\vec{g}(\vec{r},t)$ may be expressed as $m\rho_n(\vec{r},t)\vec{u}_B(\vec{r},t)$, therefore

$$\int_V d^3r\,\frac{\partial\vec{g}(\vec{r},t)}{\partial t} = \int_S \left[\vec{\sigma}(\vec{r},t) - m\rho_n(\vec{r},t)\vec{u}_B(\vec{r},t)\vec{u}_B(\vec{r},t)\right]\cdot d\vec{S}. \tag{2.60}$$

Finally, in the discussion of thermodynamic processes, we must discuss conservation of energy [6]. As before, we can define energy $E(t)$ and energy density $e(\vec{r},t)$ such that

$$E(t) = \int_V d^3r\, e(\vec{r},t) \tag{2.61}$$

and the equation for conservation of energy can be written as

$$\frac{\partial e(\vec{r},t)}{\partial t} + \nabla\cdot\vec{J}_e(\vec{r},t) = 0 \tag{2.62}$$

where $\vec{J}_e(\vec{r},t)$ is the energy flux. There are several factors attributed to changes in energy within the volume V. The first factor is energy due to convection of particles through surface S, expressed as

$$-\int_s e(\vec{r},t)\vec{u}_B(\vec{r},t)\cdot d\vec{S}. \tag{2.63}$$

Next, we consider the work done on the surface S by surrounding liquid as

$$\vec{u}_B(\vec{r},t)\cdot d\vec{F} = \vec{u}_B(\vec{r},t)\cdot\vec{\sigma}\cdot d\vec{S}. \tag{2.64}$$

Finally, we consider the heat diffusing into $d\vec{S}$ as $-\vec{Q}(\vec{r},t)\cdot d\vec{S}$. As such, we define the change in energy as

$$\frac{dE(t)}{dt} = \int_V d^3r\,\frac{\partial e(\vec{r},t)}{\partial t} \tag{2.65}$$

and subsequently

$$\int_V d^3r\,\frac{\partial e(\vec{r},t)}{\partial t} = \int_S [\vec{u}_B(\vec{r},t)\cdot\vec{\sigma}(\vec{r},t) - e(\vec{r},t)\vec{u}_B(\vec{r},t) - \vec{Q}(\vec{r},t)]\cdot d\vec{S}. \tag{2.66}$$

The derivations above lay the foundation for our three major conservation laws, matter, momentum, and energy. From here, we may now proceed with calculation of a Brillouin spectrum with the use of hydrodynamics [6]. Firstly, the fluxes of number of particles, momentum, and energy may be written as

$$\vec{J}(\vec{r},t) = \rho_n(\vec{r},t)\vec{u}_B(\vec{r},t) \tag{2.67}$$

$$\tau_{ij} = m\rho_n(\vec{r},t)\vec{u}_{Bi}(\vec{r},t)\vec{u}_{Bj}(\vec{r},t) - \sigma_{ij}(\vec{r},t) \tag{2.68}$$

$$\vec{J}_e(\vec{r},t) = e(\vec{r},t)\vec{u}_B(\vec{r},t) + \vec{Q}(\vec{r},t) - \vec{u}_B(\vec{r},t)\cdot\vec{\sigma}(\vec{r},t). \tag{2.69}$$

Equations 2.53, 2.56, and 2.62 can therefore be expressed as

$$\frac{\partial \rho_n(\vec{r},t)}{\partial t} + \nabla \cdot [\rho_n(\vec{r},t)\vec{u}_B(\vec{r},t)] = 0. \tag{2.70}$$

$$\frac{\partial \vec{g}_i(\vec{r},t)}{\partial t} + \nabla_j \cdot [m\rho_n(\vec{r},t)\vec{u_{Bi}}(\vec{r},t)\vec{u}_{Bj}(\vec{r},t) - \sigma_{ij}(\vec{r},t)] = 0. \tag{2.71}$$

$$\frac{\partial e(\vec{r},t)}{\partial t} + \nabla \cdot [e(\vec{r},t)\vec{u}_B(\vec{r},t) + \vec{Q}(\vec{r},t) - \vec{u}_B(\vec{r},t) \cdot \vec{\sigma}(\vec{r},t)] = 0. \tag{2.72}$$

While the expression for particle flux in equation 2.67 is relatively straightforward, the expressions given in equations 2.68 and 2.69 must be expanded upon [6]. Starting with the momentum flux $\tau_{ij}(\vec{r},t)$, the stress tensor $\sigma_{ij}(\vec{r},t)$ may be expressed as

$$\sigma_{ij}(\vec{r},t) = -p\delta_{ij} + \sigma'_{ij}(\vec{r},t) \tag{2.73}$$

where $p\delta_{ij}$ is the pressure component of the stress tensor, and $\sigma'_{ij}(\vec{r},t)$ is the viscous shear term, given by the Newtonian stress tensor

$$\sigma'_{ij}(\vec{r},t) = \eta_s[\nabla_i u_{Bj}(\vec{r},t) + \nabla_j u_{Bi}(\vec{r},t) - \frac{2}{3}\nabla \cdot \vec{u}_B(\vec{r},t)\delta_{ij}] + \eta_b \nabla \cdot \vec{u}_B(\vec{r},t)\delta_{ij} \tag{2.74}$$

where η_s is the shear viscosity and η_b is the bulk viscosity. From here, we may therefore express the momentum flux tensor τ_{ij} as

$$\begin{gathered} \tau_{ij} = m\rho_n(\vec{r},t)\vec{u}_{Bi}(\vec{r},t)\vec{u}_{Bj}(\vec{r},t) - p\delta_{ij} + \eta_s[\nabla_i u_{Bj}(\vec{r},t) + \\ \nabla_j u_{Bi}(\vec{r},t) - \tfrac{2}{3}\nabla \cdot \vec{u}_B(\vec{r},t)\delta_{ij}] + \eta_b \nabla \cdot \vec{u}_B(\vec{r},t)\delta_{ij}. \end{gathered} \tag{2.75}$$

To expand the energy flux term $\vec{J}_e(\vec{r},t)$, we must consider two contributions; a kinetic contribution and the internal energy density [6]. As such

$$e(\vec{r},t) = \frac{1}{2} m\rho_n(\vec{r},t) u_B^2(\vec{r},t) + e'(\vec{r},t) \tag{2.76}$$

where $e'(\vec{r},t)$ is the aforementioned internal energy density. Furthermore, the diffusive heat flux $Q(\vec{r},t)$ can be expressed as

$$Q(\vec{r},t) = -\kappa \nabla T(\vec{r},t) \tag{2.77}$$

where κ is the thermal conductivity and $\nabla T(\vec{r},t)$ is the temperature gradient [6]. Therefore we may now express equation 2.69 as

$$\vec{J}_e = \left(\frac{1}{2} m\rho_n(\vec{r},t) u_B^2(\vec{r},t) + e'(\vec{r},t)\right)\vec{u}_B(\vec{r},t) - \kappa \nabla T(\vec{r},t) - \vec{u}_B(\vec{r},t)\cdot\vec{\sigma}(\vec{r},t). \tag{2.78}$$

From here, we must make some assumptions about the system in question. First, we assume that fluctuations in thermodynamic properties are small. Next, we assume that all properties previously shown can be expressed as some equilibrium value plus a fluctuation. For example, particle density may be expressed as $\rho_n(\vec{r},t) = \rho_0 + \rho_1(\vec{r},t)$. Such notation will also be used for other variables in the following derivations. Furthermore, we only take into account first order fluctuations. We can also define the equilibrium velocity $\vec{u}_0$ to be zero, since the system is at rest at equilibrium [6]. With these considerations in place, expressions for the rate of change particle density, momentum density, and energy density may be shown to be

$$\frac{\partial \rho_1(\vec{r},t)}{\partial t} = -\rho_0 \nabla \cdot \vec{u}_1(\vec{r},t) \tag{2.79}$$

$$m\rho_0 \frac{\partial \vec{u}_1(\vec{r},t)}{\partial t} = -\nabla p_1(\vec{r},t) + \eta_s \nabla^2 \vec{u}_1(\vec{r},t) + (\eta_b + \frac{1}{3}\eta_s)\nabla[\nabla \cdot \vec{u}_1(\vec{r},t)] \tag{2.80}$$

$$\frac{\partial e_1(\vec{r},t)}{\partial t} = \kappa \nabla^2 T_1(\vec{r},t) - (e_0 + p_0)\nabla \cdot \vec{u}_1(\vec{r},t). \tag{2.81}$$

Using Equation 2.79 to eliminate the $\nabla \cdot \vec{u}_1(\vec{r},t)$ term from equation 2.81, it may be written as a function of entropy fluctuation, such that [6]

$$T_0 \frac{\partial s_1(\vec{r},t)}{\partial t} = \kappa \nabla^2 T_1(\vec{r},t), \tag{2.82}$$

where

$$s_1 = \frac{1}{T_0}\left(e_1 - \frac{e_0 + p_0}{\rho_0} p_1\right) \tag{2.83}$$

From here, we must introduce pressure and entropy terms, p_1 and s_1, such that

$$p_1 = m v_T^2 (\rho_1 \alpha \rho_0 T_1) \tag{2.84}$$

$$s_1 = -\frac{m \rho_0 c_V}{T_0}\left(\frac{\gamma - 1}{\alpha \rho_0}\rho_1 - T_1\right) \tag{2.85}$$

where v_T is the isothermal speed of sound, α is the thermal expansion coefficient, c_V is the volumetric specific heat capacities, and γ is the ratio of specific heat capacities c_P/c_V. To further simplify formulae, we will introduce new terms, such that $\Psi(\vec{r},t) = \nabla \cdot \vec{u}_1(\vec{r},t)$, $D_v = (\eta_b + \frac{4}{3}\eta_s)/m\rho_0$, and $D_T = \kappa/m\rho_0 c_P$. From here, we may write new expressions for the conservation equations.

$$\frac{\partial \rho_1(\vec{r},t)}{\partial t} + \rho_0 \Psi_1(\vec{r},t) = 0 \tag{2.86}$$

$$\frac{\partial \Psi_1(\vec{r},t)}{\partial t} = \frac{v_T^2}{\rho_0}\nabla^2 \rho_1(\vec{r},t) + \alpha v_T^2 \nabla^2 T_1(\vec{r},t) - D_V \nabla^2 \Psi_1(\vec{r},t) = 0 \tag{2.87}$$

$$\frac{\partial T_1(\vec{r},t)}{\partial t} - \frac{\gamma - 1}{\alpha \rho_0} - \gamma D_T \nabla^2 T_1(\vec{r},t) = 0 \tag{2.88}$$

In order to finally set up these equations to create the spectral density function $S_{\rho\rho}(\vec{q},\omega)$, we must take the Fourier-Laplace transforms of the remaining variables, such that $\rho_1(\vec{r},t) \rightarrow \rho_1(\vec{q},\omega)$, $T_1(\vec{r},t) \rightarrow T_1(\vec{q},\omega)$, and $\Psi_1(\vec{r},t) \rightarrow \Psi_1(\vec{q},\omega)$. These solutions are then multiplied by the complex conjugates of each variable to give a full set of correlation functions for density and temperature, as well as their Laplace transforms and their complex conjugates.

Next, we define the structure factor to be

$$S(\vec{q}) = \left\langle \rho_1^{\dagger}(\vec{q}) \rho_1(\vec{q}) \right\rangle \tag{2.89}$$

To first order approximation, the density-density correlation function is

$$\frac{\left\langle \rho_1^{\dagger}(\vec{q},0) \rho_1(\vec{q},t) \right\rangle}{\left\langle \rho_1^{\dagger}(\vec{q},0) \rho_1(\vec{q},0) \right\rangle} = \left(1 - \frac{1}{\gamma}\right) e^{-q^2 D_T |t|} + \frac{1}{\gamma} e^{-q^2 \Gamma |t| \cos(\omega_B(q)|t|)} + \frac{b(q)}{\gamma} e^{-q^2 \Gamma |t| \sin(\omega_B(q)|t|)} \tag{2.90}$$

where $b(q)$ is given by

$$b(q) = \frac{q(3\Gamma - D_V)}{\gamma c_s} \tag{2.91}$$

and Γ is the classical attenuation coefficient, given by

$$\Gamma = \frac{1}{2}[(\gamma - 1) D_T + D_V] \tag{2.92}$$

Finally, an expression for the spectral density function can be obtained by taking the Laplace transform of equation 2.90. Thus

$$\begin{aligned} S_{\rho\rho}(\vec{q},\omega) = \tfrac{1}{\pi} V\rho^2 k_B T \chi_T \Bigg\{ & \left(1-\tfrac{1}{\gamma}\right)\left[\tfrac{D_T q^2}{\omega^2+(D_T q^2)^2}\right] \\ & +\tfrac{1}{\gamma}\left(\tfrac{\Gamma q^2}{[\omega-\omega_B(q)]^2+[\Gamma q^2]^2}+\tfrac{\Gamma q^2}{[\omega+\omega_B(q)]^2+[\Gamma q^2]^2}\right) \\ & +\tfrac{b(q)}{\gamma}\left(\tfrac{\omega+\omega_B}{[\omega+\omega_B(q)]^2+[\Gamma q^2]^2}-\tfrac{\omega-\omega_B}{[\omega+\omega_B(q)]^2+[\Gamma q^2]^2}\right)\Bigg\}. \end{aligned} \tag{2.93}$$

This expression for $S_{\rho\rho}(\vec{q},\omega)$ defines the structure of the Brillouin spectrum. There are three terms present in the above expression. The first term in the expression, in the first line, represents the central elastic mode of a Brillouin spectrum, shown in figure 2.3. The terms in the second line characterize the Lorentzian curves from the Stokes and anti-Stokes longitudinal Brillouin peaks. Finally, the terms in the final line represents S-shaped curves centered at $\pm\omega_B$. These peaks cause slight asymmetries in the longitudinal Brillouin peaks, on the low frequency side, between the longitudinal peak and the central peak [6].

2.3.3 Relaxation

The physics of a Brillouin spectrum of a molecular solution is largely the same as that of a monatomic liquid, as previously discussed. However there are additional relaxation processes occurring within the liquid. A relaxation mode appears in a Brillouin spectrum as a weak and broad peak that is centered at zero frequency shift. Therefore, a relaxation mode can be observed by an increase in the background level of a Brillouin spectrum, primarily in the low frequency region.

There are primarily two types of relaxations occurring in molecular liquids which may be observed by means of Brillouin scattering, the first of which are thermal relaxations. These occur when there is energy transfer between the translational and intramolecular degrees of freedom. This relaxation can be explained via the frequency dependent bulk viscosity, $\eta_b(\omega)$, as

$$\eta_b(\omega) = \eta_b(v_\infty^2 - v_0^2)(1 + i\omega\tau_R)^{-1}\tau_R \tag{2.94}$$

where τ_R is relaxation time. v_∞ and v_0 are the infinite frequency and zero frequency phonon velocities, where the longitudinal bulk mode velocity falls within this range. These terms are present in equation 2.94 as dispersion terms due to the molecules' inability to follow pressure fluctuations at high frequencies. When phonon frequency, ω, is on the order of τ^{-1}, $\eta_b(\omega)$ becomes highly dependent on phonon frequency. Relaxation modes due to thermal relaxations have a large width, extending beyond the longitudinal peaks, and can be observed by an asymmetry in the Brillouin peaks on the low frequency side [6].

The second type of common relaxation which may be observed in Brillouin scattering is a structural relaxation. These relaxations only occur in highly viscous solutions. Their appearance in a spectrum is almost identical to that of a thermal relaxation. Furthermore, the width of structural relaxation mode is proportional to $1/\tau_R$. So when the relaxation time is too low, the peak becomes too broad to be observed. When the relaxation time is too high, the peak becomes extremely sharp, and can become hidden by the elastic peak of the Brillouin spectrum. As such, there is a limited range in which structural relaxations may be observed. Furthermore, the origin of a relaxation mode cannot be inferred from Brillouin scattering alone, and therefore requires the use of other techniques to be properly identified [6].

2.4 Elasstic and Viscoelastic Properties Derived from Brillouin Spectra

In the present work, elastic and viscoelastic properties will be calculated Brillouin scattering results. Specifically, Brillouin peak frequency and linewidth will be used to calculate these properties. Firstly, by means of Equation 2.42 from Section 2.2.1, Brillouin peak frequency will be used to calculate hypersound velocity for both aqueous and crystal systems. Similarly, Equation 2.47 will be used for both aqueous and crystal systems to calculate bulk modulus, as

$$B = \rho v^2. \tag{2.95}$$

For all materials studied within this work, hypersound attenuation will be calculated by

$$\alpha = \frac{\pi \Gamma_B}{v} \tag{2.96}$$

where Γ_B is the bulk mode linewith, as calculated from the peak in the Brillouin spectrum. For STMV crystals, the normalized attenuation parameter, Λ, is calculated using

$$\Lambda = \frac{\pi \Gamma_B}{f}. \tag{2.97}$$

Finally, for aqueous macromolecular solutions studies in this work, Brillouin peak frequency and linewidth will be used to calculate apparent viscosity, eta, as

$$\eta = \frac{4}{3}\eta_s + \eta_b = \frac{\rho v^2 \Gamma_B}{4\pi^2 f^2} = \frac{\rho \lambda^2 \Gamma_B}{16\pi^2 n^2}. \tag{2.98}$$

Bibliography

[1] N.W. Ashcroft and N.D. Mermin. *Solid State Physics*. Saunders College, Philadelphia, 1976.

[2] MP Marder. *Condensed Matter Physics*. John Wiley & Sons, 2010.

[3] J F Nye. *Physical Properties of Crystals: Their Representation by Tensors and Matrices*. Oxford University Press, London, UK, 1985.

[4] W L Ferrar. Algebra; a text-book of determinants, matrices, and algebraic forms. Technical report, 1941.

[5] H. Z. Cummings and P. E. Schoen. *Light Scattering from Thermal Fluctuations*, volume 2. John Wiley and Sons, North-Holland, New York, 1972.

[6] D WN Edington. Spectroscopic studies of anomalous hydrodynamic behaviour in complex fluids. 2002.

Chapter 3

Experimental Methods

3.1 Growth of STMV Crystals

The experimental process of STMV crystallization in this study begins with infection of tobacco plants with STMV and its helper virus TMV. Tobacco plants were initially sowed and germinated in the Memorial University Botanical Gardens, and transferred to our lab at roughly two weeks old. In the lab, we were able to keep the plants alive and healthy for several months using the setup shown in Figure 3.1. As such, the only factor affecting the health of the plants were the viruses used in this study. Once the plants had been received, we infected the plants by swabbing leaves with infected plant material. Infected plant material was originally obtained from Dr. Ayala Rao at University of California Riverside. After the first batch of plants were infected, leftover infected plant material was also used to infect subsequent batches of plants. Infection was allowed to propagate through the plant for roughly two weeks, as the leaves of the tobacco plants became mottled, shown in Figure 3.2.

Harvesting of virus particles was done via centrifugation. Infected leaves were

Figure 3.1: Tobacco plants growing under lamp.

ground using a mortar and pestle. This ground paste was added to a centrifugal cell, and topped off with deionized water. An Amicon Ultra-4 10K centrifugal filter tube, shown in Figure 3.3m was used for the centrifugation process. This tube has a filter within it with a maximum filtration size of 10 kDa. STMV has an atomic mass of 6.3 kDa, and as such can pass through the filter. The atomic mass of TMV is 126 kDa, and as such we can ensure the resulting solutions were be purely STMV in deionized water.

Centrifugation was performed using an IEC Clinical bench-top centrifuge with a six place fixed angle 45° rotor. Centrifugation was performed at a maximum speed of 4450 RPM, with a centrifugal force of 2400 × g, for a minimum of four hours. In subsequent experimental works, STMV solutions were further centrifuged one or two extra times to ensure higher purity of solution.

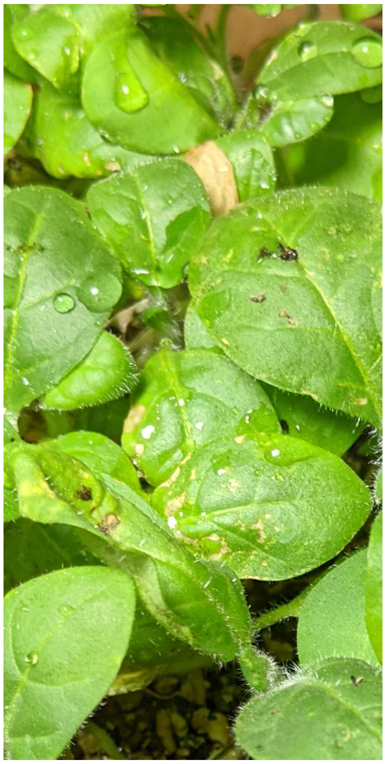

Figure 3.2: Mottling effect in tobacco leaves.

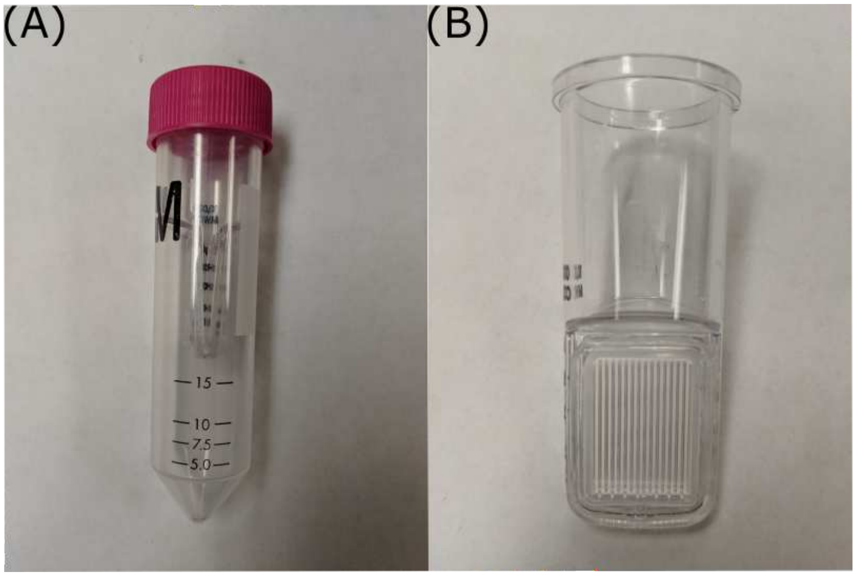

Figure 3.3: (A) Centrifuge cell used to separate STMV particles from TMV and leaf molecules. (B) Filter used in cell to separate STMV.

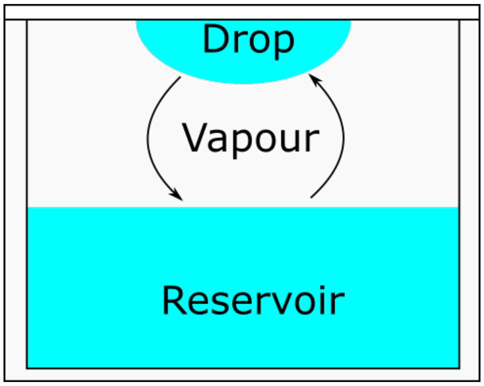

Figure 3.4: Schematic of hang drop vapour diffusion technique for crystal growth.

Crystallization of STMV solution was performed using a hang-drop vapour diffusion technique, schematic of which is shown in Figure 3.4. This is a technique which is commonly used in macromolecular crystallization, wherein a droplet containing virus particles, buffer solutions, and a precipitant, often a salt, is suspended over a reservoir solution of similar buffers and precipitants. Through transfer of vapour between the droplet and the reservoir, the two are able to equilibriate. The concentration of virus in the droplet begins low, but increases as the volume of the droplet decreases through equilibiation with the reservoir. As the concentration of virus particles in the drop increases, so to do the number of interactions between particles. This leads to crystal growth within the droplet.

Crystallization of STMV in this work was performed using the methods described by Valverde and Dodds [1]. Solutions of $(NH_4)_2SO_4$ were prepared by dissolving $(NH_4)_2SO_4$ powder in deionized water. While different concentrations were used in preliminary crystal growth attempts, the most consistent results were obtained using a 10% saturated solution of $(NH_4)_2SO_4$. 2-3 mL of $(NH_4)_2SO_4$ were used to fill the base of the vapour diffusion chamber, to be used as the reservoir. Equal volumes of $(NH_4)_2SO_4$ solution and STMV solution were mixed together to create the drop solution. Small droplets of this solution, on the order of 10-50 μL, were carefully

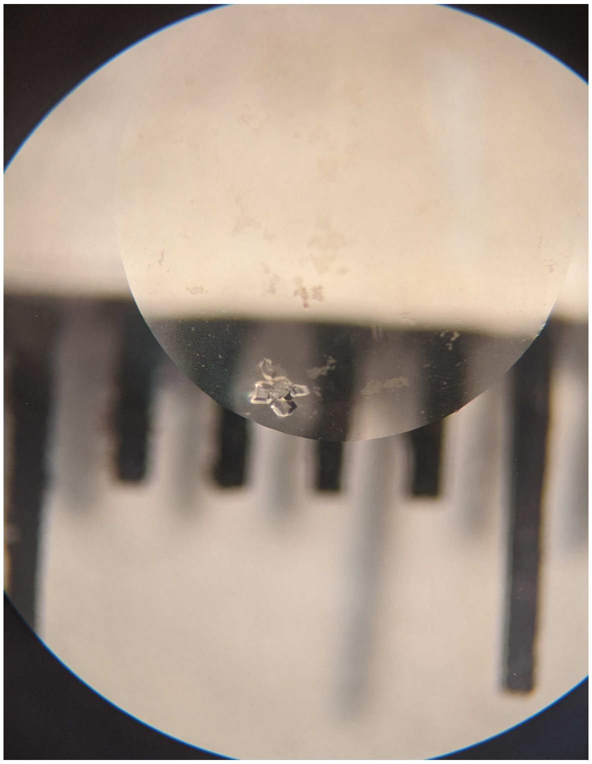

Figure 3.5: STMV crystal cluster viewed under a microscope. Tick marks in background represent one millimeter.

placed on the lid of the vapour diffusion chamber. The lid was then carefully flipped and placed onto the vapour diffusion chamber, ensuring that the droplets were not disturbed or moved in the process. Crystals were left for two weeks to grow.

Crystals grown by this method were polycrystalline clusters with cross sections up to a few hundred micrometers, as shown in Figure 3.5.

STMV crystals grown by the above method were extremely brittle and fragile. Any attempts to remove the crystals from the lid of the vapour diffusion cell resulted in complete destruction of the crystal. As such, subsequent crystals were grown on silicon substrates to enable transfer of STMV crystals to the Brillouin scattering apparatus.

Small pieces of silicon were cleaved from a larger <100> oriented piece of silicon, and were adhered to the lid of the vapour diffusion cell. A small scratch was made in

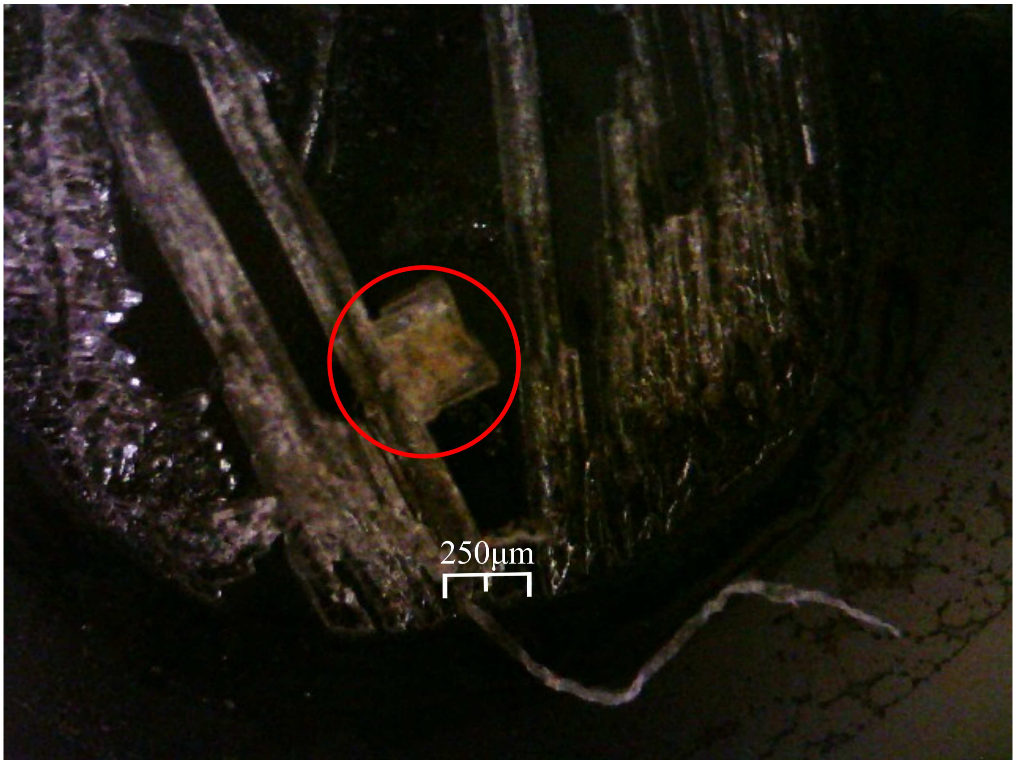

Figure 3.6: STMV crystal on silicon substrate. Crystallized $(NH_4)_2SO_4$ is also seen around the STMV crystal.

the silicon, to promote nucleation, and the process described above was again used to grow STMV crystals. Crystals grown on silicon were roughly the same size, at a few hundred micrometers across, as shown in Figure 5.1

3.2 Production of Ficoll Solutions

Solutions of Ficoll 70 and Ficoll 400 were prepared by dissolving Ficoll in D_2O using the methods described by Ranganathan *et al.* [2]. For both variations of Ficoll, all solutions were prepared under identical conditions, using the same process.

Before preparation of solutions, 1 mL of D_2O was weighed. This was used to give accurate calculations of the mass of Ficoll required to yield specific concentrations of

Figure 3.7: Vortex Genie from Scientific Industries. Used for initial mixing of solute and solvent.

Ficoll solution. Concentrations of solution were measured as percent of mass.

Preparation of Ficoll solutions began with measuring the desired mass of Ficoll in a small sealable vial. Once the desired mass was reached, 1 mL of D_2O was added to the vial. From here, a Scientific Industries Vortex Genie, shown in Figure 3.7, was used to vibrate the vial and promote dissolving of Ficoll. From here, a Fisherbrand Homogenizer 850, shown in Figure 3.8, with a rod diameter of 7mm and a speed of 11000 RPM was used to further mix the Ficoll with D_2O. The machine was run for three minutes, followed by a one minute break to allow the solution to settle. This process was repeated five times to ensure homogeneity of the solution. Finally, the vial was sealed with paraffin to ensure there would be no evaporation, and the solutions would remain at their desired concentration.

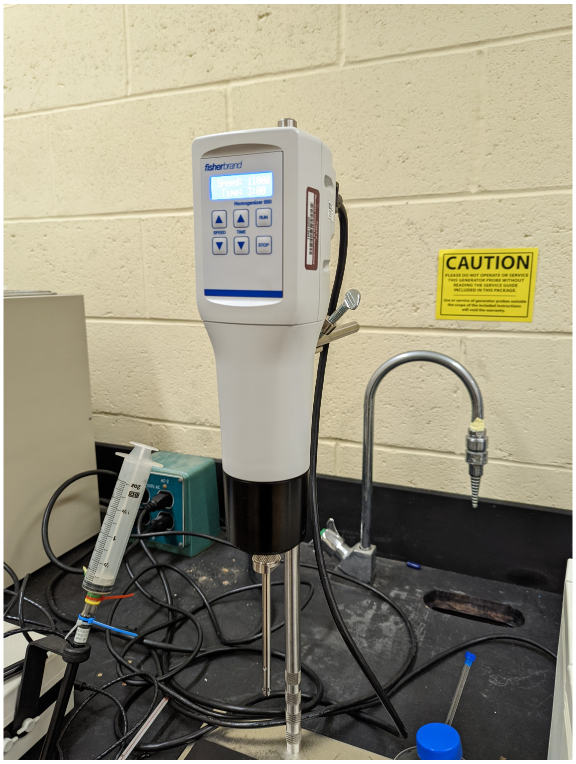

Figure 3.8: Fisherbrand Homogenizer 850. Used to homogenize macromolecular solutions.

3.3 Production of BSA Solutions

BSA solutions were prepared using nearly the same method as Ficoll solutions. Unlike Ficoll, BSA powder was dissolved in a buffer solution to ensure a stable pH environment BSA. A 0.1 mol/L solution of phosphate buffer with a pH level of 7.0 was prepared by diluting a 0.2 mol/L solution of phosphate buffer with deionized water. 1 mL of buffer solution was then weighed. This mass was subsequently used to calculate masses of BSA required to yield solutions with desired concentrations by mass percent.

Mass of BSA powder was measured in small, sealable vials. 1 mL of buffer solution was then added to the vial. A Scientific Industries Vortex Genie, shown in Figure 3.7 was used to vibrate the vial to promote dissolving of BSA. Next, a Fisherbrand Homogenizer 850, shown in Figure 3.8, with a rod diameter of 7mm and a speed of 11000 RPM was used to further dissolve the BSA in the buffer. The dissolving process was three minutes long, and repeated five times with a minimum of one minute between runs to allow the solution to settle. Once the homogenization process was finished, vials were sealed with paraffin to ensure there would be no evaporation of the solution, and the concentration would remain constant.

3.4 Brillouin Scattering

To collect Brillouin spectra of STMV, crystals were mounted into the Brillouin scattering apparatus shown in Figure 3.9. The light source of this setup is a monochromatic Nd:YVO_4 solid state laser with wavelength of 532 nm that operates with an output power of 2 W. To follow the schematic in Figure 3.9, light emitted from the laser immediately passes through a variable neutral density filter V_1 to reduce beam power.

The beam then passes through a half wave plate H, rotating the beam polarization by 90°, such that the beam now has a horizontal polarization. From here, the beam is split by a beam splitter B, where the reflected portion of the beam is sent to the Fabry-Perot interferometer as a reference beam. This reflected beam is focused onto mirror M_2 by aperture A, and is directed through variable neutral density filter V_3. This allows us to control the reference beam power as it enters the pinhole of the Fabry-Perot interferometer.

The portion of the beam which is transmitted through the beam splitter is reflected 90° by mirror M_1, then passes through filters F_1 and F_2, to further reduce beam power. The beam then passes through variable neutral density filter V_3. This filter allows us to manually control the beam power that is incident on the sample S, on the order of tens of milliwatts. Light is then reflected by the prism P, and focused onto the sample by the camera lens C. This camera lens is chosen due to its anti-reflective coating and built-in aperture.

Light scattered by the sample is then collected and collimated by the camera lens. The collimated beam is then focused on the pinhole of the interferometer by lens L.

Scattered light is analyzed by a six-pass tandem Fabry-Perot interferometer, manufactured by JRS Scientific Instruments, the schematic of which is shown in Figure 3.10. Light enters the interferometer through the pinhole, and is immediately redirected by mirrors M_1 and M_2 to the first hole of aperture A_1. This aperture has three holes, each of which are used between the three trips a beam of light makes. Light is then sent through the first Fabry-Perot etalon FP1. Only light with frequencies satisfying

$$f_m = m\frac{c}{2nl\cos\theta} \tag{3.1}$$

pass through, where m is an integer, n is the refractive index of the mirror in the

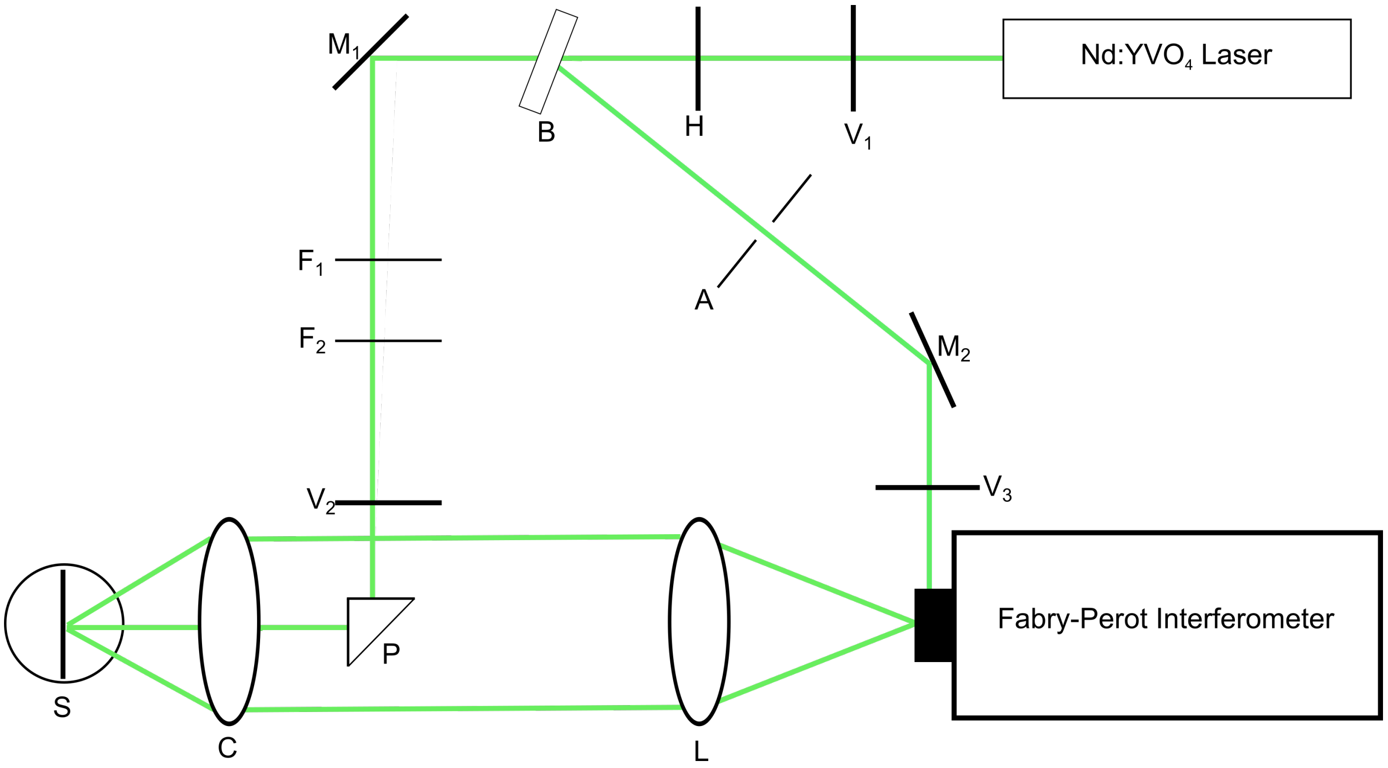

Figure 3.9: Brillouin spectroscopy setup to be used in experiments. V - variable neutral density filter, H - half wave plate, B - beam splitter, M - mirror, A - aperture, F - filter, P - prism, C - camera lens, S - sample, L - lens.

Fabry-Perot etalon, l is the spacing of the etalon, and θ is the angle of incidence. For studies on crystalline structures, angle of incidence is varied between spectra. For studies on liquids, all spectra are taken at normal incidence ($\theta = 0$). By varying l, we are able to scan over different frequencies. Light which emerges from the Fabry-Perot etalon then passes through the first hole in aperture A_2. The beam is then reflected by mirror M_3 into the second Fabry-Perot etalon FP2. As with the first etalon, only light which satisfies Equation 3.1 may pass through. As shown in Figure 3.10, both etalons have one mirror on the translation stage, and differ by an angle of α. As such, the mirror spacing of the second etalon is given by

$$d_2 = \frac{d_1}{\cos\alpha}. \tag{3.2}$$

The beam passes through the first hole in aperture A_3, and is then incident on prism P_1, which reflects the beam anti-parallel to its original path, through the second hole in A_3.

The beam redirected by the prism passes back through etalons FP2 and FP1, through the second holes in apertures A_2 and A_1. Lens L_1 then focuses the beam onto mirror M_4, which reflects the beam back. Lens L_1 then focuses the beam onto the third hole in A_1, where it makes its final pass through the Fabry-Perot etalons.

After its final passing through A_3 mirror M_5 directs the beam through aperture A_4, and onto lens L_2. This lens then focuses the beam onto the output pinhole of the Fabry-Perot interferometer, and onto the photomultiplier tube PM. The photomultiplier tube then generates an electronic signal, which is recorded in the spectra generated on the computer.

The benefit of using several passes through the tandem Fabry-Perot interferometer is that it drastically increases the contrast of the spectrum, yielding sharper peaks in

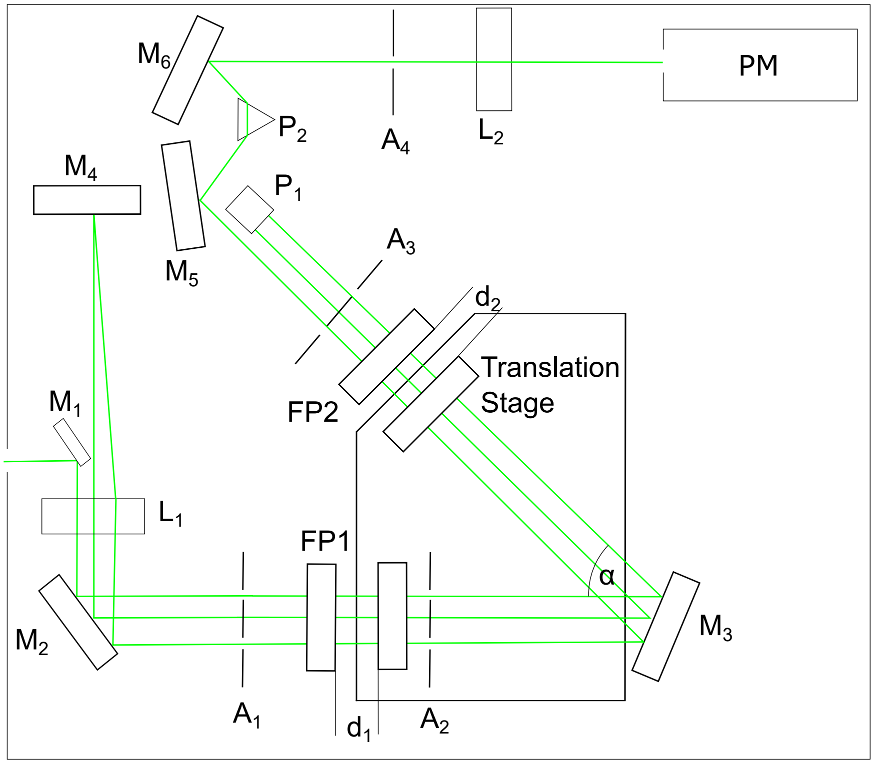

Figure 3.10: Optics of six pass tandem Fabry-Perot interferometer. M_i - mirror, L_i - lens, A_i - aperture, FP_i - Fabry-Perot interferometer, d_i - spacing of interferometer i, α - angle between FP_1 and FP_2, P - prism, PM - photomultiplier tube.

spectra corresponding to inelastic scattering events.

Brillouin spectra collected from aqueous solutions in this work were collected over ∼50000 scans, whereas spectra collected from crystals were collected over ∼300000 scans. This corresponds to ∼4 hours and ∼20 hours of collection time, respectively.

Bibliography

[1] R A Valverde and J A Dodds. *Journal of General Virology*, 68(4):965–972, 1987.

[2] Venketesh Thrithamara Ranganathan, Saman Bazmi, Stefan Wallin, Yun Liu, and Anand Yethiraj. Is ficoll a colloid or polymer? a multitechnique study of a prototypical excluded-volume macromolecular crowder. *Macromolecules*, 55(20):9103–9112, 2022.

Chapter 4

Concentration Dependence of Elastic and Viscoelastic Properties of Aqueous Solutions of Ficoll and Bovine Serum Albumin by Brillouin Light Scattering Spectroscopy

Abstract: The cellular environment is crowded with macromolecules of different shapes and sizes. The effect of this macromolecular crowding has been studied in a variety of synthetic crowding environments: two popular examples are the compact colloid-like Ficoll macromolecule, and the globular protein bovine serum albumin

(BSA). Recent studies have indicated a significant component of bound or surface-associated water in these crowders reduces the available free volume. In this work, Brillouin light scattering experiments were performed on aqueous solutions of Ficoll 70 and Ficoll 400 with concentrations ranging from 1 wt% to 35 wt% and BSA with concentrations of 1 wt% to 27 wt%. From the dependence of spectral peak parameters on polymer concentration, we determined fundamental solution properties: hypersound velocity, adiabatic bulk modulus and compressibility, apparent viscosity, and hypersound attenuation. Existing theory that ignores intermolecular interactions can only capture the observed linear trends in the frequency shift up to a threshold concentration, beyond which a quadratic term accounting for intermolecular interactions is necessary. This likely indicates a transition from the dilute to semi-dilute regime. In the Ficoll solutions (but not BSA) we see evidence for a central mode, which is indicative of relaxation in the hydration shell of Ficoll.

4.1 Introduction

Physical systems consisting of liquid water and macromolecules are ubiquitous. The fluid medium inside a biological cell is an aqueous solution that consists of macromolecules of different sizes and shapes which occupy a significant volume (typically assumed to be 30 - 40% of the cell) [1]. It has been understood for more than two decades that the crowded macromolecular environment can affect biochemical reactions within the cell [2]. Any volume other than the water volume is inaccessible to other molecules, and this excluded volume affects molecular structure, motions and chemical kinetics. In addition, for compact molecules with internal bound water, the accessible water volume will be less than the total water volume. Thus, the simplest picture of macromolecular crowding is entropic: the macromolecules and the inaccessible water reduce the free volume and increase the excluded volume.

While there is an increasing realization of the role of other non-specific interactions [3], experimental model systems have focused on aqueous solutions with a simple crowder such as a polysaccharide (*e.g.*, the compact Ficoll macromolecule or the chain-like dextran) or a globular protein (*e.g.*, bovine serum albumin) [4–6]. Structure and dynamics in these crowders has been reported extensively [7–11]. More realistic, heterogeneous crowding media, such as bacterial cell lysate, have been employed as well [12, 13]. In recent work, Ranganathan *et al.* [14] have provided quantitative evidence, via pulsed field gradient nuclear magnetic resonance spectroscopy, for water that is bound and thus inaccessible to other molecules, implying that the true excluded volume is larger than what is usually inferred.

Brillouin light scattering spectroscopy has been recognized as a niche technique for probing the mechanical and viscous properties in heterogeneous biomaterials [15]. Brillouin scattering experiments on aqueous macromolecular solutions and hydrogels typically report the dependence of spectral peak parameters and derived elastic and viscoelastic properties on solute concentration [16–18]. These parameters and properties are usually measured over a large concentration range and include Brillouin peak frequency shift and linewidth, hypersound velocity and attenuation, apparent viscosity, and various elastic and viscoelastic moduli. Attempts at using existing theoretical models to describe the concentration dependence of these quantities, however, have met with limited success. For example, Brillouin studies of so-called "aqueous biorelevant solutions" [16] reveal a common dependence of peak frequency shift on solute concentration for those solutions containing macromolecules (lysozyme, bovine serum albumin, and gelatin) up to 40 wt%, implying that this behaviour is largely independent of the nature of the solute. Application of the Reuss effective medium model for a two-component system resulted in an equation for the shift as a function of concentration that agreed well with most experimental data. A theoretical expression relating peak linewidth to concentration that incorporated this equation, however, was unable to fully reproduce the observed trends. Moreover, the sparsity and relatively large concentration interval ($\sim$ 10 wt%) between adjacent data points means that possible discontinuities in the observed trends, such as might occur in proximity to the polymer overlap concentration, were not accounted for in the model. In related Brillouin scattering work on collagen hydrogels [19] the storage modulus of collagen was extracted by fitting an expression for the concentration dependence of the effective storage modulus from the Voigt model to a high-hydration subset of the full experimental dataset for the concentration dependence of the gel storage modulus. It was stated that the two-component Voigt model gave a better fit than the Reuss model used in previous works [19]. No model was advanced to describe the data trend over the entire measured concentration range. Moreover, Brillouin scattering studies of cross-linked polyvinyl alcohol hydrogels [20] found only crude qualitative agreement between the observed dependence of Brillouin peak frequency shift and linewidth on gel network volume fraction and that calculated from a theory incorporating frictional damping and coupling between elastic waves in polymer network and fluid [21].

In this paper we report on Brillouin light scattering studies of aqueous solutions of polymers Ficoll 70, Ficoll 400, and Bovine Serum Albumin (BSA). Solution elastic and viscoelastic properties were determined over the dilute and semi-dilute ranges from the dependence of spectral peak parameters on solute (polymer) concentration. The observed trends in these properties are not consistent with existing theory but instead were found to be well-described by expressions derived from a new phenomenology relating hypersound frequency and solute concentration. The sensitivity of the Brillouin scattering technique to changes in structure and water-macromolecule dynamics also allowed the polymer overlap concentration to be determined. The extent of the hydration, manifested in the unexpectedly low overlap concentration, provides independent confirmation of recent results that suggest that the effective volume fraction occupied by hydrated macromolecules in solution is much larger than expected for the bare unhydrated variety. In characterizing the viscoelastic properties of commonly-used experimental model systems over a wide solute concentration range and advancing a phenomenology that incorporates interparticle interaction, this study provides important new insight into the physics of macromolecular crowding and biomacromolecular systems in general.

4.2 Experimental Details

4.2.1 Sample Preparation

Solutions of Ficoll-70 (m = 70 kDa) and Ficoll-400 (m = 400 kDa) were prepared under identical conditions by dissolving Ficoll powder in 99.9% pure D_2O at room temperature in small glass vials. A Scientific Industries Vortex Genie was used to promote initial mixing of D_2O and Ficoll, and subsequent homogenization was performed using a Fisherbrand Homogenizer 850 with a rod diameter of 7 mm and speed of 11,000 RPM. The homogenization sequence, which was performed five times per sample, consisted of three minutes of mixing followed by one minute of settling. The resulting solutions were clear and colourless and had concentrations ranging from 1 wt% to 35 wt%, with a noticeable increase in viscosity for those at the upper end of this range.

BSA ($m = 66.43$ kDa) solutions with concentrations of 1% w/w to 27% w/w were prepared by dissolving BSA powder in 0.1 M phosphate buffer solution with pH of 7.0

at room temperature and subjecting them to the same mixing and homogenization procedure as used for the Ficoll solutions. Solutions with concentrations < 20 % w/w were clear and colourless while those with concentrations higher than this value were somewhat cloudy.

4.2.2 Brillouin Light Scattering Spectroscopy

Apparatus

Brillouin light scattering experiments were performed under ambient conditions using a 180° backscattering geometry. The incident light source was a Nd:YVO_4 solid state laser (Coherent Verdi V-2) with an emission wavelength of 532 nm and output power of 1.66 W. Neutral density filters placed in the beam path were used to reduce the power level at the sample to ~ 100 mW. Light was focused on samples with a 5 cm lens of f-number 2.8 (NA = 0.18). Scattered light was collected and collimated by the same lens and subsequently focused by a 40 cm focal length lens onto the 450 μm entrance pinhole of a six-pass tandem Fabry-Perot interferometer (JRS Scientific Instruments) for spectral analysis. The interferometer had a free spectral range of 15 GHz and a finesse of ~ 100. A schematic of this experimental setup can be found in Refs. [22, 23].

Quantities Derived from Spectra

Elastic and viscoelastic properties of the Ficoll solutions were deduced from Brillouin spectra. Hypersound velocity was determined using the well-known Brillouin equation applied to the case of a backscattering geometry,

$$v = \frac{f\lambda}{2n}, \tag{4.1}$$

where f is the measured Brillouin peak frequency shift, λ is the incident light wavelength, $n = n(x)$ is the concentration-dependent solution refractive index, and x is the concentration in weight percent. The latter was obtained for each Ficoll 70 and Ficoll 400 solution using $\partial n/\partial C = 0.148$ mL/g (with C expressed as g/mL) relationships provided by Fissel *et al* [24]. Similarly, refractive indices for BSA solutions were calculated using the relationship $\partial n/\partial C = 0.190$ mL/g (with C expressed as g/mL), found by Tumolo *et al.* [25].

Knowledge of the hypersound velocity allowed the adiabatic bulk modulus to be found from

$$B = \rho v^2, \tag{4.2}$$

where ρ is the mass density of the solution. The density of the solution showed little variation over the full concentration range, and was approximated to a constant 1110 kg/m^3 for the purposes of fitting. The adiabatic compressibility, κ, was also determined using the fact that $\kappa = 1/B$.

The apparent viscosity, η, and hypersound attenuation, α, in the solution were deduced from Brillouin spectral data via

$$\eta = \frac{4}{3}\eta_s + \eta_b = \frac{\rho v^2 \Gamma_B}{4\pi^2 f^2} = \frac{\rho \lambda^2 \Gamma_B}{16\pi^2 n^2} \tag{4.3}$$

and

$$\alpha = \frac{\pi \Gamma_B}{v}, \tag{4.4}$$

respectively [26], where Γ_B is the Brillouin peak full width at half-maximum (FWHM), η_s and η_b are the shear and bulk viscosities, and the other quantities are as already defined.

4.3 Results and Discussion

4.3.1 Spectra

General Features and Mode Assignment

Figure 4.1 shows a series of Brillouin spectra collected from the Ficoll 70 solutions and BSA solutions. Spectra of the Ficoll 400 solutions are similar to Ficoll 70 spectra in all respects (see Figure A1 in the Appendix A). A single set of Brillouin peaks was observed in all spectra, with a frequency shift ranging from $\sim$ 6.8 GHz to $\sim$ 8.4 GHz. Although not obvious from the spectra shown in Figure 4.1, there is also a broad, weak peak at the center of the spectra obtained from Ficoll 70 and Ficoll 400 solutions with solute concentrations $\geq$ 20%. The presence of this peak was inferred from the fact that the baseline intensity in the region between the central elastic peak and the Brillouin doublet in spectra of high concentration solutions was noticeably higher than that in spectra of the low concentration solutions and also higher than that on the high frequency shift side of the Brillouin doublet. An example of this for Ficoll 70 solutions with 3% and 30% concentration is shown in Figure 4.2 A. In contrast, no central peak was discernible in spectra of the BSA solutions.

The Brillouin doublet and the peak in the center of the spectra of high concentration Ficoll solutions have different origins. The former is assigned to the usual longitudinal acoustic mode propagating through the solution based on the similarity of its frequency shift to that of the corresponding mode in water [27]. The central peak was attributed to a diffusive relaxation mode based on its zero frequency shift and the fact that the width of the peak showed no significant change with changing concentration [28]. These properties are consistent with other Brillouin and Rayleigh scattering studies which have observed this relaxation mode in macromolecular solutions. [17, 18, 29, 30]

Extraction of Peak Parameters

Longitudinal acoustic mode peak frequency shift and linewidth were obtained by fitting Lorentzian functions to the Brillouin peaks, with the latter being processed prior to plotting by subtraction of the 0.3 GHz instrumental contribution to the best-fit linewidth.

To obtain an estimate of the central mode linewidth, Γ_C, it was first necessary to remove data from regions of the spectrum containing other peaks so as to minimize its impact on any subsequent fit. This included the region containing the central elastic peak and other data contained within the central Fabry-Perot interferometer control window, ± 2 GHz from the center of the spectrum, and that containing the two longitudinal mode peaks, which was typically a ~ 6 GHz range around the longitudinal peak. The remaining data was fitted to a Lorentzian function (see Fig. 4.2A), revealing a central mode that is very weak and exceptionally wide, with a FWHM of ~ 14 GHz. As can be seen by the high degree of overlap between the experimental data and the dotted curve in Fig. 4.2A, the addition of this Lorentzian to the best-fit Lorentzians for the longitudinal mode peaks results in a function that well represents the original Brillouin spectrum (without the central elastic peak).

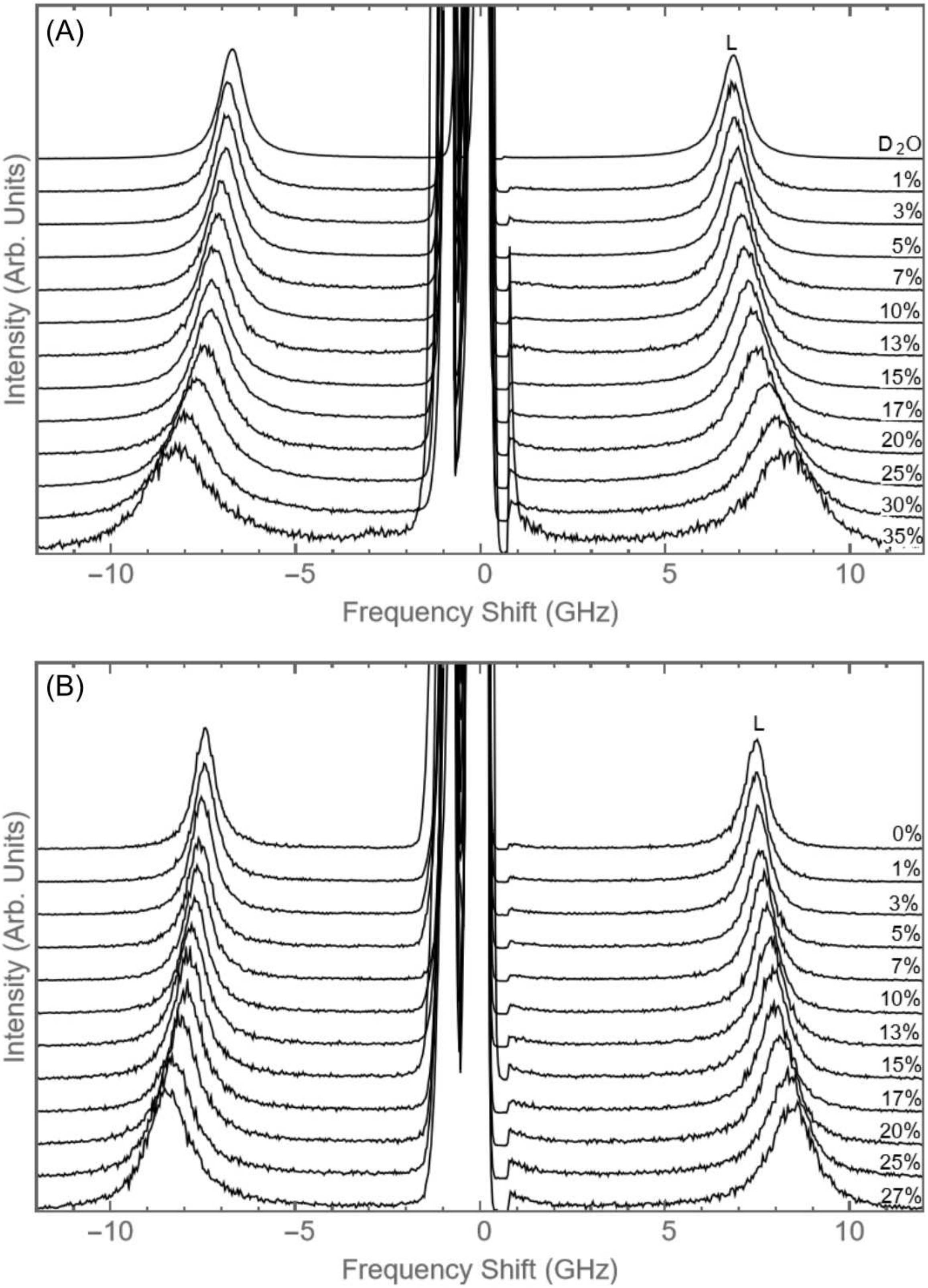

Figure 4.1: Normalized Brillouin spectra collected from solutions of (A) Ficoll 70 and (B) BSA of various concentrations (wt%). L represents a longitudinal bulk mode.

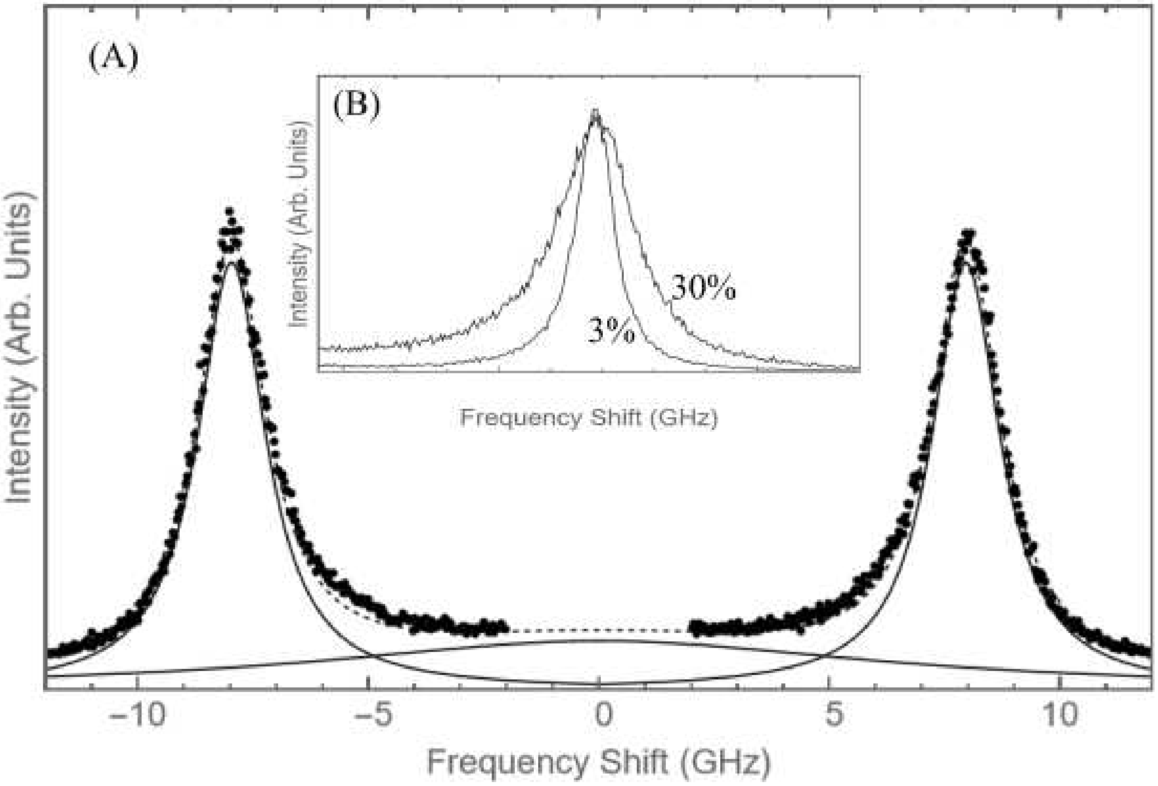

Figure 4.2: (A) Brillouin spectrum of an aqueous solution of Ficoll 70 with a solute concentration of 30%. Solid lines - Best-fit Lorentzian functions for central peak and Brillouin peaks. Dotted line - sum of central peak and Brillouin peak best-fit Lorentzians. (B) Anti-Stokes Brillouin peaks for aqueous Ficoll solutions with solute concentrations of 3% and 30%. 30% concentration peak is shifted horizontally from 7.96 GHz to 6.86 GHz so that the peaks overlap to highlight the slight asymmetry and significantly higher baseline intensity of the peak for the 30% concentration solution compared to that for the 3% solution on the low frequency shift side.

4.3.2 Longitudinal Acoustic Mode: Elastic and Viscoelastic Properties

Dependence of Brillouin Peak Parameters on Solute Concentration

Figure 4.4 shows longitudinal acoustic mode peak frequency shift and linewidth versus concentration for the Ficoll 70, Ficoll 400, and BSA solutions. For all solutions, both quantities increase monotonically with increasing concentration, with the linewidth being much more sensitive than the shift to changes in concentration. While the frequency shift for each solution increases by $\sim 20\%$ over the range probed, the peak FWHM for the Ficoll and BSA solutions increases by a factor of ~ 4 and ~ 2, respectively.

For a given concentration, the frequency shift for Ficoll 400 solution is slightly larger than that for Ficoll 70 solution. At low concentrations, the peak linewidths obtained from the Ficoll 70 and Ficoll 400 solutions are nearly equal, while for concentrations in excess of ~ 15 wt% the linewidths begin to diverge, with that for Ficoll 400 being greater than that for Ficoll 70 over this range. This subtle change in the relationship between concentration and frequency or linewidth may represent the overlap concentration at which the system physics changes as it transitions from the dilute to the semi-dilute regime.

The solute concentration dependence of Brillouin peak frequency shift of some so-called biorelevant aqueous solutions have been well-fit for concentrations up to $x \sim 40$ wt% by the relation [16]

$$f_R(x) = \frac{f_w}{\sqrt{1 - x + x v_w^2/v_s^2}} = \frac{f_w}{\sqrt{1 + \alpha x}}, \tag{4.5}$$

where $\alpha := v_w^2/v_s^2 - 1$. Also, the concentration dependence of linewidth has been well fit up to $x \sim 20$ wt% by

$$\Gamma_R^B(x) = Af_R(x)^2 + Bx, \tag{4.6}$$

respectively, where A and B are constants and f_w, v_w, and v_s are the Brillouin peak frequency shift for water, and the hypersound velocities of water and the solute, respectively. The basis of Equation 4.5 is the two-component Reuss model for which the effective elastic modulus M of the solution is given by

$$\frac{1}{M} = \frac{\rho\mu_s}{\rho_s}\left[\frac{1}{M_s} - \frac{1}{M_w}\right] + \frac{1}{M_w}, \tag{4.7}$$

where $\mu_s = m_s/(m_s + m_w)$ is the solute mass fraction and M_s and M_w are the elastic moduli of the solute and water, respectively. If the density of the solution ρ equals that of the solute ρ_s, then Equation 4.7 simplifies to

$$\frac{1}{M} = \frac{\mu_s}{M_s} + \frac{1-\mu_s}{M_w}, \tag{4.8}$$

Equation 4.5 can be obtained from Equations 4.1 and 4.8 with the approximation of fixed density and refractive index.

Fitting Equation 4.5 to the $\{f, x\}$ data for the Ficoll and BSA solutions with v_w^2/v_s^2 as an adjustable parameter, however, yielded best-fit relations $f(x)$ that show tolerable agreement with experiment, particularly in the Ficoll data, shown in Figure 4.3. While this fit looks tolerable at the macro level, when focusing on the low concentration data of Ficoll, shown in the inset of Figure 4.3, the fit is of poorer quality. This is significant because this region is where the fit is expected to be the strongest, as this is where the volume fraction and mass fraction are close to equal. Equation 4.5 in the original work [16] described the relationship between Brillouin peak frequency and the volume (not

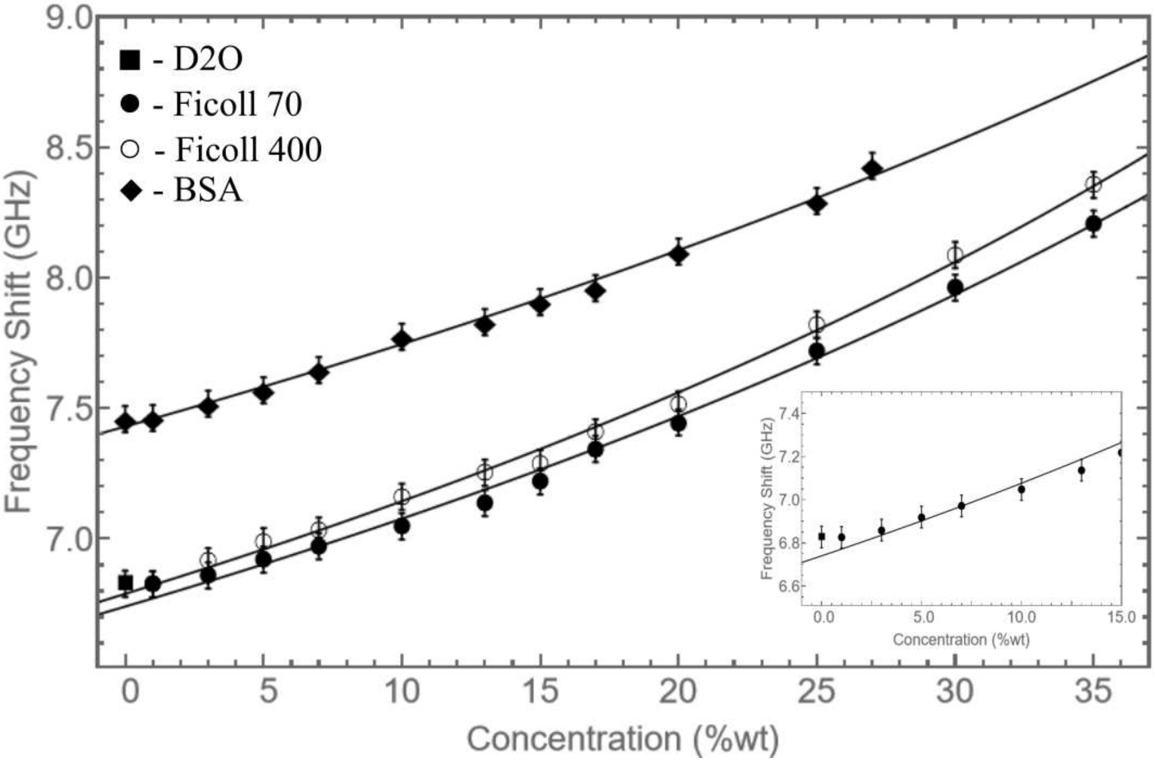

Figure 4.3: Brillouin peak frequency shift as a function of concentration for aqueous solutions of Ficoll 70, Ficoll 400, and BSA. Solid lines represent fits of $f(x)$ to Equation 4.5.

mass) fraction. Substitution of these "best-fit" expressions for $f(x)$ into Equation 4.6 give similar quality fits to the $\{\Gamma_B, x\}$ data shown in Figure 4.4. In addition, a fit of Equation 4.5 to only the low concentration data yields an excellent fit for $x \leq 10\%$ but the resulting function does not describe the higher concentration data. This sub-optimal agreement between theory and experiment is likely due to it not properly accounting for molecular crowding arising from hydration of Ficoll or BSA as the solution concentration increases, the onset of which occurs at the transition from the dilute to semi-dilute regime. The larger difference between experimental data and the fit of Equation 4.5 for Ficoll 70 and Ficoll 400, compared to that of BSA, is also indicative of a higher degree of hydration of these polymers, which will be further discussed later. It is important to note that there is a natural crowding effect that occurs with increased concentration, however this effect is amplified by the swelling of polymers due to hydration. This crowding leads to increased polymer-polymer interaction in the solution. As such, the hypersound frequency can no longer be described by Equation 4.5; there are also contributions from volumetric and entropic changes due to polymer-polymer interactions, specifically the onset of contact and the possible formation of loosely packed regions of solute molecules.

The failure of the above model to accurately reproduce the concentration dependence of f and Γ_B for the Ficoll and BSA solutions, coupled with the lack of other appropriate theoretical models, lead us to propose a new phenomenology to describe the current experimental data. This phenomenology assumes that the concentration dependence of f and Γ_B both increase smoothly with concentration according to

$$f(x) = f_R(x) + A_1 x^2, \tag{4.9}$$

where f_R is given by Equation 4.5, and

$$\Gamma_B(x) = Af(x)^2 + Bx + A_2x^2, \tag{4.10}$$

where the A_i are fit parameters and $f(x)$ is given by Equation 4.9. Furthermore, the second order term in Equation 4.10, A_2x^2 is a phenomenological extension to van't Hoff's law, as explained below [31, 32]. From this, solute molecules in a dilute solution may be treated as an ideal gas. As such, the linewidth is proportional to solution density, as expressed in the equation

$$\Gamma_B(x) \propto 1 + c_1\rho + c_2\rho^2 + c_3\rho^3 + \cdots . \tag{4.11}$$

At low concentrations, corresponding to lower density, the higher order terms are insignificant. At higher concentrations, however, these higher order terms begin to dominate [32]. The second order term of the virial equation is attributed to interactions between solute molecules, the contribution of which becomes more important at higher solute concentrations.

Figure 4.4 shows best-fits of Equations 4.9 and 4.10 to the $\{f, x\}$ and $\{\Gamma_B, x\}$ data for the Ficoll and BSA solutions. The fits reproduce the trends of the experimental data very well. For reference, the best-fit equations are given in Table 4.2.

Although not obvious, there is also what could be a localized characteristic concentration which is visible in both the frequency shift and linewidth, which is localized around $\sim$ 15 wt% concentration for both Ficoll solutions (denoted by the arrow in the inset in Figure 4.4 for change in behaviour of Ficoll 70 peak width). The characteristic concentration around $\sim$15% solute concentration is also observed in the BSA data.

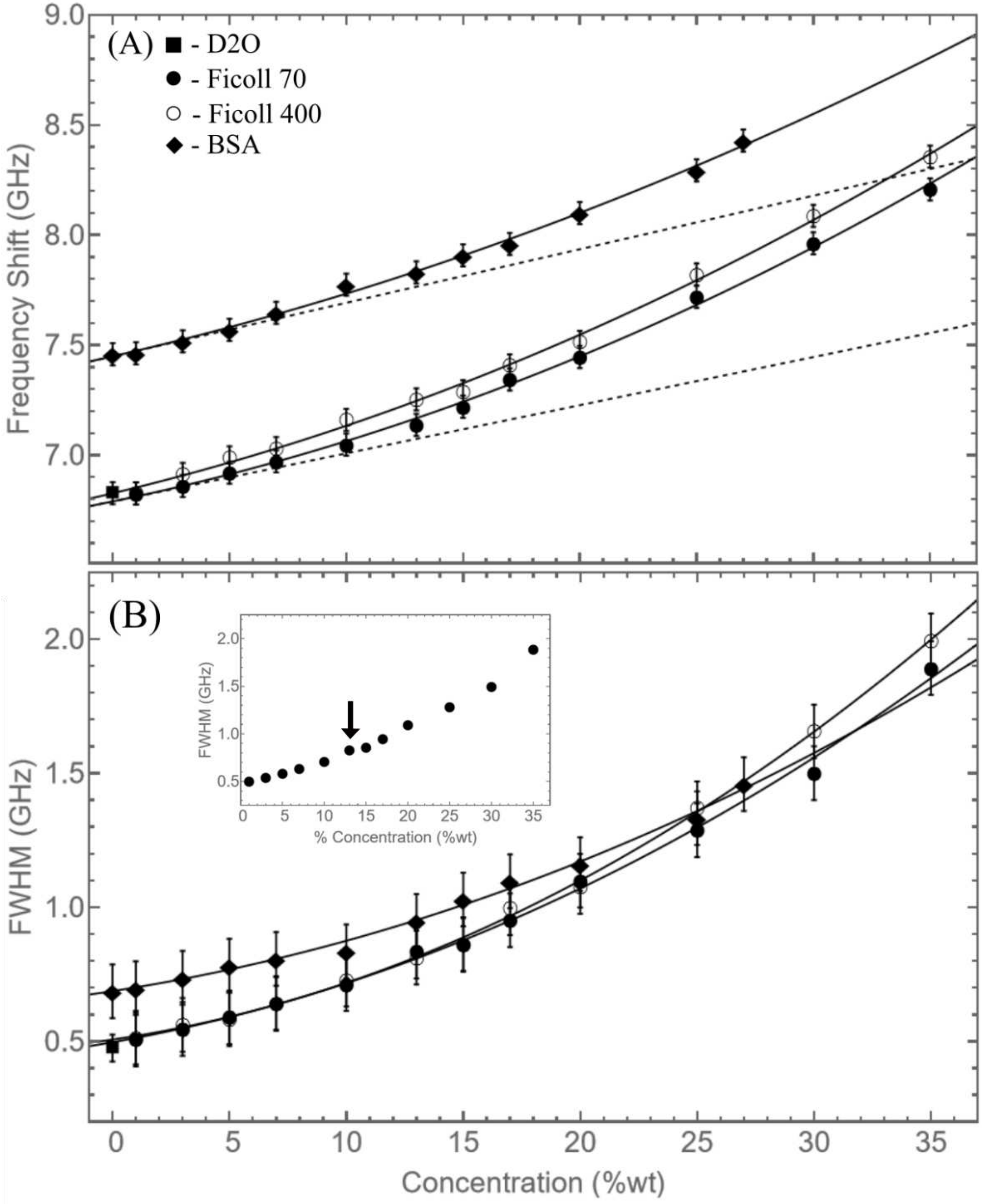

Figure 4.4: Brillouin peak frequency shift (A) and linewidth (B) as a function of concentration for aqueous solutions of Ficoll 70, Ficoll 400, and BSA. Solid lines represent best fits of $f(x) = f_R(x) + A_1x^2$ and $\Gamma_B(x) = Af(x)^2 + Bx + A_2x^2$. Dashed lines represent frequency relationship provided by Equation 4.5 for Ficoll 70 and BSA. Inset in (B) is linewidth of Ficoll 70.

Although the origin of this phenomenon is unclear from the plotted data, these characteristic concentrations are concurrent with the overlap concentration, and, therefore, may be indicative of the overlap concentration, and the transition from the dilute to semi-dilute regime. This transition point is highlighted in Table 4.3.2.

Hypersound Velocity

Figure 4.5 (A) shows the evolution of hypersound velocity with concentration for the Ficoll 70, Ficoll 400, and BSA solutions. There is a consistent increase in velocity with increasing solute concentration for all solutions, as expected from the increase in Brillouin peak frequency shift with increasing concentration. As with the frequency data, the hypersound velocity in Ficoll 400 solutions is systematically higher than in Ficoll 70 solutions. Furthermore, while the velocity of BSA solutions being larger than that of Ficoll solutions can be attributed to the different solvent, the change in velocity with respect to concentration was much lower for BSA than for both Ficoll solutions. Figure 4.5 (A) shows curves for velocity as a function of concentration which were derived by substituting the best-fit equation for frequency as a function of concentration into Equation 4.1.

In the dilute regime, the hypersound velocity of macromolecular solutions can be expressed in a manner similar to Equation 4.5, as hypersound velocity is linearly proportional to phonon frequency [16]. However, as the concentration increases beyond 10%, we begin to see a significant increase in packing of solute molecules in solution due to crowding effects. This is demonstrated by the deviation of Brillouin peak frequency and linewidth from previous theory. It also is important to note that previous studies have shown that solute hydration leads to volume fraction of solute being much larger than expected than expected for bare (no bound water) solute

Table 4.1: Hypersound velocities for Ficoll 70, Ficoll 400, and Bovine Serum Albumin (BSA) solute, calculated using the equation ${v_w}^2/{v_s}^2 - 1 = \alpha$, where α is the fit parameter in the denominator of $f_R(x)$ from equation 4.5.

Solute	Velocity (m/s)
Ficoll 70	2320
Ficoll 400	2850
BSA	2580

molecules at similar weight concentrations.[14]. This concept is further supported by Brillouin scattering results in this work, as the onset of polymer-polymer interactions was seen at concentrations as low as 10% by weight. This increase in macromolecular packing leads to an increase in interactions between solute molecules [33]. This is the transition between the dilute and the semi-dilute limits.

By using the $f_R(x)$ expression of Equation 4.9, the hypersound velocity for Ficoll 70, Ficoll 400, and BSA was calculated. Values for these velocities are shown in Table 4.1. Velocities calculated for solutes used in this work ranged between ~ 2300 m/s and ~ 2900 m/s, which is comparable to results from previous studies on macromolecular solutions [16].

Bulk Modulus & Adiabatic Compressibility

Figure 4.5 (B) shows that the bulk modulus for the Ficoll 70, Ficoll 400, and BSA solutions increase with increasing solute concentration. This trend was expected not only from the relationship between bulk modulus and hypersound velocity given by Equation 4.2, but also from an intuitive perspective as with an increase in concentration a greater proportion of the available volume is occupied by the solute. This leads to the solution being less compressible and therefore to a higher bulk modulus. For low concentrations B increases approximately linearly with x as predicted

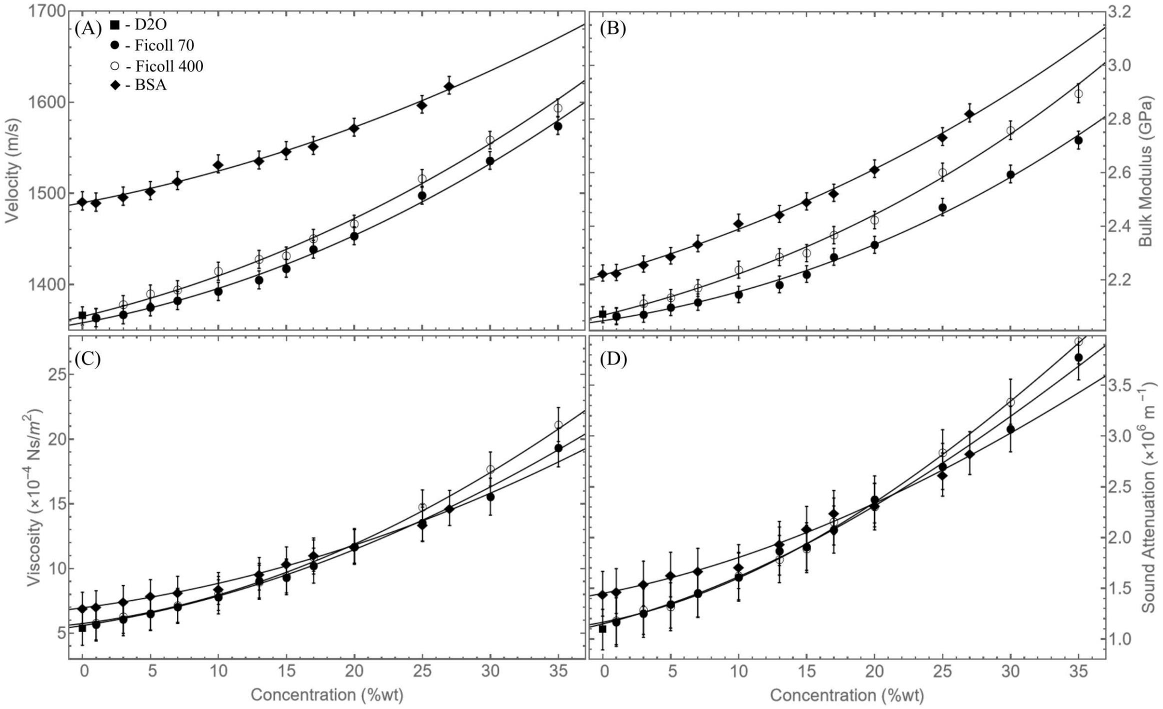

Figure 4.5: Hypersound velocity (A), solution bulk modulus (B), apparent viscosity (C), and hypersound attenuation (D) as a function of concentration in aqueous solutions of Ficoll 70, Ficoll 400, and BSA. Solid lines are curves are based on the frequency fits from Figure 4.4 and Equations 4.1, 4.2, 4.3, and 4.4, respectively

by Equation 4.7 in the limit of small x. While there is no obvious change in trend, at $x \sim 15$ wt% the slope of $B(x)$ is noticeably larger and continues to increase with increasing concentration. Following the reasoning in Sec. 4.3.2(1), this is caused by the solution transitioning from dilute to semi-dilute. The increased interaction between solute molecules (*e.g.*, entanglement) results in a decrease in compressibility and, consequently, an increase in bulk modulus. This deviation of the solution compressibility from a volumetric average of the compressibilities of the constituents (*i.e.*, the Reuss model) can be attributed to entropic and volume contributions due to these interactions as discussed in Sec. 4.3.2(1) [33].

Apparent Viscosity

The apparent viscosity of the Ficoll and BSA solutions for a range of concentrations in the dilute and semi-dilute regimes are shown in Figure 4.5 (C). The $\eta(x)$ curves in this figure were obtained from Equation 4.3 using $\Gamma_B(x)$ and $f(x)$ described above. As can be seen, the apparent viscosity values for the two Ficoll solutions are roughly equal at low concentrations but begin to diverge from eachother at $x \sim 15$ wt%, behaviour similar to that observed for relative viscosity in rheology studies of aqueous Ficoll 70 and Ficoll 400 solutions [14]. It is important to note that the values measured in this work are different from viscosity measurements from rheology measurements [14]. This is due to the relationship expressed in Equation 4.3, where we can see that the apparent viscosity is ~3 times larger than the shear viscosity, as the bulk viscosity of water is ~ 2 times larger than the shear viscosity. This change in behaviour is approximately at a concentration corresponding to the dilute-to-semi-dilute transition. Within this region, the contribution to viscosity from Ficoll becomes more dominant than that of D_2O. It is important to note that previous rheology studies have shown that the intrinsic viscosities of Ficoll 70 and Ficoll 400 differ by $\sim 12\%$ [14]. Furthermore, the range of apparent viscoties presented in this work are significantly different from the ranges of shear viscosities shown in previous rheology studies. While the very low concentration viscosities are comparable, the shear viscosities presented in previous rheology work are larger than the apparent viscosities derived from Brillouin scattering by a factor of ~ 100 [14]. At low concentrations, apparent viscosity of BSA solutions is slightly larger than that of either solution of Ficoll. The curve of Equation 4.3 for BSA, however, is considerably less steep than that of either solution of Ficoll, demonstrating a lower intrinsic viscosity for BSA.

Hypersound Attenuation

Figure 4.5 (D) shows hypersound attenuation for all solutions at various solute concentrations determined from Equation 4.4. The curves that appear in this figure were obtained in a manner analogous to those for apparent viscosity. The attenuation increases monotonically with increasing concentration for all solutions. As was the case for apparent viscosity, hypersound attenuation in the Ficoll 70 solution is approximately equal to that in the Ficoll 400 solution at low concentrations. As concentration increases, the solutions transition from the dilute to the semi-dilute and the attenuation values for the two solutions diverge. This is an indication that hypersound attenuation is much more strongly correlated with D_2O than with Ficoll in the dilute limit. In the semi-dilute limit, the dependence on Ficoll concentration becomes more important. Furthermore, similar to viscosity, at low concentrations, where attenuation is more closely related to the solvent, attenuation of BSA solutions is greater than that of either Ficoll solution. Once again, however, the concentration dependence of BSA solutions with concentration is less sharp than that of Ficoll.

Table 4.2: Empirical equations describing the concentration dependence of the elastic and viscoelastic properties of aqueous solutions of Ficoll 70, Ficoll 400, and Bovine Serum Albumin (BSA).

Quantity	Base Equation	Solution	Solution-Specific Equation
Hypersound Frequency (GHz)	$f(x) = f_R(x) + A_1x^2$	Ficoll 70-D_2O	$f(x) = (6.80/\sqrt{1 - 0.00653x}) + 0.000412x^2$
		Ficoll 400-D_2O	$f(x) = (6.82/\sqrt{1 - 0.00771x}) + 0.000314x^2$
		BSA	$f(x) = (7.45/\sqrt{1 - 0.00665x}) + 0.000253x^2$
Brillouin Linewidth (GHz)	$\Gamma_B(x) = Af(x)^2 + Bx + A_2x^2$	Ficoll 70-D_2O	$\Gamma_B(x) = 0.0123x + 0.000566x^2 + 0.0108f(x)^2$
		Ficoll 400-D_2O	$\Gamma_B(x) = 0.00899x + 0.000753x^2 + 0.0108f(x)^2$
		BSA	$\Gamma_B(x) = 0.00896x + 0.000446x^2 + 0.0124f(x)^2$

Table 4.3: Estimated overlap concentration for aqueous solutions of Ficoll 70, Ficoll 400, and Bovine Serum Albumin (BSA) obtained in present work and previous studies. PW-C: Present Work - Overlap concentration estimated from visible change in behaviour observed in plot of Frequency shift vs. Solute Concentration and/or FWHM vs. Solute Concentration. PW-Q: Present Work - Overlap concentration estimated from the divergence of previous model resulting from removing quadratic term from Eq. 4.9.

Solution	Overlap Concentration (wt. %)				
	PW-C	PW-Q	Ref [14]	Ref [34]	Ref [35]
Ficoll 70	$\sim 15 \pm 3$	$\sim 10 \pm 5$	10-15	-	22.9
Ficoll 400	$\sim 17 \pm 3$	$\sim 20 \pm 5$	10-15	5.33	13.5
BSA	$\sim 13 \pm 3$	$\sim 10 \pm 5$	-	-	-

4.3.3 Central Mode

Figure 4.2 shows the central peak present in spectra of high concentration Ficoll solutions. Such peaks were not observed in BSA spectra. This peak was observed in the spectra of solutions with $x \geq 20\%$, from which it was noted that its intensity increases with increasing concentration for both Ficoll 70 and Ficoll 400 solutions. The width of this central peak, however, shows no systematic change with change in concentration. This central peak was attributed to a relaxation mode due to D_2O molecules within the hydration shells of Ficoll, a phenomenon which has been observed in Brillouin and Rayleigh scattering experiments on other high concentration macromolecular solutions [17, 18, 29, 36]. This phenomenon occurs when D_2O molecules briefly bind to the hydration shell of the Ficoll molecules before returning to the bulk solvent.

Central modes of Brillouin spectra of liquids, referred to as Mountain modes, have been studied for over fifty years, and were originally describes as arising from coupling of the internal molecular degrees of freedom with the thermal fluctuations of the solvent [37]. These properties could be enhanced by the hydration of macromolecules within the solvent. Ficoll, therefore, may be a strong candidate for systematic study of Mountain modes.

4.3.4 System Properties and Dynamics

Table 4.2 contains a summary of the dependence of hypersound frequency and Brillouin peak linewidth on concentration given by Equations 4.4 and 4.10. All elastic and viscoelastic properties explored in the present study increase monotonically with increasing solute concentration. These increases can be attributed to an increase in packing of solute molecules within the solution. For aqueous solutions of Ficoll or BSA, there are two components which impact the volume fraction. The first is the natural addition of solute molecules to solution as concentration increases. The second component to consider is the hydration of solute molecules. This process is seen to primarily occur in higher concentration solutions, but makes a large contribution to the volume fractions of Ficoll 70 and Ficoll 400. A change in volume fraction due to hydration also occurs in BSA, but to a lesser degree than in Ficoll. As such, there is a much more dramatic increase in volume fraction of these macromolecules compared to solutions where there is no hydration of solute molecules. Because of this, Ficoll solutions used in this study range from dilute solutions to nearly maximum packing of randomly distributed spheres, and BSA solutions also experience a very high degree of packing at the highest concentrations. From the Brillouin scattering results, it is apparent that BSA experiences less packing compared to Ficoll. Table 4.2

shows fit equations for frequency versus solute concentration. The second order term for BSA, corresponding to polymer-polymer interactions, is ∼20% lower than that of either type of Ficoll. This increase in volume occupied by globular molecules results in a reduction in solution compressibility and a corresponding increase in bulk modulus. Furthermore, the increase in solute volume fraction makes the aqueous solution more viscous and the packing of spheres increases the attenuation of sound within the solution.

To further discuss the effects of hydration, above 15% concentration a relaxation mode was observed in Brillouin spectra for both Ficoll 70 and Ficoll 400 solutions. This relaxation was caused by hydration of Ficoll, specifically due to an exchange of D_2O between the bulk solvent and the hydration shell of Ficoll. This addition of relaxation due to hydration further validates the larger solute volume fraction due to hydration, compared to bare solute at similar mass concentrations, by demonstrating a fundamental change in the mechanics of the solution as concentration surpasses the overlap concentration.

4.4 Conclusion

In the present study Brillouin light scattering experiments were performed on solutions of Ficoll 70 and Ficoll 400 dissolved in D_2O with concentrations ranging from 1% to 35 wt%, and BSA dissolved in phosphate buffer with concentrations ranging from 0% to 27%. Brillouin spectra for all such solutions exhibited a single Brillouin peak which was attributed to a longitudinal bulk mode. The frequency shifts and linewidths of these Brillouin peaks were used to calculate hypersound velocity, attenuation, and bulk modulus, all of which exhibited an increase with increasing concentration. For the solutions studied in this work, the relationship between hypersound frequency and solute concentration cannot accurately be described by models which have been previously presented for non-interacting macromolecular solutions. A new phenomenology was derived to describe the change in hypersound frequency in macromolecular solutions which incorporates solute-solute interactions.

Finally, a central peak was observed in high concentration spectra for both Ficoll 70 and 400 but was not observed in BSA spectra. This peak was attributed to relaxation associated with hydration of Ficoll by D_2O.

This work provides physical insight into the interaction of macromolecules and water in crowded macromolecular environments, which are of immense importance in biological systems. Further, it provides quantitative spectroscopic signatures for bound or surface-associated water. Concentration dependence, with complementary work on temperature dependence, of aqueous biomacromolecular solutions is important because of the wide range of solution concentrations found in naturally occurring biological systems. This work also further establishes Brillouin spectroscopy as a valuable probe of the elasticity and viscoelasticity of aqueous biomacromolecular systems.

4.5 Acknowledgments

AY and GTA acknowledge the support of the Natural Sciences and Engineering Research Council of Canada (RGPIN-2019-04970 and RGPIN-2015-04306, respectively).

Bibliography

[1] R J Ellis. Macromolecular crowding: obvious but underappreciated. *Trends in Biochemical Sciences*, 26(10):597–604, 2001.

[2] A. P. Minton. The influence of macromolecular crowding and macromolecular confinement on biochemical reactions in physiological media. *Journal of Biological Chemistry*, 276:10577, 2001.

[3] G Rivas and A Minton. Influence of nonspecific interactions on protein associations: Implications for biochemistry in vivo. *Annual Review of Biochemistry*, 91:321–351, 2022.

[4] A Dhar, A Samiotakis, S Ebbinghaus, L Nienhaus, D Homouz, M Gruebele, and M S Cheung. Structure, function, and folding of phosphoglycerate kinase are strongly perturbed by macromolecular crowding. *Proceedings of the National Academy of Sciences*, 107(41):17586–17591, 2010.

[5] L C Acosta, G M Perez Goncalves, G J Pielak, and A H Gorensek-Benitez. Large cosolutes, small cosolutes, and dihydrofolate reductase activity. *Protein Science*, 26(12):2417–2425, 2017.

[6] M G S Norris and N Malys. What is the true enzyme kinetics in the biological system? an investigation of macromolecular crowding effect upon enzyme kinetics of glucose-6-phosphate dehydrogenase. *Biochemical and Biophysical Research Communications*, 405(3):388–392, 2011.

[7] D. Venturoli and B. Rippe. Ficoll and dextran vs. globular proteins as probes for testing glomerular permselectivity: effects of molecular size, shape, charge, and

deformability. *American Journal of Physiology-Renal Physiology*, 288(4):F605–F613, 2005.

[8] W H Fissell, S Manley, A Dubnisheva, J Glass, J Magistrelli, A N Eldridge, A J Fleischman, A L Zydney, and S Roy. Ficoll is not a rigid sphere. *American Journal of Physiology-Renal Physiology*, 293(4):F1209–F1213, 2007.

[9] A A Fodeke and A P Minton. Quantitative characterization of polymer- polymer, protein- protein, and polymer- protein interaction via tracer sedimentation equilibrium. *The Journal of Physical Chemistry B*, 114(33):10876–10880, 2010.

[10] A Christiansen and P Wittung-Stafshede. Quantification of excluded volume effects on the folding landscape of pseudomonas aeruginosa apoazurin in vitro. *Biophysical Journal*, 105(7):1689–1699, 2013.

[11] G Shah and P L Dubin. Adsorptive interaction of ficoll standards with porous glass size-exclusion chromatography columns. *Journal of Chromatography A*, 693(2):197–203, 1995.

[12] M Sarkar, J Lu, and G J Pielak. Protein crowder charge and protein stability. *Biochemistry*, 53(10):1601–1606, 2014.

[13] Y Trosel, L P Gregory, V K Booth, and A Yethiraj. Diffusion nmr and rheology of a model polymer in bacterial cell lysate crowders. *Biomacromolecules*, 2023.

[14] Venketesh Thrithamara Ranganathan, Saman Bazmi, Stefan Wallin, Yun Liu, and Anand Yethiraj. Is ficoll a colloid or polymer? a multitechnique study of a prototypical excluded-volume macromolecular crowder. *Macromolecules*, 55(20):9103–9112, 2022.

[15] F Palombo and D Fioretto. Brillouin light scattering: applications in biomedical sciences. *Chemical Reviews*, 119(13):7833–7847, 2019.

[16] S. V. Adichtchev, Y. A. Karpegina, K. A. Okotrub, M. A. Surovtseva, V. A. Zykova, and N. V. Surovtsev. Brillouin spectroscopy of biorelevant fluids in relation to viscosity and solute concentration. *Physical Review B*, 99(6):062410, 2019.

[17] N. J. Tao and S. M. Lindsay. Reorientational relaxation of water molecules in licl solution studied by depolarised rayleigh scattering. *Journal of Physics: Condensed Matter*, 1(44):8709, 1989.

[18] N. J. Tao. Light scattering spectroscopy studies of water molecules in dna. *Water and Biological Macromolecules*, page 266, 1993.

[19] M. Bailey, M. Alunni-Cardinali, N. Correa, S. Caponi, T. Holsgrove, H. Barr, N. Stone, C. P. Winlove, D. Fioretto, and F. Palombo. Viscoelastic properties of biopolymer hydrogels determined by brillouin spectroscopy: A probe of tissue micromechanics. *Science Advances*, 6:eabc1937, 2020.

[20] S. C. Ng, T. J. C. Hosen, and L. M. Gan. Brillouin light-scattering from poly(vinyl alcohol) hydrogels. *Journal de Physique Letters*, 46(18):887–892, 1985.

[21] J. A. Marqusee and J. M. Deutch. Brillouin light scattering from polymer gels. *J. Chem. Phys.*, 75(11):5239–5245, 1981.

[22] G. T. Andrews, A. M. Polomska, E. Vazsonyi, and J. Volk. Brillouin light scattering from porous silicon films and multilayers. *Physica Status Solidi (a)*, 204(5):1372–1377, 2007.

[23] G. T. Andrews. Acoustic characterization of porous silicon. In L. Canham, editor, *Handbook of Porous Silicon*, chapter 53, pages 691–703. Springer International, 2018.

[24] W H Fissell, C L Hofmann, R Smith, and M H Chen. Size and conformation of ficoll as determined by size-exclusion chromatography followed by multiangle light scattering. *American Journal of Physiology-Renal Physiology*, 298(1):F205–F208, 2010.

[25] T Tumolo, L Angnes, and M S Baptista. Determination of the refractive index increment (dn/dc) of molecule and macromolecule solutions by surface plasmon resonance. *Analytical Biochemistry*, 333(2):273–279, 2004.

[26] J Ostwald, W Pazold, and O Weis. High-resolution brillouin spectroscopy of water. *Applied Physics*, 13:351–356, 1977.

[27] J Xu, X Ren, W Gong, R Dai, and D Liu. Measurement of the bulk viscosity of liquid by brillouin scattering. *Applied Optics*, 42(33):6704–6709, 2003.

[28] DA Pinnow, SJ Candau, and TA Litovitz. Rayleigh scattering: orientational relaxation in liquids. *The Journal of Chemical Physics*, 49(1):347–362, 1968.

[29] S. A. Lee, M. R. Flowers, W. F. Oliver, A. Rupprecht, and S. M. Lindsay. Brillouin-scattering study of hyaluronic acid: dynamic coupling with the water of hydration and phase transitions. *Physical Review E*, 47(1):677, 1993.

[30] M Pochylski, F Aliotta, Z Blaszczak, and J Gapiński. Structuring effects and hydration phenomena in poly (ethylene glycol)/water mixtures investigated by brillouin scattering. *The Journal of Physical Chemistry B*, 110(41):20533–20539, 2006.

[31] J Rodenburg, M Dijkstra, and R van Roij. Van't hoff's law for active suspensions: the role of the solvent chemical potential. *Soft Matter*, 13(47):8957–8963, 2017.

[32] M A Al-Jalali, I F Aljghami, and Y M Mahzia. Virial expansion and its application to oxygen spectroscopic measurements at 1270 nm band. *Journal of the Chemical Society of Pakistan*, 37(6), 2015.

[33] RA Pethrick. Acoustic studies of polymers. In *Static and Dynamic Properties of the Polymeric Solid State: Proceedings of the NATO Advanced Study Institute, held at Glasgow, UK, September 6–18, 1981*, pages 241–249. Springer, 1982.

[34] W. Gtri, H. Bey, A. Aschi, L. Bitri, and T. Othman. Impact of macromolecular crowding on structure and properties of pepsin and trypsin. *Materials Science and Engineering C*, 72:98–105, 2017.

[35] L. C. Acosta, G. M. Perez-Goncalves, G. J. Pielak, and A. H. Gorensek-Benitez. Large cosolutes, small cosolutes, and dihydrofolate reductase activity. *Protein Science*, 26:2417–2425, 2017.

[36] A. Orecchini, A. Paciaroni, A. DeFrancesco, C. Petrillo, and F. Sacchetti. Collective dynamics of protein hydration water by brillouin neutron spectroscopy. *Journal of the American Chemical Society*, 131(13):4664–4669, 2009.

[37] Raymond D Mountain. Thermal relaxation and brillouin scattering in liquids. *Journal of Research of the National Bureau of Standards. Section A, Physics and Chemistry*, 70(3):207, 1966.

Chapter 5

Growth and Inelastic Laser Light Scattering Studies of Satellite Tobacco Mosaic Virus Crystals

Abstract: In recent years, there has a been growing interest in the elastic properties of macromolecular structures. The elastic properties of viruses, however, are still hardly known. Solutions of satellite tobacco mosaic virus were prepared through centrifugation of infected tobacco leaves and ultrapure water. Satellite tobacco mosaic virus solutions were subsequently used to grow polycrystalline structures of satellite tobacco mosaic virus on various substrates via hang drop vapour diffusion methods. Room temperature Brillouin light scattering experiments were performed on polycrystalline satellite tobacco mosaic virus. Brillouin spectra of polycrystalline satellite tobacco mosaic virus contained peaks which were determined to be due to longitudinal acoustic modes. Such peaks were used to approximate the sound velocity and attenuation within the crystals.

5.1 Introduction

Satellite tobacco mosaic virus (STMV) is an icosahedral ssRNA virus comprised of 60 identical capsid subunits with a triangulation number of T = 1. As a satellite virus, STMV does not encode a capsid protein and therefore lacks the ability to self replicate. Though it cannot self replicate, STMV may spread when in the presence of a helper virus. The helper virus most commonly associated with STMV is tobacco mosaic virus, TMV.

Macromolecular crystals, such as STMV crystals, typically grow in very narrow ranges. They can usually only grow in temperatures ranging from 0°C - 30°C, and fairly neutral pH ranges. Furthermore, macromolecular crystallization requires an incredibly high solvent content, no less than 30%. In most cases, the solvent content in solution is between 40% - 60% [1], Macromolecules in solution typically crystallize in small islands which eventually branch together. As such, bond strength within crystals is typically weak, leading to brittle crystals. This also contributes to high levels of disorder in these crystals. Unlike conventional crystals, macromolecular crystals often have a large degree of hydration. The resulting crystals also exhibit a large amount of polymorphism. For example, STMV crystals can be orthorhombic, monoclinic, or cubic. The cell size of macromolecular crystals are large, ranging from edge lengths of 30 Å to several hundred Å.

Crystallization of proteins, RNA, and viruses employ many of the same mechanisms as conventional crystals. Some of these growth mechanisms include spiral dislocation, 2D nucleation, random nucleation, and 3D aggregation. Unlike conventional crystallization, however, macromolecular crystallization may employ different mechanisms in the same face, or change from one mechanism to another [2].

While crystallization of viruses and proteins dates back as far as the 1940's [3, 4], crystallization of STMV has only been explored over the last 30 years [5]. The growth of STMV crystals has been observed by means of atomic force microscopy in real time over durations of several hours by Malkin *et al.* [6]. During this time, crystals grew from microcrystals of size 40 - 50 μm to mature crystals of size 0.5 mm. Importantly, STMV crystallized differently from other macromolecules observed. No dislocations were observed in STMV crystals. The dominant growth mechanism of STMV was continuous sedimentation and absorption of three dimensional nuclei. Upon absorption, nuclei continue to grow by both two dimensional nucleation, growth in the normal direction, and by step flow over the surface of the larger crystal. These nuclei rapidly develop into multi layer plateaus. The heights of the plateaus varied, ranging from 12 - 510 nm (8 - 34 layers) [6].

While crystallization of viruses and other macromolecules has been well researched over the last hundred years, the exploration of the elastic properties of such crystals is still a relatively new field of research. As such there have been few studies on the elastic properties of macromolecular crystals and, in particular, virus crystals[7–11]. Furthermore, there has been very little work done exploring the elastic properties of STMV crystal structures. In a study by Stephanidis *et al.*, Brillouin light scattering experiments were performed on STMV solutions, hydrated STMV crystals, and fully dehydrated STMV crystals [12]. For STMV solutions, all spectra showed only Brillouin features characteristic of aqueous buffers. This was likely due to the small concentration of STMV in the solution. STMV crystals were grown using hang-drop vapour diffusion techniques. Resulting crystals in this study had cubic symmetry. After growth, crystals were transferred into sealed glass capillaries with minimum mother liquor to ensure full hydration and stability of crystals. Finally, dry crystals were prepared by slowly evaporating mother liquor in unsealed capillaries in air over several days. Dry crystals became slightly opaque, but STMV crystal shape and crystalline organization remained unchanged. A low frequency Brillouin peak was observed in the spectra for hydrated STMV crystals which was not apparent in spectra for dehydrated crystals. This peak was attributed to the aqueous buffer within the wet crystal. A broader and higher frequency peak was also observed in both types of crystals, which was attributed to be due to a longitudinal acoustic mode. There was a significant shift in phonon peak frequency between hydrated and dehydrated crystals, leading to a much higher phonon velocity in dehydrated samples.

The contents of this study are twofold. First, STMV crystals were grown using hang-drop vapour diffusion techniques. Various techniques were used to optimise crystal growth, until such a technique was able to consistently grow crystals which were suitible in size. Secondly, Brillouin light scattering experiments were performed on STMV crystals. Such experiments were performed in an attempt to observe longitudinal acoustic modes as well as individual phonon modes propagating within the sample. Longitudinal bulk mode frequency was subsequently used to approximate phonon velocity within the crystals.

5.2 Satellite Tobacco Mosaic Virus Crystals - Growth

5.2.1 Harvesting of Satellite Tobacco Mosaic Virus

Nicotiana rustica (tobacco) seeds were sown and germinated in the Memorial University Botanical Gardens. At roughly two weeks of growth, plants were transferred to our laboratory where they were infected with STMV and TMV by swabbing the leaves with infected plant material (obtained from Dr. Ayala Rao, University of California, Riverside). After the first batch of plants were infected, leftover infected plant material was also used to infect subsequent batches of plants. Infection was allowed to propagate through the plants for roughly two weeks and was manifested in a mottling of the leaves.

Harvesting of virus particles was done via centrifugation. Infected leaves were ground to a paste using a mortar and pestle. This paste was then added to the centrifugal cell and topped off with ultrapure water. The cell chosen was an Amicon Ultra-4 10K centrifugal filter tube. This tube has a filter within it with a maximum filtration size of 10 kDa. STMV has an atomic mass of 6.3 kDa, and passed through the filter while TMV, a rod-like virus with a lenghth of 300 nm, width of 18 nm, and mass of 126 kDa did not. This ensured that the resulting solutions contained only STMV in ultrapure water.

Centrifugation was performed using an IEC Clinical bench-top centrifuge with a six place fixed angle 45° rotor. Samples were centrifuged at a maximum speed of 4450 RPM for a minimum of four hours. This resulted in a relative centrifugal force of 2400 × g. In early centrifugation attempts, residual plant matter was discovered within the virus solution, having settled after a few weeks. As such, STMV solutions were further centrifuged one or two extra times to ensure higher purity of solution in later trials, including all those used for crystallization in this work. No residual plant matter was observed in final solutions.

5.2.2 Crystallization Process

Crystallization of STMV was performed using a hang-drop vapour diffusion technique. This technique is commonly used in macromolecular crystallization [2, 13, 14]. In this process, a droplet containing virus particles, buffer solutions, and a precipitant, often a salt, is suspended over a reservoir solution of similar buffers and precipitants. Through vapour transfer from the droplet to the reservoir, the two are able to equilibriate. The concentration of virus in the droplet begins low, but as vapour diffuses from the droplet, its volume decreases. This change in volume, without exchange in number of virus particles in the droplet, subsequently increases the virus concentration in the droplet. As the concentration of virus particles in the drop increases, so to do the number of interactions between particles. This leads to crystal growth within the droplet [14].

Specific steps in crystallization of STMV followed the methods described by Valverde and Dodds [5]. Solutions of $(NH_4)_2SO_4$ were prepared by dissolving $(NH_4)_2SO_4$ powder in ultrapure water. While different concentrations were used in preliminary crystal growth attempts, the most consistent results were obtained using a 10% saturated solution of $(NH_4)_2SO_4$. 2-3 mL of $(NH_4)_2SO_4$ was used to fill the base of the vapour diffusion chamber, to be used as the reservoir. Equal volumes of $(NH_4)_2SO_4$ solution and STMV solution were mixed together to create the drop solution. This process was used to grow STMV crystals with orthorhombic symmetry [14].

Table 5.1 shows the different substrates on which crystal growth was attempted. Crystals were initially grown on the underside of the lid of the Thermo-Fisher Scientific BioLite 12 well vapour diffusion cells. Small droplets of virus-reservoir solution, $\sim 10-50\ \mu$L, were carefully placed on the substrate. The lid was then carefully inverted and placed onto the vapour diffusion chamber, ensuring that the droplets were not disturbed in the process. Crystals were left for two weeks to grow. Crystals grown on the vapour diffusion cell lid grew into polycrystalline clusters with side lengths of a few hundred micrometers. Crystals clusters were white and semi-transparent. These crystals were extremely brittle, and could not be removed from the cell lid, which was too large for the Brillouin scattering apparatus, without complete destruction of the crystals.

In order to transport crystals from growth cells to the Brillouin scattering apparatus, STMV crystals had to be grown on a separate surface, which was adhered to the lid. Of the surfaces used to grow crystalline STMV, the most successful was crystalline silicon. As such, all samples discussed in this work were grown on silicon. Small pieces of silicon were cleaved from a larger (100) oriented piece of silicon, and were adhered to the lid of the vapour diffusion cell. A small scratch was made in the silicon, to promote nucleation, and crystals were grown using the above method. Figure 5.1 shows a STMV crystal grown by the above method. Four such crystals were used in Brillouin scattering experiments.

As shown in Table 5.1, attempts to grow STMV crystals were made on miscoscope slides, to enable transport from growth cells to the Brillouin scattering apparatus. Microscope slides used were hydrophilic, and subsequently droplets could not be formed on the surface. Pools of virus solution were left to crystallize over the same time period, however no such crystals were formed.

Previous work on nucleation of protein crystals has used porous surfaces, with pore diameters on the order of 10 nm, as a nucleation surface in vapour diffusion processes [15]. As such, STMV crystals were grown on porous silicon substrates via hang drop vapour diffusion. There was no substantial difference is size or morphology of crystals grown by this method compared to crystals grown on crystalline silicon.

Table 5.1: Surfaces used to attempt to grow STMV crystals.

Substrate	Success	Comments
Cell Lid	✓	Crystals were brittle and could not be removed without destroying.
Microscope Slide	×	Slides were hydrophilic and droplets did not form. Pools of virus-containing solution left to crystallize, but no crystals formed.
Crystalline Silicon	✓	Small scratch made on silicon surface to promote nucleation. Crystal clusters successfully grown to sizes of a few hundred μm.
Porous Silicon	✓	Substrate pore diameter ~ 10 nm. Crystal clusters successfully grown, but not substantially different from those grown on crystalline silicon.

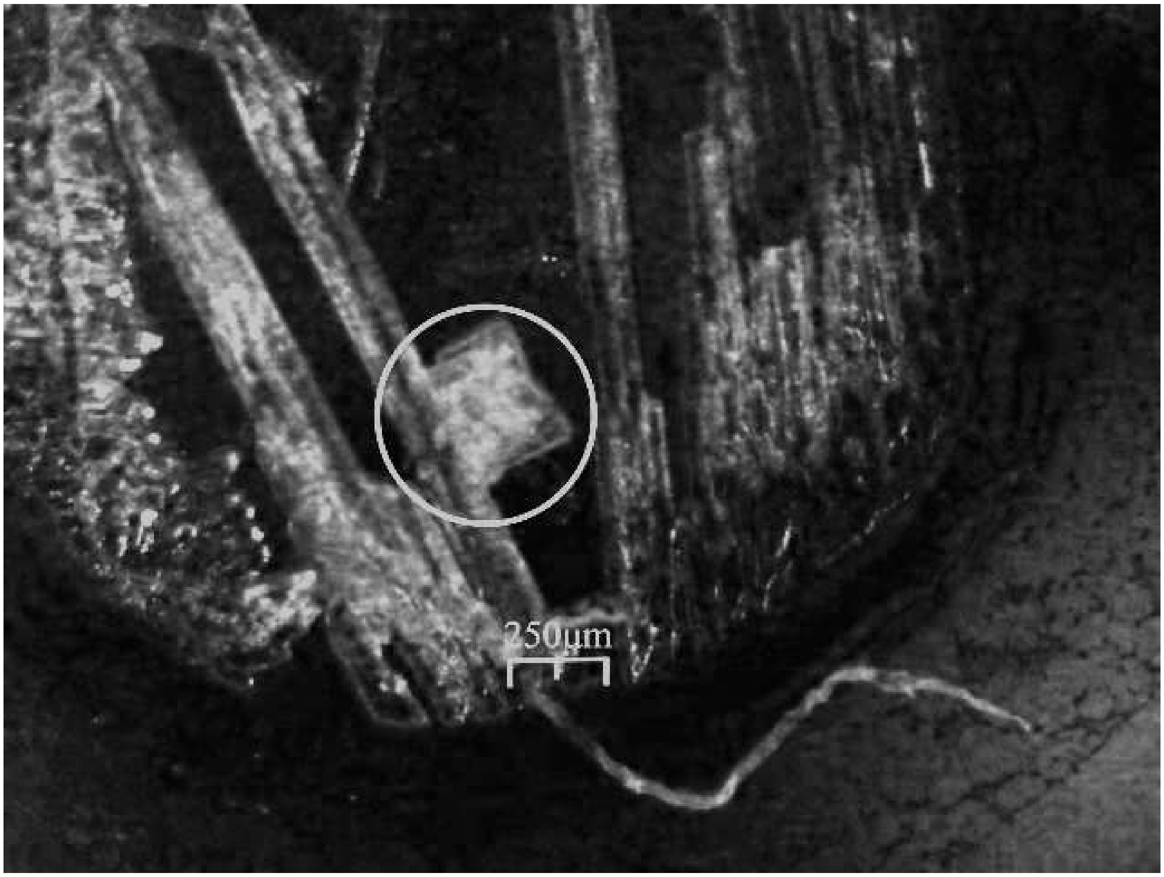

Figure 5.1: Satellite tobacco mosaic virus crystal on a silicon substrate. Crystallized $(NH_4)_2SO_4$ is also seen around the virus crystal. Image taken using Supereyes digital microscope.

5.3 Satellite Tobacco Mosaic Virus Crystals - Brillouin Scattering

Brillouin light scattering experiments were performed at room temperature in a 180° backscattering geometry using the set-up shown in Ref. [16]. A Nd:YVO_4 laser with a wavelength of 532 nm and power of 1.66 W was used to probe phonons in crystals. To ensure STMV crystals were not damaged by laser light, power was reduced to 10 mW at the sample via a variable neutral density filter. Incident horizontally polarized light was focused on the sample with a 5 cm lens with an f number of f/2.8, which was subsequently used to collect and collimate scattered light. This scattered light was focused by a 40 cm lens onto the 450 μm entrance pinhole of a six-pass tandem Fabry-Perot interferometer. The interferometer had a free spectral range of 50 GHz and finesse of $\sim$100. After frequency analysis, the scattered light was focused onto a 700 μm entrance pinhole where it is collected by a photomultiplier. Due to the small size of the STMV crystals, a Supereyes 13MP/5MP 500X Handheld Digital Microscope was used to position the incident beam (diameter $\sim$50 μm) onto the center of the crystal prior to spectrum collection.

5.3.1 Brillouin Spectra of STMV Crystals

Figure 5.2 shows representative Brillouin spectra collected from a STMV crystal sample at various angles of incidence. Two sets of Brillouin peaks were observed in most spectra. The lower frequency-shift peak at $\sim 14-18$ GHz was determined to be due to a bulk acoustic mode propagating within the STMV crystal due to its similarity in frequency shift to that previously reported for cubic STMV crystals [12]. Due to the anisotropy of the samples, it is impossible to know the direction being probed within the sample, though polarized Brillouin spectroscopy could be used to determine whether this bulk mode is longitudinal or transverse. The second peak, with a frequency shift of ~25 GHz is of unknown origin, but is suspected to be due to residual $(NH_4)_2SO_4$ on the silicon surface.

Figure 5.3 shows Brillouin peak frequency plotted against the angle of incidence, measured relative to the normal direction of the sample, for four STMV crystals. Though there was no systematic variation of longitudinal peak frequency, significant variance was observed in peak frequency between spectra, with the largest amount of variance with a sample being ~6 GHz, and the smallest being ~2 GHz. The wide range of uncertainties in shift is due largely to variation in peak intensity, with the larger uncertainties associated with peaks that were very weak in intensity.

Table 5.2 shows average frequency shift of the longitudinal peaks for all samples in this study. Three of the samples have similar peak shifts, while the fourth has a slightly higher shift. All frequencies recorded within this work are within the range reported in Ref. [12]. It is important to note, however, that crystals grown in this work were grown under different conditions, and subsequently have a different crystal structure.

Table 5.2 shows average longitudinal phonon velocity of STMV crystals obtained using the well-known Brillouin equation

$$v = \frac{f\lambda}{2n}. \tag{5.1}$$

The refractive index n was estimated to be 1.52, as reported for cubic STMV crystals [12]. The same trend noticed with longitudinal frequency was also observed in longitudinal bulk mode velocity, which is expected since v is directly proportional to f. Bulk mode velocities for the crystals studied in the present work, which are largely

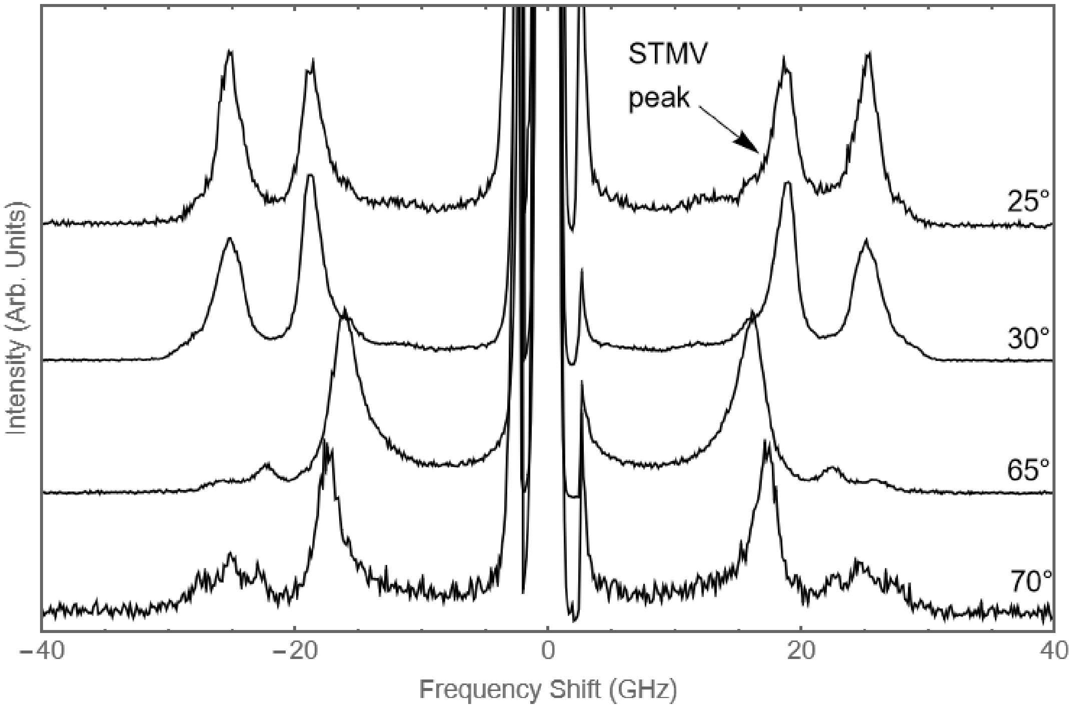

Figure 5.2: Brillouin spectra collected from satellite tobacco mosaic virus crystal at various angles of incidence. The peak labelled “STMV peak” was determined to be due to a longitudinal bulk acoustic mode propagating in the crystal.

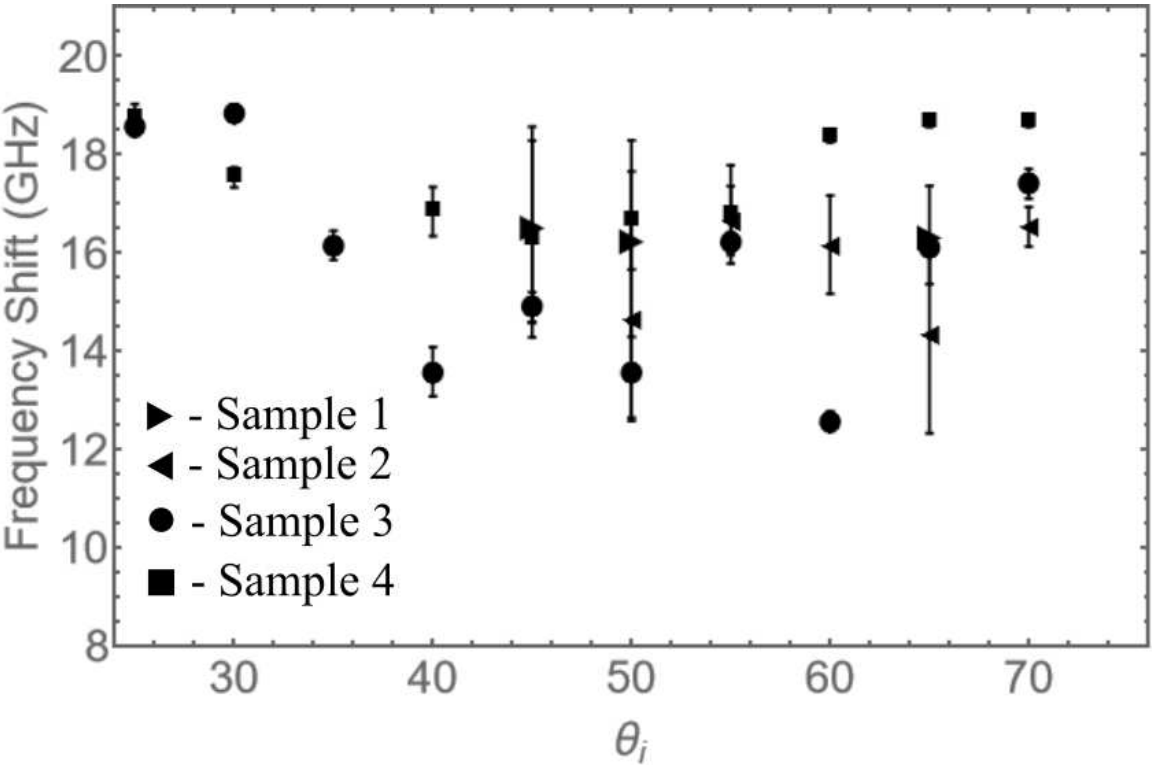

Figure 5.3: Longitudinal Brillouin peak frequency shift for satellite tobacco mosaic virus crystals versus angle of incidence.

Table 5.2: Longitudinal phonon frequency, velocity, peak width, and attenuation for satellite tobacco mosaic virus crystals from the present work and a previous study.

Source	Crystal Symmetry	Average Phonon Frequency (GHz)	Average Velocity (km/s)	FWHM (GHz)	Attenuation ($\times 10^6$ m^{-1})	Normalized Attenuation
Present Work	Orthorhombic	16 ± 2	2.8 ± 0.2	-	-	-
		16 ± 2	2.8 ± 0.2	-	-	-
		15.8 ± 0.3	2.71 ± 0.05	3.2 ± 0.3	3.6 ± 0.4	0.64 ± 0.07
		17.6 ± 0.6	3.02 ± 0.08	1.4 ± 0.2	1.5 ± 0.2	0.25 ± 0.04
Hydrated STMV Crystal [12]	Cubic	11.2 ± 0.5	1.92 ± 0.08	-	-	0.76
Dehydrated STMV Crystal [12]	Cubic	20 ± 0.5	3.43 ± 0.08	-	-	0.3
WIV [10]	Film	-	2.9 ± 0.2	-	-	-
Bulk PMMA [17]	-	-	2.80	-	-	-
Lysozyme [7]	Tetragonal	-	~ 1.82	-	-	-

dehydrated, are comparable to those reported for cubic STMV crystals [12], falling within the range presented for hydrated and dehydrated crystals.

Phonon velocities recorded for STMV are within a comparable range to those of crystals comprised of PMMA and WIV, which are, structurally, similar in shape to STMV [10, 17]. Furthermore, crystals made of long chain macromolecules such as lysozyme, or larger viruses such as TMV have lower phonon velocities than STMV crystals [7, 9, 18].

Longitudinal peak linewidths, shown in Table 5.2, were measured in Brillouin spectra. Between the four samples studied within this work, Brillouin peak intensity was extremely inconsistent. Many of the peaks observed were not well defined, leading to larger uncertainties shown in Figure 5.3. This limited the number of Brillouin peaks from which a reliable linewidth could be extracted. Table 5.2 shows average linewidth for the longitudinal bulk mode peak for each STMV sample. For STMV samples 1 and 2, all Brillouin peaks observed were extremely weak and poorly defined, and measurement of linewidth was not possible. For samples 3 and 4, there were some spectra which contained strong, sharp peaks. These spectra were used to calculate the average linewidth shown in Table 5.2. It is of note that the longitudinal bulk mode peak observed in one spectrum from sample 3 showed anomalously large linewidth, which contributed to the large difference between the average linewidths shown in Table 5.2.

Average linewidth data, in conjunction with average phonon velocity, was used to calculate hypersound attenuation using the equation

$$\alpha = \frac{\pi \Gamma_B}{v}, \tag{5.2}$$

where Γ_B is the Brillouin peak width. Table 5.2 shows hypersound attenuation for two STMV crystal samples studied in this work. As with linewidth, the values calculated for attenuation show a large difference between the two samples. Due to the growth conditions of these crystals, there are a few possible contributing factors to this difference in attenuation. Since these crystals grew in clusters, there are interfaces between crystals. As such, the difference in interfaces between the two crystals could be a contributing factor in this difference in attenuation, as interfaces between two materials increase the hypersound attenuation. Secondly, a difference in hydration state could also contribute to the difference in attenuation of the two crystals [12].

Table 5.2 shows normalized sound attenuation parameter, calculated for STMV crystals using

$$\Lambda = \frac{\Gamma_B}{f}. \tag{5.3}$$

Similar to previously discussed elastic parameters, these values fall within the range between those presented for hydrated and dehydrated STMV crystals [12]. This further demonstrates the difference in hydration state between these two crystals.

5.3.2 Search for Individual Virus Eigenmodes

Previous studies have shown that low frequency eigenmodes, corresponding to higher quantum numbers, of individual spherical particles may be observed by inelastic light scattering spectroscopy for cases in which the particle size is comparable to the wavelength of the probing laser light [10, 17, 19–21]. This theory has been expanded to virus particles, including those in crystals, and predicts the frequency of individual virus vibrational modes to be

$$f_{loc} \simeq \frac{V_T}{D}, \tag{5.4}$$

where V_T is the transverse bulk mode velocity and D is the virus diameter [10]. This relationship has been used to determine particle size when the frequency of vibration and velocity is known [22, 23], but was used in the present work to estimate the frequency at which such modes might be observed in the Brillouin spectrum of STMV virus crystals because the diameter of STMV is known and the velocity can be estimated from $V_T = X \times V_L$ [24]. For STMV, previous estimations for the ratio of longitudinal and transverse velocities have been $X = 0.25 - 0.5$. While the diameter of STMV is considerably smaller than the wavelength of the probing visible light, this method was used to estimate the frequency range over which individual virus modes might be observed in the spectrum. This range was found to be $\sim 100 - 200$ GHz. As such, Brillouin spectra were collected with a free spectral range of up to 250 GHz in an attempt to observe vibrational modes from individual virus molecules. Unfortunately, no additional modes were observed in such spectra. This is not an unexpected result, as the wavelength of light used in this work (532 nm) is much longer than the diameter of STMV (∼17 nm), thus further validating the theory that such modes are inactive in particles where D $\ll \lambda$ [12].

5.4 Conclusion

In this study, STMV crystals were grown from solution via hang drop vapour diffusion techniques. Crystal growth was performed on several substances, however crystalline silicon was found to be the most suitable due to the size of crystals grown on the surface. Crystals grown on such surfaces grew into polycrystalline clusters on the order of a few hundred microns in length.

Brillouin scattering experiments were performed on STMV crystals. Two peaks were observed in spectra, with one being identified as being due to a longitudinal bulk mode within the STMV crystal. Peak frequency shift and width were used to calculate elastic properties of crystallizes STMV, with phonon velocities falling within the range of results reported in previous works. Brillouin peak frequency and linewitdh were also used to calculate hypersound attenuation and normalized sound attenuation. The results for normalized attenuation were found to be within the range previously reported for hydrated and dehydrated STMV crystals. These viscoelastic properties varied between crystals, which was determined to be a result of a difference in hydration state between the crystals.

5.5 Acknowledgments

GTA acknowledges the support of the Natural Sciences and Engineering Research Council of Canada (RGPIN-2019-04970). SJS would like to acknowledge and express thanks to Dr. A Rao for providing initial infected plant material.

Bibliography

[1] B W Matthews. Solvent content of protein crystals. *Journal of Molecular Biology*, 33(2):491–497, 1968.

[2] A McPherson. *Crystallization of Biological Macromolecules*, volume 586. Cold Spring Harbor Laboratory Press Cold Spring Harbor, NY, 1999.

[3] S Cohen. *Journal of Biological Chemistry*, 144(2):353–362, 1942.

[4] Z Kam, HB Shore, and G Feher. *Journal of Molecular Biology*, 123(4):539–555, 1978.

[5] R A Valverde and J A Dodds. *Journal of General Virology*, 68(4):965–972, 1987.

[6] AJ Malkin, TA Land, Yu G Kuznetsov, A McPherson, and JJ DeYoreo. *Physical Review Letters*, 75(14):2778, 1995.

[7] M Tachibana, K Kojima, R Ikuyama, Y Kobayashi, and M Ataka. *Chemical Physics Letters*, 332(3):259–264, 2000.

[8] A A Chernov. *Journal of Structural Biology*, 142(1):3–21, 2003.

[9] M Talati and P K Jha. *Physical Review E*, 73(1):011901, 2006.

[10] RD Hartschuh, SP Wargacki, H Xiong, J Neiswinger, A Kisliuk, S Sihn, V Ward, RA Vaia, and AP Sokolov. *Physical Review E*, 78(2):021907, 2008.

[11] S Sirotkin, A Mermet, M Bergoin, V Ward, and J L Van Etten. Viruses as nanoparticles: Structure versus collective dynamics. *Physical Review E*, 90(2):022718, 2014.

[12] B Stephanidis, S Adichtchev, P Gouet, A McPherson, and A Mermet. *Biophysical Journal*, 93(4):1354–1359, 2007.

[13] A McPherson and L J DeLucas. Microgravity protein crystallization. *Microgravity*, 1:15010, 2015.

[14] A J Malkin, J Cheung, and A McPherson. *Journal of crystal growth*, 126(4):544–554, 1993.

[15] V M Bolanos-Garcia and N E Chayen. New directions in conventional methods of protein crystallization. *Progress in biophysics and molecular biology*, 101(1-3):3–12, 2009.

[16] G. T. Andrews. Acoustic characterization of porous silicon. In L. Canham, editor, *Handbook of Porous Silicon*, chapter 53, pages 691–703. Springer International, 2018.

[17] T Still, R Sainidou, M Retsch, U Jonas, P Spahn, GP Hellmann, and G Fytas. The "music" of core- shell spheres and hollow capsules: Influence of the architecture on the mechanical properties at the nanoscale. *Nano letters*, 8(10):3194–3199, 2008.

[18] A A Balandin and V A Fonoberov. Vibrational modes of nano-template viruses. *Journal of Biomedical Nanotechnology*, 1(1):90–95, 2005.

[19] M Montagna. Brillouin and raman scattering from the acoustic vibrations of spherical particles with a size comparable to the wavelength of the light. *Physical Review B*, 77(4):045418, 2008.

[20] T Still, M Mattarelli, D Kiefer, G Fytas, and M Montagna. Eigenvibrations of submicrometer colloidal spheres. *The Journal of Physical Chemistry Letters*, 1(16):2440–2444, 2010.

[21] K T Tsen, E C Dykeman, O F Sankey, S D Tsen, N Lin, and J G Kiang. Probing the low-frequency vibrational modes of viruses with raman scattering—bacteriophage m13 in water. *Journal of biomedical optics*, 12(2):024009–024009, 2007.

[22] C Sun, Y Tsai, Y E Chen, T Liu, H Chen, H Wang, and C Lo. Resonant dipolar coupling of microwaves with confined acoustic vibrations in a rod-shaped virus. *Scientific reports*, 7(1):4611, 2017.

[23] J Burkhartsmeyer, Y Wang, K S Wong, and R Gordon. Optical trapping, sizing, and probing acoustic modes of a small virus. *Applied Sciences*, 10(1):394, 2020.

[24] L Saviot and D B Murray. Longitudinal versus transverse spheroidal vibrational modes of an elastic sphere. *Physical Review B*, 72(20):205433, 2005.

Chapter 6

Conclusion

Macromolecular systems have gained a significant amount of attention in the last few decades throughout different aspects of physics and biophysics. However, there have been very few experimental studies exploring the elastic properties of such systems. As such, this study's aim was to use Brillouin light scattering as a tool to explore the two most common forms of macromolecular systems: aqueous solutions and crystals. The first work presented in this study explored the viscoelastic properties of three different macromolecular solutions (Ficoll 70, Ficoll 400, and BSA) by means of Brillouin scattering over a range of concentrations. The second work presented explored the growth conditions of macromolecular crystals (STMV), and subsequently used Brillouin scattering to explore their elastic properties. Together, this ultimately allows us to observe these properties in three separate regimes of macromolecular systems: dilute solution, semi-dilute solution, and solid crystal.

6.1 Concentration Dependence of Elastic and Viscoelastic Properties of Aqueous Solutions of Ficoll and Bovine Serum Albumin by Brillouin Light Scattering Spectroscopy

6.1.1 Conclusion

Brillouin light scattering experiments were performed on solutions of Ficoll 70 and Ficoll 400 dissolved in D_2O, with concentrations ranging from 1% to 35% mass percent, and solutions of BSA dissolved in phosphate buffer, with concentrations ranging from 1% to 27% mass percent. Brillouin spectra from all solutions studied exhibited a single Brillouin peak, attributed the propagation of a longitudinal bulk mode. Frequency shifts and Brillouin peak linewidths of these longitudinal peaks were used to calculate viscoelastic properties, including hypersound velocity, bulk modulus, apparent viscosity, and hypersound attenuation. All of these properties experienced an increase in value with increasing solute concentration. However, the relationships between these properties and concentration could not be accurately described by models which have been previously been presented for systems of non-interacting particles. As such, a new model was presented to describe changes in hypersound frequency with changing concentration which incorporates solute-solute interactions.

In high concentration spectra collected for Ficoll 70 and Ficoll 400, a central peak was observed in Brillouin spectra. This peak was attributed to relaxation associated with hydration of solute molecules by D_2O and the occupation of D_2O within the hydration shell.

6.1.2 Future Work

Previous Brillouin light scattering studies have demonstrated a universality in the relationships between solute concentration and Brillouin peak frequency and linewidth for low concentration macromolecular solutions. The next logical step is, therefore, to repeat the experiments performed in this work on several different macromolecular solutions at high concentrations, specifically the semi-dilute region, when solute-solute interactions cannot be ignored. Some common, and well researched, macromolecules which would be good candidates to study include lysozyme, sucrose, and dextran. Spectra of these macromolecular solutions can then be used to examine the semi-dilute regime and compared to the model presented in this work. Furthermore, through examination of any central peaks observed in spectra, we may be able to further comment on the effects of hydration on crowding in macromolecular solutions. In particular, it would be interesting to investigate hydration of materials such as lysozyme, PEG, or other organic polymers wherein hydration has also been explored using other experimental techniques.

6.2 Growth and Inelastic Laser Light Scattering Studies of Satellite Tobacco Mosaic Virus Crystals

6.2.1 Conclusion

STMV crystals were grown on several different surfaces by use of hang drop vapour diffusion techniques. Of the surfaces used, crystalline silicon was determined to be the best due to the size of the crystals grown on it, as well as the ease of transport to the Brillouin scattering apparatus. Crystals grown using this technique grew into polycrystalline clusters, which were on the order of a few hundred micrometers in length.

Brillouin scattering experiments were performed on STMV crystals. Two peaks were observed in spectra, with one being determined to be due to a longitudinal bulk mode propagating within the STMV crystal, and the other one due to the residual $(NH_4)_2SO_4$ remaining on the silicon surface. Brillouin peak frequency and linewidth of the longitudinal mode peak were used to calculate elastic properties of the STMV crystals. Phonon velocities calculated for these crystals ranged from 2.71 km/s to 3.02 km/s, falling within the ranges previously presented for hydrated and dehydrated STMV crystals. Similarly, hypersound attenuation for STMV crystals ranged from 1.5×10^6 m^{-1} to 3.6×10^6 m^{-1}, and normalized attenuation ranged from 0.25 to 0.64, the latter of which also falls in the range given for hydrated and dehydrated crystals. The differences in elastic properties calculated for these has been attributed to differences in hydration state, as phonon velocities in these crystals increases, and attenuation decreases, as they become more dehydrated.

6.2.2 Future Work

When it comes to future studies on STMV crystals, there are several different angles from which we can approach. First and foremost, using different growth methods or surfaces, attempts can be made to grow large single crystals. One specific change which could be made to help grow larger single crystals is the use of a more precise centrifuge to separate virus particles from the leaves and helper viruses. Furthermore, the use of seed crystals may also be implemented to further increase the size of single crystals. Subsequently, Brillouin light scattering experiments can be carried out on single crystals, the data of which can be used to calculate elastic constants of the crystals. Furthermore, using different buffer solutions during the crystal growth process can lead to different crystal structures, such as the cubic STMV crystals which have been grown by Stephanidis *et al*. [1]. As such, crystals with different geometries can be grown in similar fashion, with subsequent Brillouin light scattering experiments to be performed on said crystals.

Bibliography

[1] B Stephanidis, S Adichtchev, P Gouet, A McPherson, and A Mermet. *Biophysical Journal*, 93(4):1354–1359, 2007.

Appendix A

Supplementary Material for: Concentration Dependence of Elastic and Viscoelastic Properties of Aqueous Solutions of Ficoll and Bovine Serum Albumin by Brillouin Light Scattering Spectroscopy

Table A.1: Brillouin peak frequency shift (f) and linewidth (Γ) for Ficoll 70, Ficoll 400, and Bovine Serum Albumin solutions at all concentrations studied.

	Ficoll 70		Ficoll 400		Bovine Serum Albumin	
Concentration (% wt.)	f_{F70} [± 0.05 GHz]	Γ_{F70} [± 0.09 GHz]	f_{F400} [± 0.05 GHz]	Γ_{F400} [± 0.09 GHz]	f_{BSA} [± 0.05 GHz]	Γ_{BSA} [± 0.09 GHz]
0	6.83	0.47	6.83	0.47	7.46	0.69
1	6.82	0.51	6.83	0.51	7.46	0.70
3	6.86	0.55	6.91	0.56	7.51	0.74
5	6.91	0.59	6.98	0.58	7.57	0.78
7	6.97	0.64	7.03	0.64	7.65	0.81
10	7.05	0.71	7.16	0.73	7.77	0.84
13	7.14	0.83	7.25	0.81	7.83	0.95
15	7.22	0.86	7.29	0.86	7.91	1.03
17	7.34	0.95	7.40	1.00	7.96	1.10
20	7.44	1.10	7.51	1.08	8.10	1.16
25	7.71	1.29	7.82	1.37	8.29	1.33
27	-	-	-	-	8.43	1.46
30	7.96	1.50	8.09	1.66	-	-
35	8.21	1.89	8.36	2.00	-	-

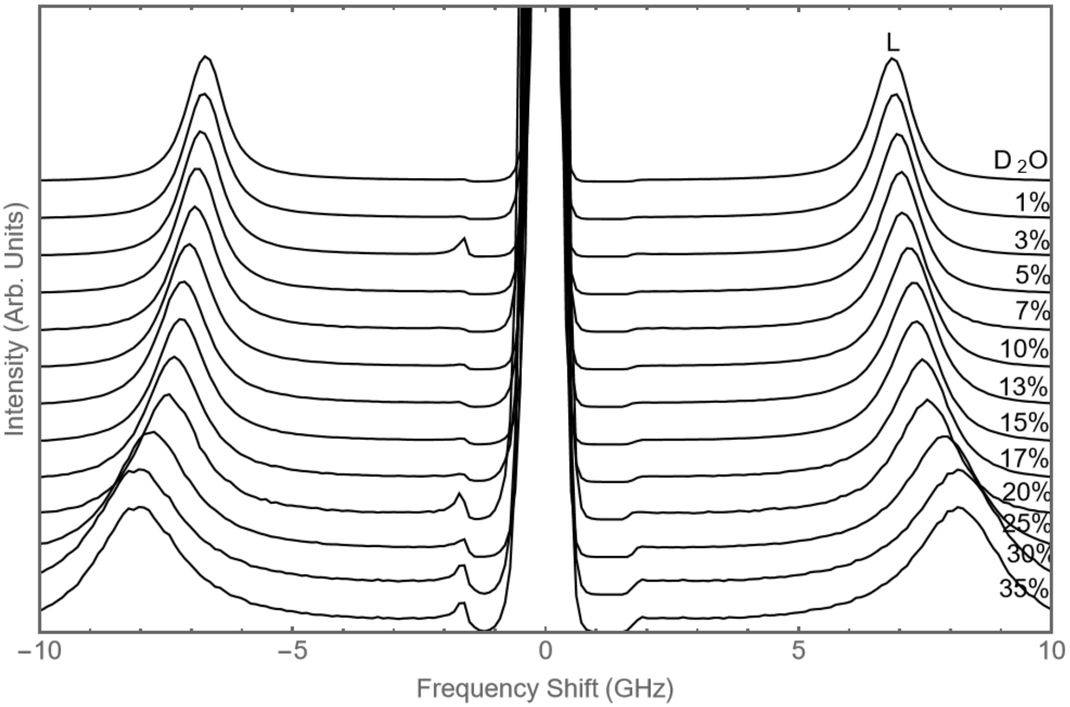

Figure A.1: Normalized Brillouin spectra collected from solutions of Ficoll 400 of various concentrations (wt%). L represents a longitudinal bulk mode.

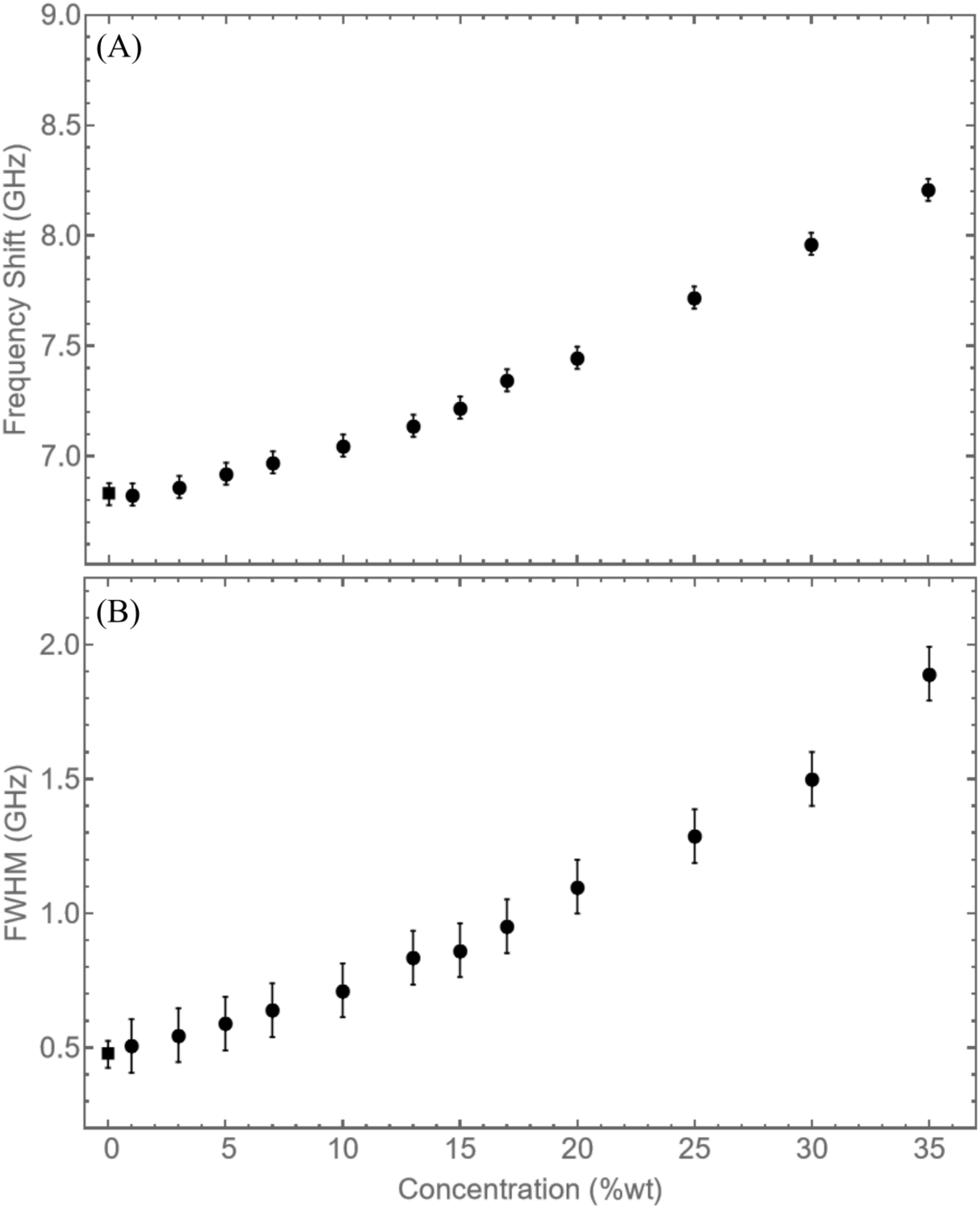

Figure A.2: Brillouin peak frequency (A) and linewidth (B) of Ficoll 70 as a function of solution concentration.

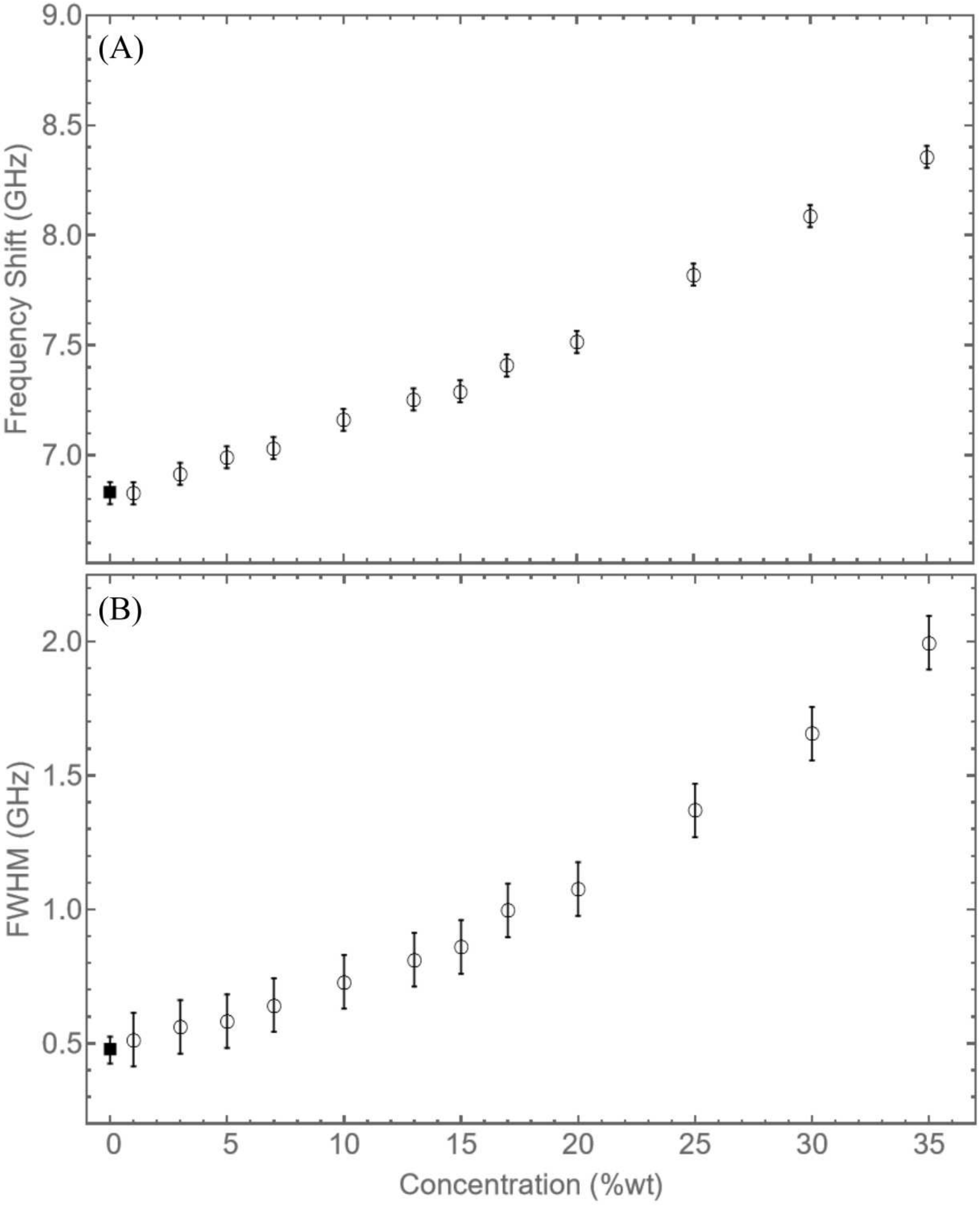

Figure A.3: Brillouin peak frequency (A) and linewidth (B) of Ficoll 400 as a function of solution concentration.

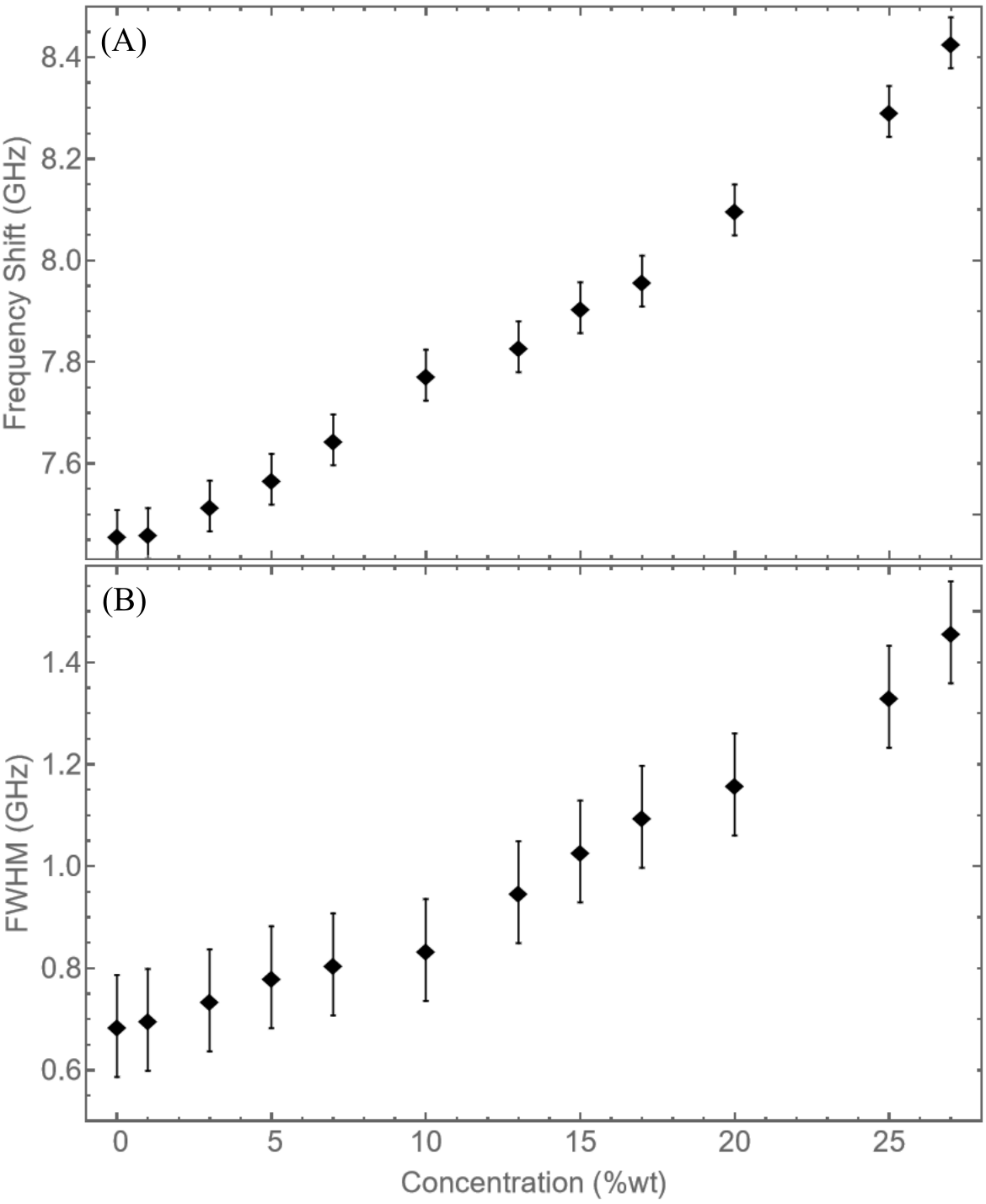

Figure A.4: Brillouin peak frequency (A) and linewidth (B) of BSA as a function of solution concentration.

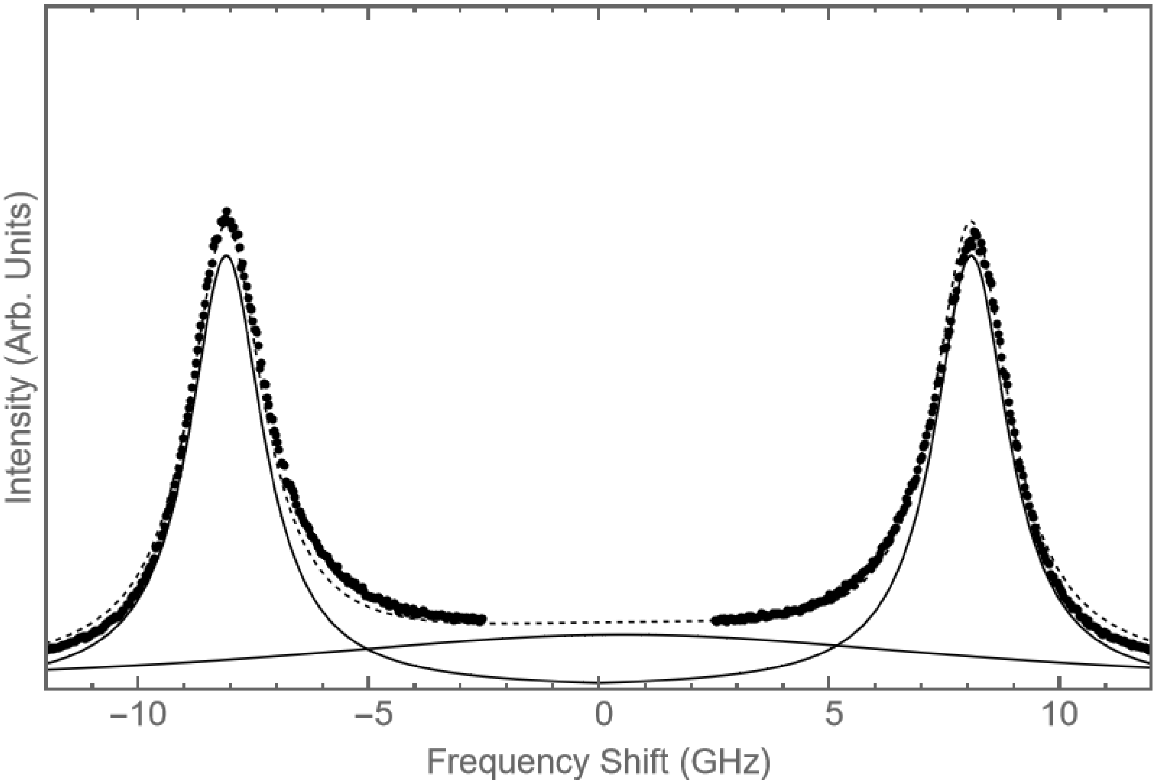

Figure A.5: Brillouin spectrum of Ficoll 400 with a concentration of 30%. Solid lines - central peak and Brillouin peak fits. Dashed line - sum of central peak and Brillouin peak fits.

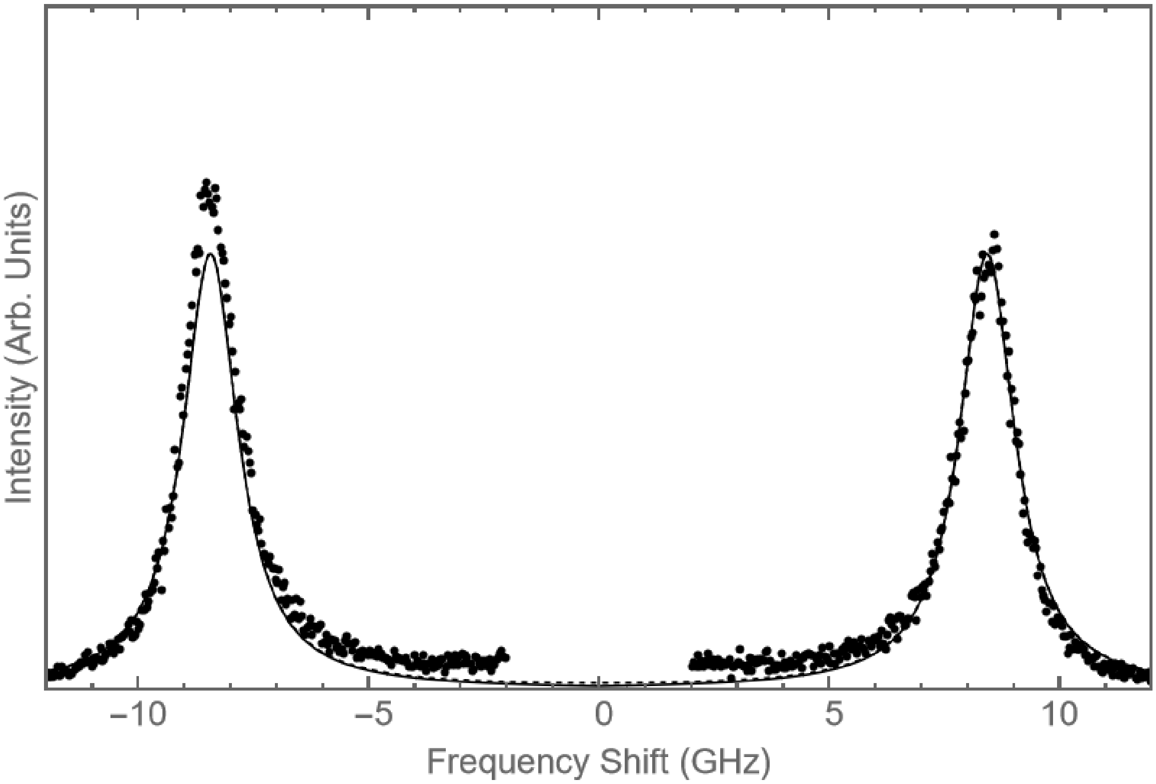

Figure A.6: Brillouin spectrum of BSA with a concentration of 27%. Solid lines - Brillouin peak fits. Dashed line - sum of Brillouin peak fits. No central peak was observed in such spectra.

Appendix B

Supplementary Material for: Growth and Inelastic Laser Light Scattering Studies of Satellite Tobacco Mosaic Virus Crystals

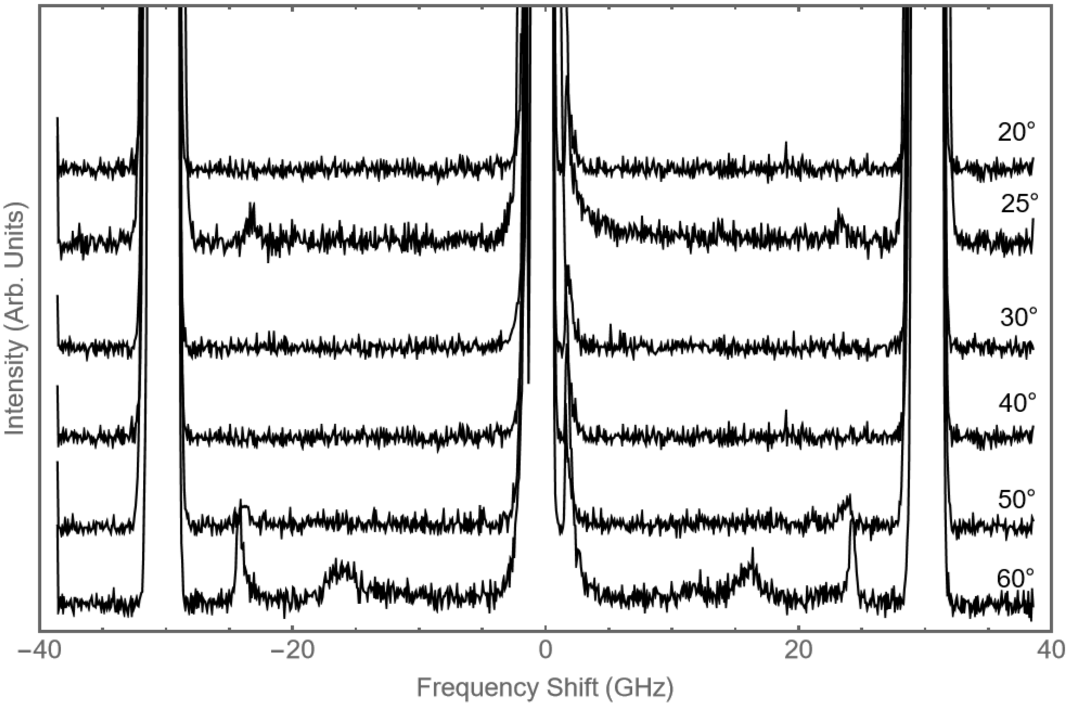

Figure B.1: Brillouin Spectra collected on STMV sample # 1.

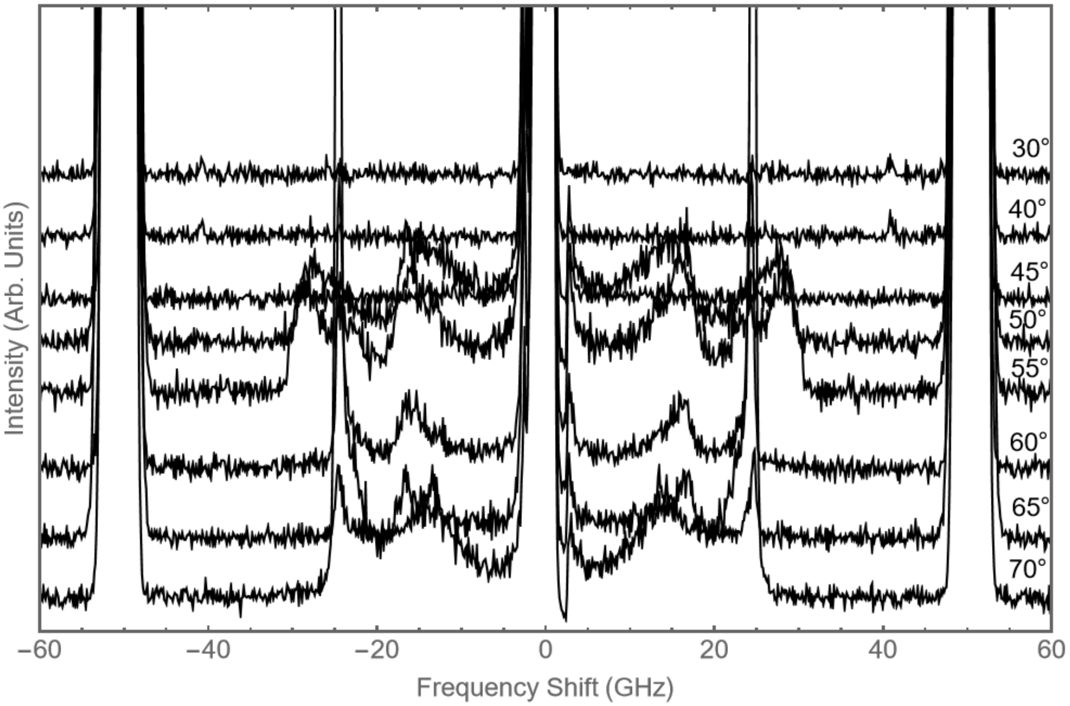

Figure B.2: Brillouin Spectra collected on STMV sample # 2.

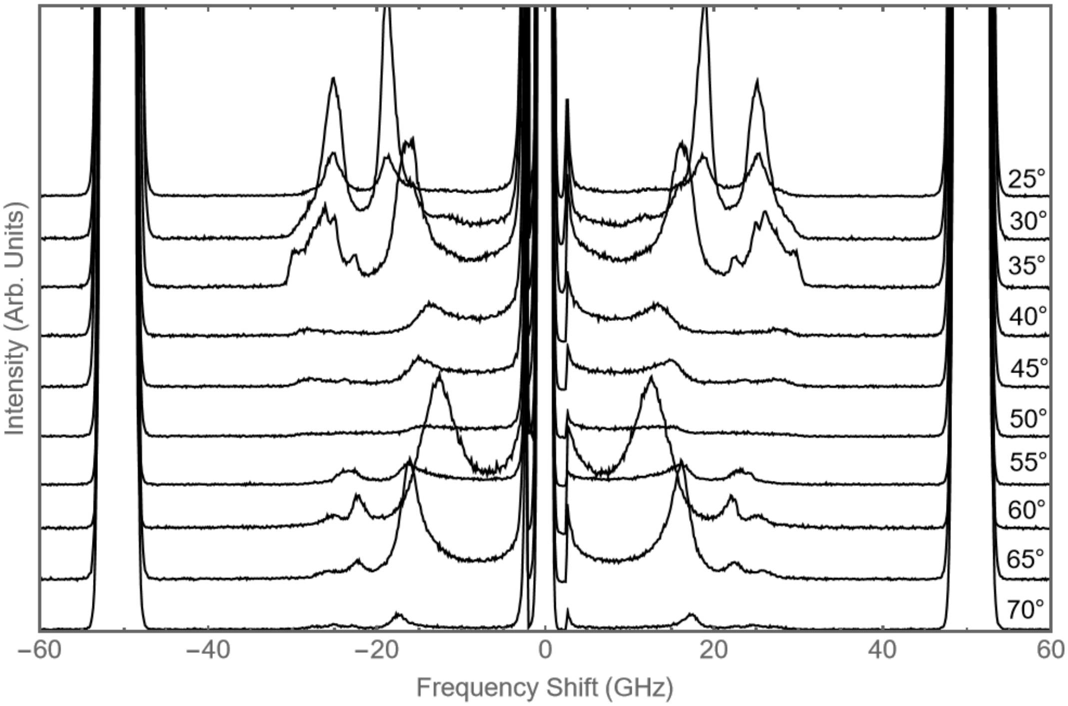

Figure B.3: Brillouin Spectra collected on STMV sample # 3.

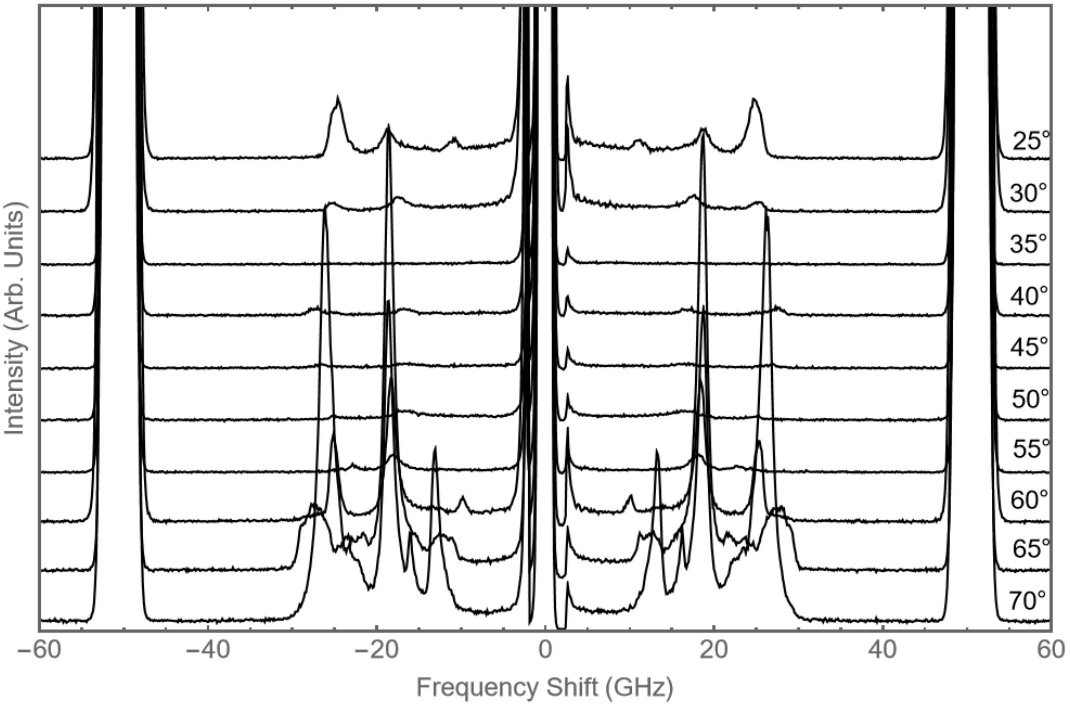

Figure B.4: Brillouin Spectra collected on STMV sample # 4.

Table B.1: Brillouin peak frequency shift (f) and linewidth (Γ) for STMV samples.

	STMV #1		STMV #2		STMV #3		STMV #4	
Incident Angle (°)	f_1 [GHz]	Γ_1 [GHz]	f_2 [GHz]	Γ_2 [GHz]	f_3 [GHz]	Γ_3 [GHz]	f_4 [GHz]	Γ_4 [GHz]
25	-	-	-	-	18.6 ± 0.2	2.2 ± 0.4	18.7 ± 0.3	-
30	-	-	-	-	18.8 ± 0.1	2.1 ± 0.2	-	-
35	-	-	-	-	16.1 ± 0.3	3.6 ± 0.4	17.53 ± 0.2	-
40	-	-	-	-	13.6 ± 0.5	-	16.8 ± 0.5	-
45	17 ± 2	-	-	-	14.8 ± 0.3	-	16 ± 2	-
50	16 ± 2	-	15 ± 2	-	13 ± 1	-	17 ± 1	-
55	-	-	16.7 ± 0.7	-	16.2 ± 0.2	-	17 ± 1	-
60	-	-	16 ± 1	-	12.5 ± 0.2	5.7 ± 0.4	18.3 ± 0.1	1.4 ± 0.2
65	16 ± 1	-	14 ± 2	-	16.1 ± 0.1	2.9 ± 0.2	18.7 ± 0.1	1.3 ± 0.2
70	-	-	16.5 ± 0.4	-	17.4 ± 0.3	2.4 ± 0.4	18.7 ± 0.1	1.6 ± 0.2